CONTRACTOR REPORT

SAND83-7029
Unlimited Release

Dynamic Stall Regulation of the Darrieus Turbine

J. W. Oler, J. H. Strickland
B. J. Im, G. H. Graham
Department of Mechanical Engineering
Texas Tech University
Lubbock, Texas 79409

Prepared by Sandia National Laboratories Albuquerque, New Mexico 87185
and Livermore, California 94550 for the United States Department of Energy
under Contract DE-AC04-76DP00789

Printed August 1983

Issued by Sandia National Laboratories, operated for the United States Department of Energy by Sandia Corporation.

Printed in the United States of America
Available from
National Technical Information Service
U.S. Department of Commerce
5285 Port Royal Road
Springfield, VA 22161

NTIS price codes
Printed copy: A08
Microfiche copy: A01

SAND83–7029
Unlimited Release
Printed August 1983

Dynamic Stall Regulation of the Darrieus Turbine

J. W. Oler, J. H. Strickland
B. J. Im, G. H. Graham
Department of Mechanical Engineering
Texas Tech University
Lubbock, Texas 79409

Under Sandia Contract No. 74–1218

Abstract

A two-dimensional unsteady airfoil analysis is described which utilizes a doublet panel method to model the airfoil surface, an integral boundary layer scheme to model the viscous attached flow, and discrete vortices to model the detached boundary layers which form the airfoil wake region. This model has successfully predicted steady lift and drag coefficients as well as pressure distributions for several airfoils with both attached and detached boundary layers. Unsteady calculations have thus far been limited to attached flow situations. Instantaneous pressure distributions have also been obtained on a single-bladed rotor operating in a tow tank in order to provide experimental data for eventual comparison with analytical predictions.

TABLE OF CONTENTS

1. INTRODUCTION.. 1

1.1 Research Motivation and Objectives.......................... 1
1.2 Relationship of Research to Previous Work.................... 3

2. FORMULATION OF THE DYNAMIC STALL MODEL........................... 7

2.1 Overview of the Complete Model.............................. 7
2.2 The Potential Flow Model.................................... 8
2.2.1 Mathematical Representation............................. 8
2.2.2 Separated Flow Model.................................... 9
2.2.3 Solution Method... 17
2.2.4 Problem in Body Fixed Coordinates....................... 20
2.2.5 Numerical Solution by the Collocation Method............ 26
2.2.6 Evaluation of the Influence Coefficients................ 31
2.2.7 Calculation of Airloads................................. 33
2.3 The Boundary Layer Model.................................... 35
2.3.1 Overview of Unsteady Boundary Layer Codes............... 35
2.3.2 Present Boundary Layer Model............................ 37
2.3.3 Transition and Separation............................... 42
2.3.4 Numerical Solution of Boundary Layer Equations......... 44

3. CALCULATION RESULTS.. 46

3.1 Steady, Attached Flows...................................... 46
3.2 Unsteady, Attached Flows.................................... 51
3.3 Quasi-steady, Separated Flows............................... 56

4. DYNAMIC STALL EXPERIMENT.. 67

4.1 Objectives.. 67
4.2 General Test Setup.. 68
4.3 Pressure Measurements....................................... 69
4.4 Strain Gage Measurements.................................... 73
4.5 Discussion of Results....................................... 78
4.5.1 Blade Forces.. 78
4.5.2 Pressure Data... 87

5. CONCLUSIONS AND RECOMMENDATIONS................................... 97

5.1 Summary of the Analytical Study............................. 97
5.2 Summary of the Experimental Investigation.................... 98

6. REFERENCES... 99

7. APPENDICES...103

A. Fundamentals of Potential Aerodynamics........................104
B. An Integral Solution to LaPlace's Equation.....................116
C. Uniqueness Requirements for the Integral Solution..............122
D. Equivalent Doublet and Vortex Surface Distributions............125
E. Experimental Pressure Data.....................................138

1. INTRODUCTION

1.1 Research Motivation and Objectives

The power produced by a Darrieus turbine at its regulation windspeed is much higher than would be anticipated from an analysis based on steady airfoil data. The additional power output is a direct consequence of an unsteady flow phenomena known as dynamic stall. Above the regulation windspeed, the power output typically drops off abruptly.

Although the windspeed range over which the peak power is attained is relatively small, the turbine drive train and electrical power generation equipment must be sized to safely accept that maximum level of power output. Economic studies by Kadlec (1980) and Klimas (1980) have indicated that a 5 to 10 percent reduction in the cost of energy from a one megawatt Darrieus turbine could be achieved if the peak power output is reduced as shown in Figure 1.1. The actual loss of useable power is minimal due to the relatively infrequent occurrence of winds near the regulation windspeed. However, the reduced maximum power output allows the use of smaller and less expensive drive trains and generators. In addition, the overall efficiency of the wind energy conversion system is increased by the improved matching of the aerodynamic and mechanical components.

To control the peak power output of a Darrieus turbine without adversely affecting its performance at low and medium windspeeds, it is necessary to tailor the dynamic stall characteristics of its blades. It is anticipated that "stall regulation" may be achieved through the design of

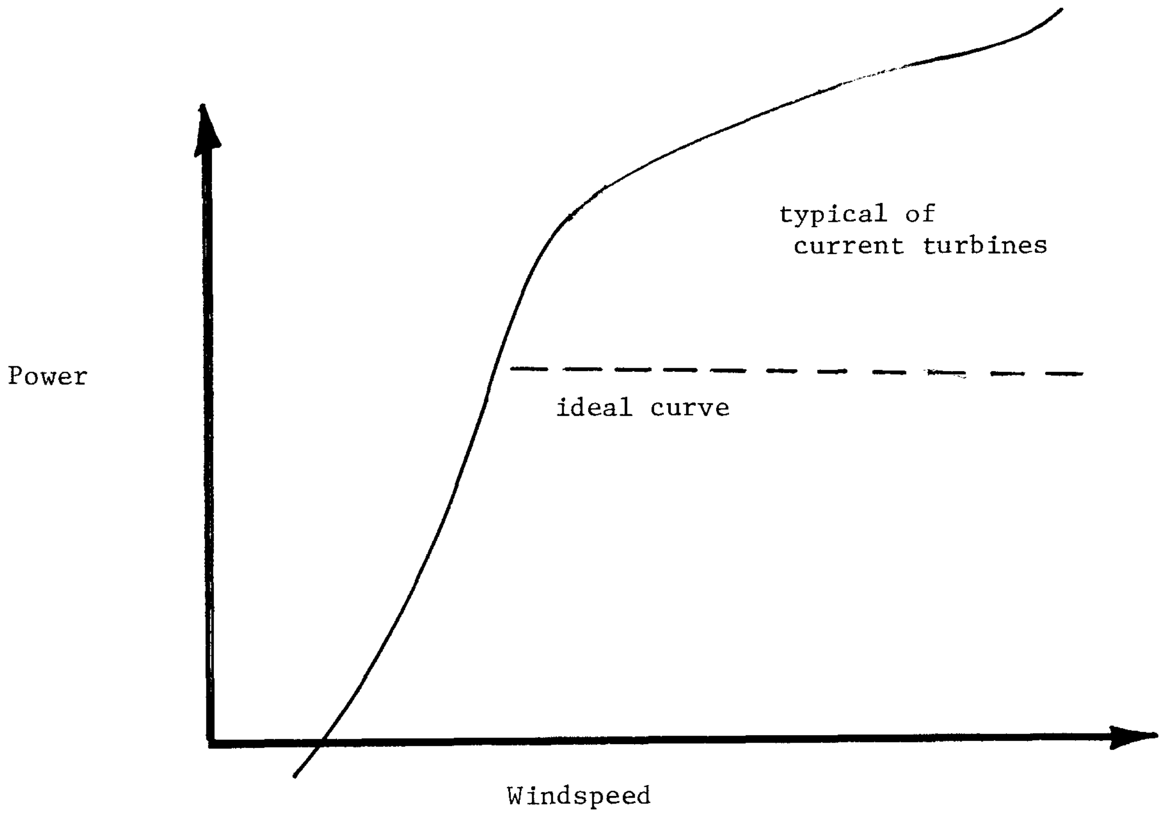

Figure 1.1 Power vs. Windspeed

airfoil sections which either passively exhibit the desired characteristics or have provision for active boundary layer control.

To facilitate the design and evaluation of the new airfoil sections, a valuable tool would be a numerical model capable of predicting the airloads on an airfoil experiencing dynamic stall. The model would allow the examination of many more potential geometries than would be economically feasible if wind tunnel or full-scale turbine tests were required. The research reported herein has been concerned with the development of a numerical model having the capability to perform this function. The current work has been limited to the prediction of the unsteady separated flow over an airfoil at a constant angle of attack. However, as formulated, the model is directly applicable to unsteady airfoil motions as well. Its extension to these cases is currently underway at Texas Tech University.

In addition to the theoretical work reported herein, an experimental program has been conducted. The purpose of this work was twofold. First, it has provided new insights into the mechanisms of dynamic stall and the way in which it influences Darrieus turbine performance. Secondly, it has generated new data which will eventually be utilized to test the predictive capabilities of the numerical model.

1.2 Relationship of Research to Previous Work

Airfoil models used in previous Darrieus turbine aerodynamic simulations can be classified as either thin airfoil potential flow models or lifting line models with tabulated airfoil data. The airfoil model which is currently being formulated includes both viscous and unsteady effects and will be referred to as DYNA2 (DYNamic Airfoil model in 2 dimensions).

The thin airfoil models which have been used by Wilson (1978) and Fanucci (1976) yield good results when the airfoil angles of attack are below stall thresholds and when the airfoil section being modeled is indeed thin. Empirical drag data are required to actually compute the airfoil thrust coefficient. The thin airfoil models do include the important dynamic effects due to pitching and certain added mass effects. They are totally inadequate for predicting static or dynamic stall.

The lifting line model which has been used by Strickland (1976) yields good results when the flow can be considered as quasi steady. Dynamic effects can be estimated using empirical relationships as was recently demonstrated by Klimas (1980) who used the Boeing-Vertol Model by Gormont (1973). The lifting line model used in this fashion required that static lift and drag data for the airfoil in question be available.

The DYNA2 model integrates analytical models for three separate regions of the flow. These three regions require utilization of panel methods to model the potential flow, discrete vortex wake methods to model the separated shear flows, and the boundary layer methods to model the attached shear flows. Each of these analysis methods must include unsteady effects.

A historical review of panel methods by Kraus (1978) reveals that one of the first uses of this type of method was by A.M.O. Smith (1962) for a body with zero lift. These methods have progressed to a point such that three-dimensional lifting geometries can be considered in both subsonic and supersonic flows as typified by the work of Woodward (1973). Many of the investigations using panel methods have been for steady flows, although the general method is well suited to unsteady flows as is evidenced by the works of Ashley (1966), Djojodihardjo and Widnall (1969), Summa (1976), and Oler

(1976). Utilization of panel methods has been concentrated on attached non-separating flows where the wake vorticity is shed smoothly from the trailing edge and the Kutta condition is satisfied. One recent exception is the utilization by NASA Langley of panel methods to examine the flow around a delta wing with leading edge separation.

The modeling of separated wakes using discrete vortices can be viewed as being a natural extension of unsteady panel methods. For instance, in the case of a stalling airfoil, the wake will consist of two wake surfaces instead of the usual one for unseparated flow. Clements (1975) gives a comprehensive review of wake modeling using discrete vortices. Many of the investigations reported by Clements pertain to flow behind bluff bodies such as that due to Sarpkaya (1979) for flow behind circular cylinders. These bluff bodies were in all cases immersed in a fluid with steady, uniform freestream velocities. Most of the workers used potential flow models based on conformal mapping techniques as opposed to utilization of the more flexible panel methods. One example of wake modeling using discrete vortices is that due to Ham (1968) in which he modeled dynamic stall by allowing a single vortex to be shed from the leading edge of the airfoil at some assumed angle of attack.

A number of unsteady turbulent boundary layer analyses are available in the literature ranging from integral forms (e.g., Daneshyar, 1978) to one-equation closure models (e.g., Nash, et al., 1975), to multiple equation closure models. Due to the large number of boundary layer calculations required for unsteady cases, the simpler models should be used when possible. Part of the work leading to the development of DYNA2 has been to extend the relatively successful integral method due to Head (1969) to include unsteady effects.

The major contribution of the DYNA2 model and its possible extensions is that it provides a synthesis of existing techniques to provide a reasonably general unsteady airfoil model which includes the prediction of dynamic stall. In reading the literature, it is apparent that much of the work has been compartmentalized into potential flow via panel methods, separated wakes via discrete vortices, and turbulent boundary layers via a number of closure models. Due to the relatively mature nature of the work in each of these areas, it therefore seems appropriate and timely to combine these techniques into a more complete model.

2. FORMULATION OF THE DYNAMIC STALL MODEL

2.1 Overview of the Complete Model

There are two principal components contained in DYNA2. These are the potential flow and boundary layer calculation routines. Both routines include unsteady effects and are coupled through the pressure distribution and boundary layer separation effects.

The potential flow calculations are accomplished with a finite element method which allows representation of the airfoil and wake surfaces by uniform strength doublet panels. The wake includes a surface extending from the boundary layer separation point as well as from the trailing edge. The routine predicts the position and strength of the wake surfaces and the corresponding pressure distribution and integrated load on the airfoil.

In the model's present form, the location of the boundary layer separation point is predicted on the basis of a pressure distribution for a steady, nonseparated flow. That location is considered fixed as the potential flow calculations proceed in a step-by-step manner. Obviously, a more correct arrangement would be to recalculate the separation point location at each time step. However, the difficulties (discussed in the next chapter) which have been encountered when that method was utilized have forced the temporary adoption of the present scheme. The resolution of the step-by-step boundary layer calculation problems is the subject of work currently underway at Texas Tech University.

2.2 The Potential Flow Model

2.2.1 Mathematical Representation

Consider the motion of a homogeneous, incompressible and inviscid fluid through which a body with its associated trailing wake moves. The body surface is given with respect to a fluid fixed reference frame by

$$S(\vec{r},t) = 0 \qquad (2.2.1)$$

and the trailing wake by

$$W(\vec{r},t) = 0 \qquad (2.2.2)$$

The possibility of a separated flow is accounted for by allowing the wake to include surfaces of potential discontinuity emanating from a boundary layer separation point as well as from the trailing edge.

Noting that the body plus wake comprises a complete lifting system and assuming that the motion was started from a state of rest or uniform motion, it follows that the motion is irrotational for all times. The governing equation for the disturbance potential is given by

$$\nabla^2\phi(\vec{r},t) = 0 \ . \qquad (2.2.3)$$

Once the solution is known, the pressure distribution in the flow may be found from the unsteady Bernoulli equation:

$$P = P_\infty - \rho\left(\frac{\partial\phi}{\partial t} + \frac{1}{2}\nabla\phi^2\right) \ . \qquad (2.2.4)$$

The determination of a unique solution of Eqn. 2.2.3 is accomplished through the application of the following boundary conditions:

1) The Infinity Condition -

The disturbance potential resulting from the presence of the body must vanish at infinity.

2) The Kinematic Surface Tangency Condition -

On the surface, S, the normal relative fluid velocity must be zero.

3) The Kutta Condition -

At all times, the flow of fluid from the trailing edge must be smooth and continuous.

4) The Boundary Layer Separation Condition -

The sheet of potential discontinuity from the boundary layer separation point must reflect the injection of the boundary layer vorticity.

5) The Dynamic Free Surface Condition -

The pressure must be continuous through the wake surfaces, since they cannot sustain a load.

6) The Geometric Free Surface Condition -

The wake particles are convected downstream at the local convection velocities.

2.2.2 Separated Flow Model

For the purpose of modeling, it is assumed that the wake may be adequately represented by two sheets of potential discontinuity. One surface extends from the trailing edge while the other originates at the boundary layer separation point as illustrated in Fig. 2.2.1.

The rates at which vorticity is shed into the two wake surfaces are related to the rate of change of the vorticity bound to the airfoil surface by the Kelvin-Helmholtz vorticity conservation theorem.

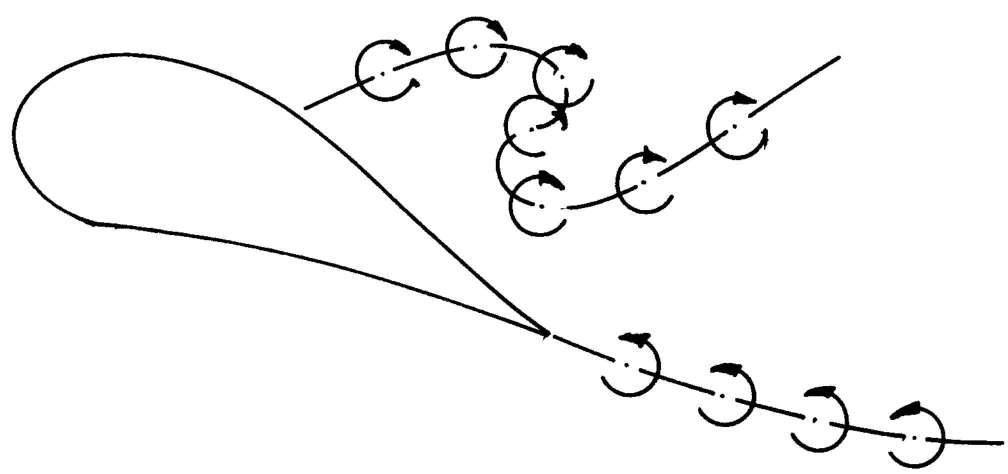

Figure 2.2.1 Separated Flow Model

The theorem requires that the rate of change of net vorticity in the flow field is zero, i.e.,

$$\frac{d\Gamma_{net}}{dt} = 0$$

or (2.2.5)

$$\frac{d\Gamma_b}{dt} + \frac{d\Gamma_w}{dt} + \frac{d\Gamma_s}{dt} = 0 \ .$$

Here, the net vorticity has been divided into three components: the vorticity bound to the airfoil surface Γ_b, the vorticity shed from the boundary layer separation point Γ_s, and the vorticity shed from the trailing edge Γ_w. The time derivatives of Γ_w and Γ_s represent the rate of vorticity shedding to the respective wake surfaces.

A simple vorticity flux analysis may be utilized to estimate the vorticity shedding rate from the boundary layer separation point.

$$\frac{d\Gamma_s}{dt} = \int_o^\delta u\left(\frac{\partial u}{\partial y} - \frac{\partial v}{\partial x}\right) dy$$

$$\frac{d\Gamma_s}{dt} \cong \int_o^\delta \frac{1}{2}\frac{\partial u^2}{\partial y} dy \qquad (2.2.6)$$

$$\frac{d\Gamma_s}{dt} \cong \frac{U_e^2}{2}$$

where U_e is the edge velocity. An assumption has been made here that 100% of the vorticity contained in the boundary layer is injected into the inviscid flow field at the separation point. This is actually an overestimate so that a reduction factor is needed in the actual calculations.

In Appendix D, it is demonstrated that the vortex sheet strength distribution is equal to the gradient of the potential jump across that sheet. If γ_b is the vorticity per unit length along an airfoil surface and σ is the distribution of potential discontinuity or doublet strength along the surface, then referring to Fig. 2.2.2, the bound vorticity may be written as

$$\Gamma_b = \int_A^B \gamma_b ds$$

$$\Gamma_b = \int_A^B \frac{d\sigma}{ds} ds \qquad (2.2.7)$$

$$\Gamma_b = \Delta\sigma_{TE} \ .$$

The rate of change of bound vorticity may be expressed in terms of the difference in surface doublet strength at the trailing edge:

$$\frac{d\Gamma_b}{dt} = \frac{d}{dt}(\Delta\sigma_{TE}) \ . \qquad (2.2.8)$$

Substituting Eqns. 2.2.6 and 2.2.8 into Eqn. 2.2.5 provides an expression for the rate of shedding of vorticity to the wake surface extending from the trailing edge.

$$\frac{d\Gamma_w}{dt} = -(\frac{d}{dt}(\Delta\sigma_{TE}) + \frac{U_e^2}{2}) \ . \qquad (2.2.9)$$

Recall that Eqn. 2.2.9 was based upon the Kelvin-Helmholtz vorticity conservation theorem. The same result may be arrived at by applying the dynamic free surface boundary condition at the airfoil trailing edge. Specifically, the pressure must be continuous across the wake over its entire length, including the point of attachment at the trailing edge. There, the pressure difference across the infinitely thin surface is zero which leads to

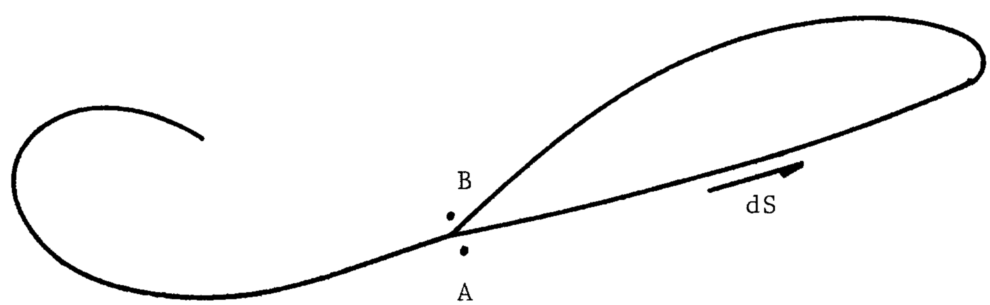

Figure 2.2.2 The Bound Vorticity on an Airfoil

$$0 = P_u - P_\ell$$
$$0 = \frac{\partial}{\partial t}(\phi_u - \phi_\ell) + \frac{1}{2}(\nabla\phi_u^2 - \nabla\phi_\ell^2) \quad . \tag{2.2.10}$$

Recognizing that $\nabla\phi = \vec{u}$ for the fluid fixed reference frame, then

$$\frac{1}{2}(U_u^2 - U_\ell^2) = -\frac{\partial}{\partial t}(\Delta\phi_{TE}) \quad . \tag{2.2.11}$$

From Fig. 2.2.3, it is noted that $(U_u^2 - U_\ell^2)/2$ is the net rate of vorticity shedding from the boundary layers on the upper and lower surfaces of the airfoil at the railing edge. Then,

$$\frac{d\Gamma_w}{dt} = -\frac{d}{dt}(\Delta\phi_{TE}) \quad . \tag{2.2.12}$$

By calculating the circulation about a curve, as shown in Fig. 2.2.4, which encloses the airfoil and wake surface extending from the boundary layer separation point, it is apparent that

$$\frac{d}{dt}(\Delta\phi_{TE}) = \frac{d\Gamma_b}{dt} + \frac{d\Gamma_s}{dt} \quad . \tag{2.2.13}$$

So,

$$\frac{d\Gamma_w}{dt} = -\left(\frac{d\Gamma_b}{dt} + \frac{d\Gamma_s}{dt}\right) \tag{2.2.14}$$

which is equivalent to the result obtained from the Kelvin-Helmholtz theorem.

An important consequence of boundary layer separation may be noted by applying the dynamic free surface condition to the wake surface extending from the separation point. Let points A and B be located an infinitesimal distance ahead of and behind the boundary layer separation point. The pressure difference across the two points must be zero which results in

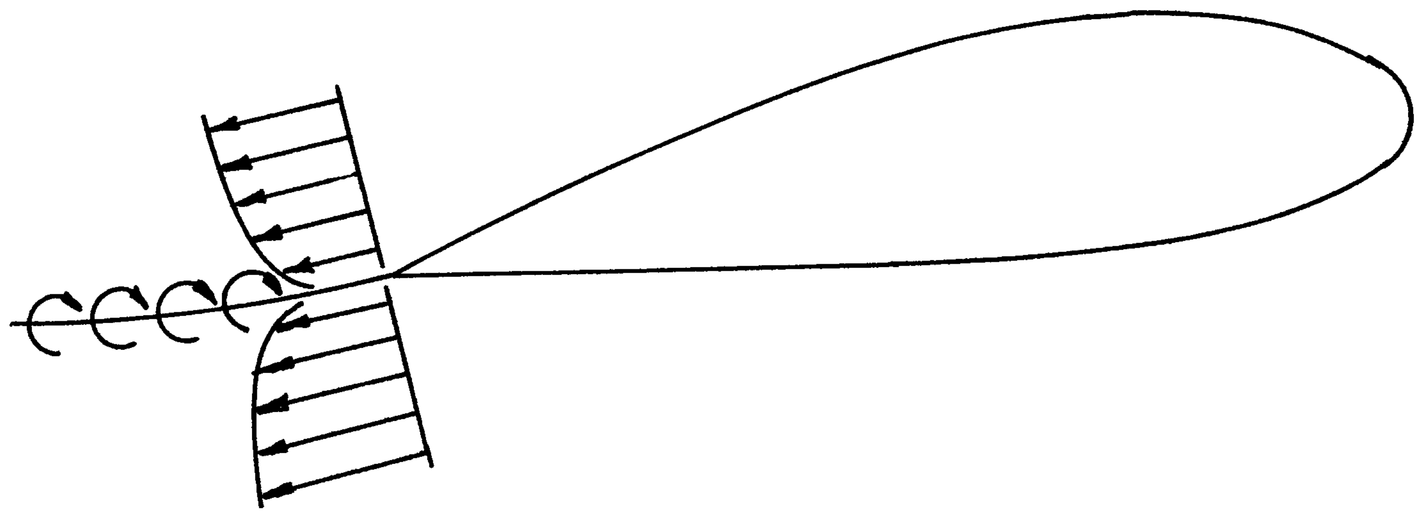

Figure 2.2.3 The Net Rate of Vorticity Shedding at the Trailing Edge

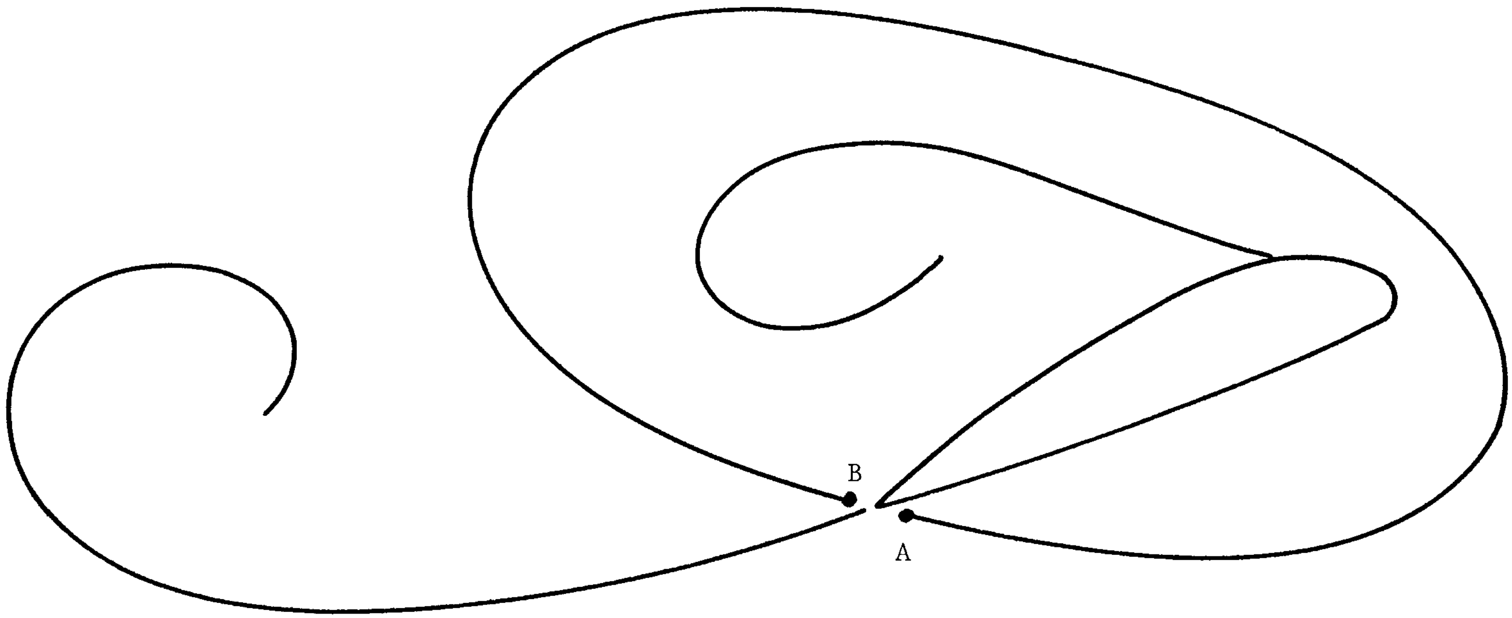

Figure 2.2.4 The Rate of Change of Potential Jump Across the Trailing Edge

$$0 = \frac{\partial}{\partial t}(\phi_A - \phi_B) + \frac{1}{2}(\nabla\phi_A^2 - \nabla\phi_B^2) \ . \tag{2.2.15}$$

As in Eqn. 2.2.11, we may write

$$\frac{\partial\Gamma_s}{\partial t} = \frac{1}{2}(\nabla\phi_A^2 - \nabla\phi_B^2) \ . \tag{2.2.16}$$

Substituting into Eqn. 2.2.15 yields

$$\frac{\partial\phi_B}{\partial t} = \frac{\partial\phi_A}{\partial t} + \frac{d\Gamma_s}{dt} \ . \tag{2.2.17}$$

Therefore, it is noted that behind the boundary layer separation point, there is an additional increment to $\partial\phi/\partial t$ equal to the rate of vorticity shedding from the separation point.

The same observation may be made by considering the rate of change of the potential jump across the trailing edge as described by Eqn. 2.2.13 which may be rewritten as

$$\frac{d\phi_u}{dt} = \frac{d\phi_\ell}{dt} + \frac{d\Gamma_b}{dt} + \frac{d\Gamma_s}{dt} \ . \tag{2.2.18}$$

For the case of a steady stalled airfoil, the average rates of change of Γ_b and ϕ_ℓ are zero, yet the $d\phi_u/dt$ is nonzero due to the vorticity being shed from the boundary layer separation point.

The additional contribution to $\partial\phi/\partial t$ in the separated region is important in the calculation of the pressure distribution around the airfoil. Without its inclusion, a finite pressure jump will be indicated across the two wake surfaces and erroneous values of lift and drag will result.

2.2.3 Solution Method

For the potential flow model described in the previous sections, the governing equation is the linear Laplace equation,

$$\nabla^2\phi(\vec{r},t) = 0$$

Through an application of Green's theorem (see Appendices C and D), it may be shown that any solution to Eqn. 2.2.18 may be represented by integrals of sources and doublets distributed over the boundaries of the flow. Furthermore, a unique solution may be obtained utilizing surface distributions of doublets alone. The Green's function solution to Eqn. 2.2.18 is then given by

$$\phi(\vec{r},t) = \frac{1}{2\pi} \iint_S \sigma \frac{\partial}{\partial \upsilon}\left[\frac{1}{R}\right] dS + \frac{1}{2\pi} \iint_W \Delta\phi^W \frac{\partial}{\partial \upsilon}\left[\frac{1}{R}\right] dS \tag{2.2.19}$$

where $\sigma = \sigma(\xi,t)$, doublet strength distribution on $S(\vec{\xi},t) = 0$.

$\Delta\phi^W = \Delta\phi^W(\vec{\xi},t)$, doublet strength distribution on $W(\vec{\xi},t) = 0$.

$\vec{\upsilon}$ = surface normal on $S(\vec{\xi},t) = 0$ or $W(\vec{\xi},t) = 0$.

$R = \left| \vec{r}-\vec{\xi} \right|$, vector distance between the "field" point, $\vec{r}$, and "source" point, $\vec{\xi}$.

The body and wake doublet strength distributions, σ and $\Delta\phi^W$, respectively, must be determined through application of the boundary conditions. It should be noted that the infinity condition is inherently satisfied by Eqn. 2.2.19.

The surface tangency condition requires that the normal relative velocity component between the fluid and solid surfaces vanish on the surfaces. This condition may be expressed as

$$\frac{\partial n}{\partial t} + \frac{\partial \phi}{\partial n} + \vec{U}_\infty \cdot \vec{n} = 0$$

$$\text{on } S(\vec{r},t) \tag{2.2.20}$$

Substitution of Eqn. 2.2.19 into Eqn. 2.2.20 yields

$$\frac{1}{2\pi} \iint_S \sigma \frac{\partial^2}{\partial n\, \partial \upsilon}[\frac{1}{R}]dS = -\{\frac{\partial n}{\partial t} + \vec{U}_\infty \cdot \vec{n}$$

$$+ \frac{1}{2\pi} \iint_W \Delta\phi^W \frac{\partial^2}{\partial n\, \partial \upsilon}[\frac{1}{R}]dS\} \tag{2.2.21}$$

$$\text{on } S(\vec{r},t) = 0$$

Eqns. 2.2.21 provides a singular Friedholm integral equation of the first kind for the unknown surface doublet strength distributions. Once it has been solved subject to the remaining boundary conditions, the potential at any point in the flow field may be determined by Eqn. 2.2.19. The solution is complicated, however, by the dependency upon the wake surface locations which are also unknown.

Consider the following approach to the solution of Eqns. 2.2.21:

1) At $t = 0$, let the body be started impulsively and the freestream velocity brought instantaneously to $\vec{U}_\infty$. For this instant, there is no wake and no contribution to the downwash on the body by the wake. A unique solution for the potential field may then be found through a simultaneous application of the surface tangency condition (Eqn. 2.2.21) and the Kutta condition.

2) Over the next infinitesimal time increment, assume that the resulting potential (and velocity) field are unchanged. As a result, the wake surfaces generated during that time increment

may be predicted through the application of the Kutta and boundary layer separation conditions.

3) For the next time step, the integrals over the wake surfaces of Eqns. 2.2.21 are known and the equation may once again be solved with the Kutta condition for σ.

4) Again assuming the velocity field to remain constant over the time increment, the new locations of the existing wake surfaces may be calculated through application of the dynamic and geometric free surface conditions. In addition, new wake surfaces are shed as before.

5) In this way, the solution proceeds in a step-by-step manner towards the steady state or periodic final result.

2.2.4. Problem in Body Fixed Coordinates

In the previous sections, a mathematical representation of the general motion of a finite number of rigid bodies through an ideal fluid was described. All expressions were made with respect to an inertial, fluid fixed reference frame, i.e., translating at $\vec{U}_\infty$.

We now assume that the body is rigid. As a result, the functional representations of the body surface is independent of time when given with respect to a body fixed coordinate system. This plus the fact that the governing Laplace equation is not explicitly time dependent suggest that it would be advantageous to transform the problem to a body fixed coordinate system.

Consider the motion of a body through an ideal fluid as shown in Fig. 2.2.5. We denote by K_O or the subscript 'o', operations with respect to the fluid fixed frame. A K or the absence of a subscript

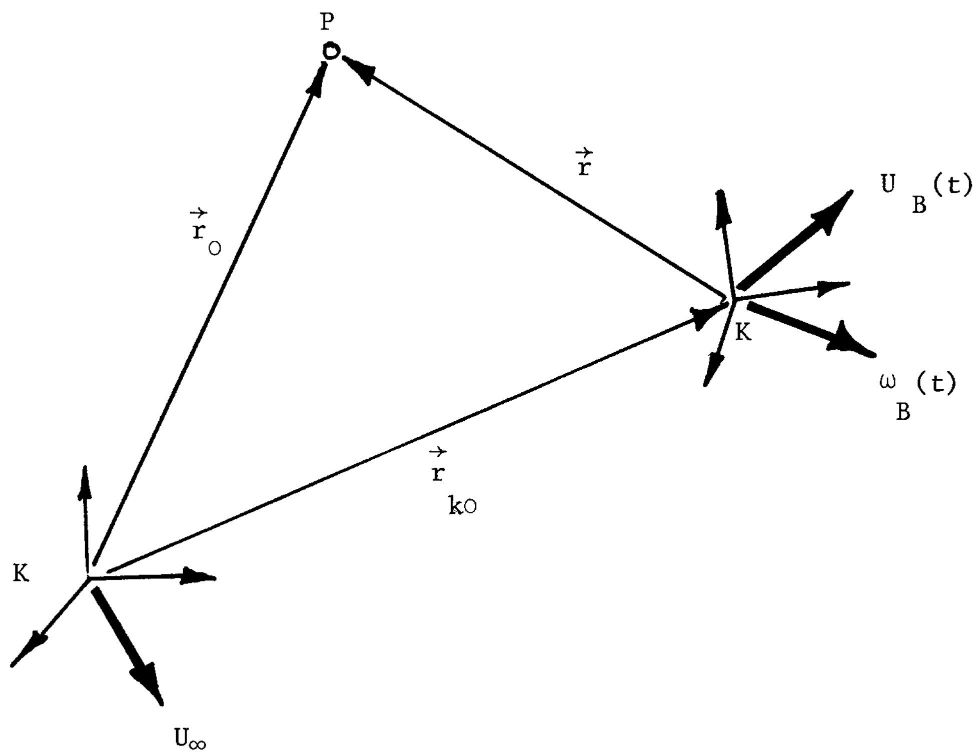

Figure 2.2.5 Inertial and Body Fixed Reference Frames

indicates operations with respect to the body fixed frame. These coordinate systems are illustrated in Fig. 2.2.5. It should be noted that the translational velocity, U_∞, of the K_o frame and the translational and rotational velocities, U_B and ω_B, of the K frame are taken with respect to an inertially fixed frame.

To establish the connection between the two coordinate systems, note that the position vectors for an arbitrary fluid fixed point P for the two reference frames are related by

$$\begin{aligned} \vec{r} &= \vec{r}(\vec{r}_o,t) \\ &= [T]\{\vec{r}_o - \vec{r}_{Ko}(t)\} \end{aligned} \tag{2.2.22}$$

where $\vec{r}_{Ko} = \int_o^t \vec{U}_{Ko}(\tau)d\tau + \vec{r}_{Ko}(0)$

and $[T]$ = coordinate transformation matrix, i.e., for any vector $\vec{A}_o$, $\{A\} = [T]\{A_o\}$.

Consider the disturbance potential field, ϕ. Since the value of a scalar field is independent of the reference frame, we may write

$$\phi_o(\vec{r}_o,t) = \phi(\vec{r},t) \tag{2.2.23}$$

Similarly, for the pressure field and body surface function, it follows that

$$P_o(\vec{r}_o,t) = P(\vec{r},t) \tag{2.2.24}$$

$$S_o(\vec{r}_o,t) = S(\vec{r}). \tag{2.2.25}$$

In Eqn. 2.2.25, advantage has been taken of the fact that S is independent of time with respect to the body fixed reference frame.

Since the gradient operator defines a vector field, gradients from the K_o and K frames may be related by

$$\{\nabla\} = [T]\{\nabla_o\} \tag{2.2.26}$$

Then for the Laplacian,

$$\nabla^2 = \{\nabla\}^T \{\nabla\}$$

or (2.2.27)

$$\nabla^2 = \{\nabla_o\}^T [T]^T [T] \{\nabla_o\}$$

For the particular case of a transformation matrix, it may be shown that

$$[T]^{-1} = [T]^T$$

so

$$[T]^T [T] = [I].$$

Eqn. 2.2.27 then becomes

$$\nabla^2 = \{\nabla_o\}^T \{\nabla_o\}$$

or (2.2.28)

$$\nabla^2 = \nabla_o^2.$$

To relate the time derivatives for the two reference frames, we write

$$\frac{\partial}{\partial t_o} = \frac{\partial t}{\partial t_o}\frac{\partial}{\partial t} + \frac{\partial \vec{r}}{\partial t} \cdot \nabla$$

But since time is unchanged by the transformation,

$$\frac{\partial t}{\partial t_o} = 1$$

and (2.2.29)

$$\frac{\partial}{\partial t} = \frac{\partial}{\partial t} + \frac{\partial \vec{r}}{\partial t} \cdot \nabla$$

The second term of the right hand side of Eqn. 2.2.29 is the contribution to the temporal variation due to the motion of the K frame relative to the K_o or fluid fixed frame. In a sense, it is like the convective contribution to a substantial derivative due to the fact that it represents the change of a property Q(r) resulting from a variation of r with respect to the fluid fixed reference frame.

Eqn. 2.2.29 may be rewritten as

$$\frac{\partial}{\partial t_o} = \frac{\partial}{\partial t} + [\vec{U}_\infty - \vec{U}_B(t) - \vec{\omega}_B \times \vec{r}] \cdot \nabla \tag{2.2.30}$$

where the relative velocity between the K and K_o frames has been written as the difference of their velocity with respect to the inertially fixed frame.

Recall from the previous section that the governing equation for the potential flow model is

$$\nabla_o^2 \phi_o(\vec{r}_o, t) = 0 \tag{2.2.31}$$

where the subscripts 'o' indicate operations with respect to the fluid fixed frame. Substitution of Eqns. 2.2.23 and 2.2.28 into Eqn. 2.2.31 yields

$$\nabla^2 \phi(\vec{r}, t) = 0 \tag{2.2.32}$$

which is the governing equation for the body fixed problem.

The surface tangency boundary condition was written for the fluid fixed frame as

$$\frac{1}{|\nabla_o S_o(\vec{r}_o,t)|}\frac{\partial S_o(\vec{r}_o,t)}{\partial t} + \nabla_o\phi_o(\vec{r}_o,t)\cdot\frac{\nabla_o S_o(\vec{r}_o,t)}{|\nabla_o S_o(\vec{r}_o,t)|} = 0 \tag{2.2.33}$$

on $S_o(\vec{r}_o,t) = 0.$

Substitution of Eqns. 2.2.23, 2.2.25, and 2.2.30 into Eqn. 2.2.33 yields

$$\frac{1}{|\nabla S(\vec{r})|}\{\frac{\partial S(\vec{r})}{\partial t} + [\vec{U}_\infty - \vec{U}_B(t) - \vec{\omega}_B(t) x \vec{r}]\cdot\nabla S(\vec{r})\}$$

$$+ \nabla\phi \cdot \frac{\nabla S(\vec{r})}{|\nabla S(\vec{r})|} = 0$$

or

$$\frac{\partial\phi(\vec{r},t)}{\partial n(\vec{r})} = - [\vec{U}_\infty - \vec{U}_B(t) - \vec{\omega}_B(t) x \vec{r} - \frac{\partial\vec{n}(\vec{r})}{\partial t}] \text{ on } S(\vec{r}) = 0 \tag{2.2.34}$$

where $n(\vec{r})$ = outward normal on $S(\vec{r}) = 0$ with respect to the body fixed frame.

An expression for the pressure field in fluid fixed coordinates was given previously by

$$P(\vec{r}_o,t) = P_\infty - \rho\{\frac{\partial\phi_o(\vec{r}_o,t)}{\partial t} + \frac{1}{2}[\nabla_o\phi_o(\vec{r}_o,t)]^2\}.$$

This may be rewritten in body fixed coordinates as

$$P(\vec{r},t) = P_\infty - \rho\{\frac{\partial\phi(\vec{r},t)}{\partial t} + [\vec{U}_\infty - \vec{U}_B - \vec{\omega}_B(t) \text{ x } \vec{r}] \cdot \nabla\phi(\vec{r},t)$$

$$+ \frac{1}{2}[\nabla\phi(\vec{r},t)]^2\} \ . \tag{2.2.35}$$

2.2.5 Numerical Solution by the Collocation Method

We now wish to develop a technique for solving Eqn. 2.2.34 with the aid of a digital computer. For this purpose, the blade and wake surfaces are descritized into M_B and $M_w(t)$ elements as shown in Fig. 2.2.7. Over each surface element, the unknown doublet strength distribution is approximated with a uniform distribution of unknown magnitude. The centroids of the surface elements are identified as control points at which the surface tangency condition is satisfied exactly.

In addition to the surface tangency condition, a Kutta condition must be applied at the trailing edge to uniquely specify the unknown potential distribution (see Appendix A). The essential requirement of all forms of the Kutta condition is that the flow proceed smoothly from the trailing edge of the airfoil. Actual enforcement of the condition may be accomplished by specifying the direction of wake shedding, matching the upper and lower surface trailing edge pressures or by matching velocities if a steady flow. Whatever the method of application, the Kutta condition provides an additional boundary condition which serves to represent the essential consequence of viscous boundary layers in a real fluid flow.

Consider the case of an isolated body descritized into M elements as shown in Fig. 2.2.7. We now have M surface tangency conditions plus the Kutta condition but only M unknown doublet panel strengths, σ_i so that the problem as stated is overspecified. Either an additional singularity of unknown strength must be added to the flow or the number of boundary conditions must be reduced. The latter approach has been followed in the present investigation.

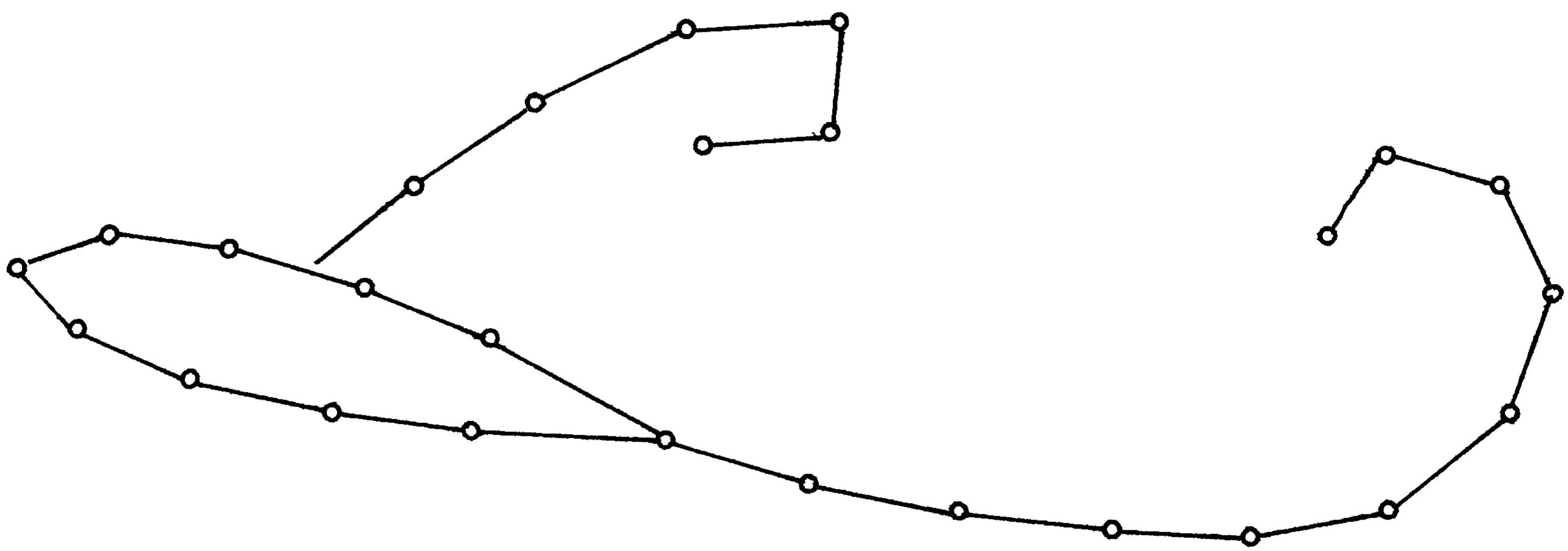

Figure 2.2.7 Finite Element Representation of Airfoil and Wake Surfaces

Rather than applying surface tangency conditions on both the upper and lower surface elements at the trailing edge, the flow is required to be tangent to the trailing edge bisector as shown in Fig. 2.2.8. In this way, the Kutta condition is satisfied as well as approximate forms of the surface tangency conditions on the trailing edge elements. Therefore, the three boundary conditions at the trailing edge are replaced by a single one and the number of boundary conditions is M-1. A final condition on the unknown doublet strengths is found by assuming that the potential jump across the trailing edge has equal contributions from the upper and lower elements, i.e., $\Delta\phi_{TE} = \sigma_M - \sigma_1$ and $\sigma_M = -\sigma_1 = \Delta\phi_{TE}/2$.

With these approximations, the surface tangency condition of Eqn. 2.2.21 may be rewritten in matrix format as

$$[A]\{\sigma\} = \{D\} - [A^W]\{\Delta\phi^W\} \tag{2.2.36}$$

where $A_{i,j}$ = normal induced velocity coefficient at the i^{th} control point due to the j^{th} source element

$$= \frac{1}{2\pi} \iint_{\delta S_j} \frac{\partial^2}{\partial n_i \, \partial \upsilon_j} [\frac{1}{R}] dS$$

$$R = | \vec{r}_i - \vec{\xi}_j |$$

$\vec{r}_i$ = position of the i^{th} control point

$\vec{\xi}_j$ = position of the j^{th} source element

$\vec{n}_i$ = surface normal at the i^{th} control point

$\vec{\upsilon}_j$ = surface normal at the j^{th} source element

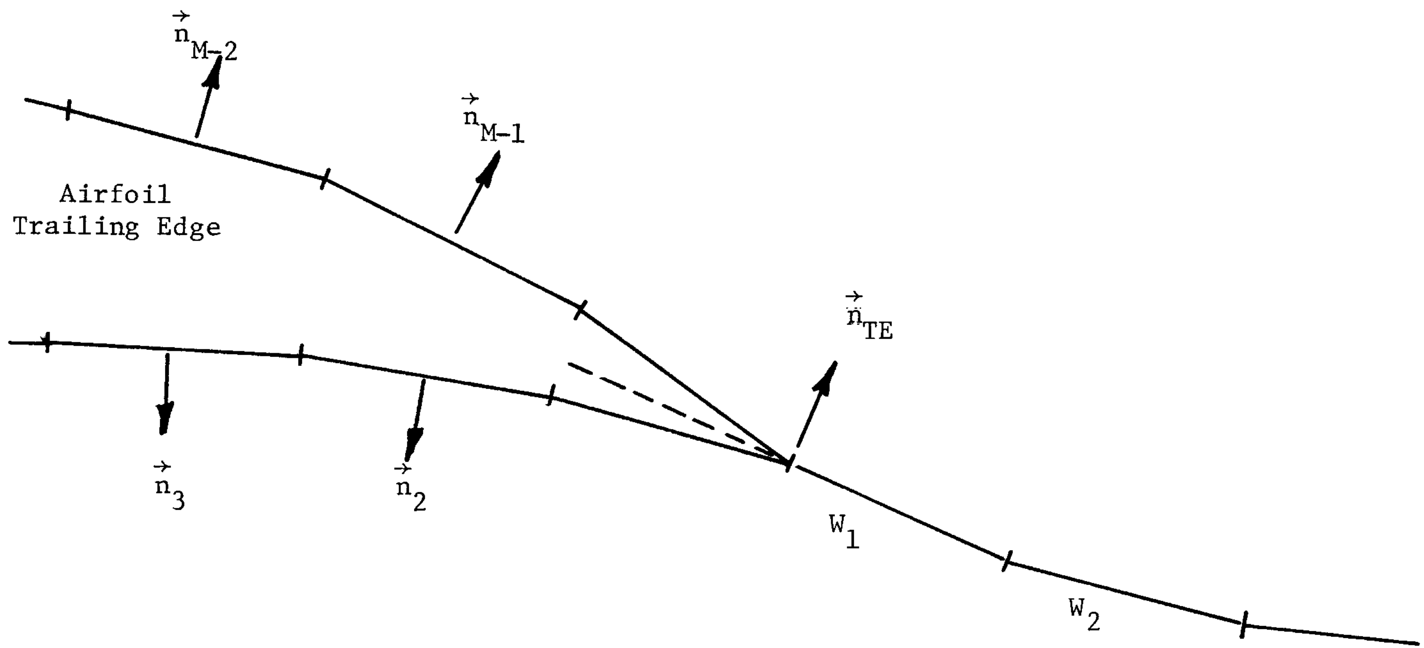

Figure 2.2.8 The Kutta Condition at the Trailing Edge

and

σ_j = strength of the j^{th} doublet element

D_i = normal downwash at the i^{th} control point due the freestream velocity and motion of S

$A^w_{i,j}$ = normal induced velocity coefficient at the i^{th} control point due to the j^{th} wake source element

$\Delta\phi^w_j$ = strength of the j^{th} wake doublet element.

Recall that the body and freestream are started impulsively such that the wake doublet strengths, $\{\Delta\Phi^w\}$, are known for that instant and all later ones. Therefore, it is convenient to define

$$\{B\} = \text{total downwash array}$$

$$= \{D\} - [A^w]\{\Delta\phi^w\}$$

so that Eqn. 2.2.36 becomes

$$[A]\{\sigma\} = \{B\} \qquad (2.2.37)$$

We may then solve the linear equation set for the body surface doublet distribution, $\{\sigma\}$, i.e.,

$$\{\sigma\} = [A]^{-1}\{B\}. \qquad (2.2.38)$$

It should be noted that the coefficient matrix, [A], does not change with time since the body has a fixed geometry.

Once the unknown doublet strengths have been determined, the potential for any b points in the field may be found from a matrix expression of Eqn. 2.2.19,

$$\{\phi_b\} = [C_b]\{\sigma\} + [C^w_b]\{\Delta\phi^w\}. \qquad (2.2.39)$$

2.2.6 Evaluation of the Influence Coefficients

As noted in the previous section, the representation of a general doublet distribution on a surface element by a uniform distribution permits the definition of normal velocity and potential influence coefficients. These were given by

$$A_{i,j} = \frac{1}{2\pi} \iint \delta S_j \frac{\partial^2}{\partial n_i \, \partial \nu_j} [\frac{1}{R}] dS \tag{2.2.40}$$

and C_j $\equiv$ potential influence coefficient at $\vec{r}_b$ due to the j^{th} source element

$$C_j = \frac{1}{2\pi} \iint \delta S_j \frac{\partial}{\partial \nu_j} [\frac{1}{R}] dS \tag{2.2.41}$$

The direct evaluation of the integrals of Eqns. 2.2.40 and 2.2.41 may be avoided if we take advantage of the analogy between surface distribution of doublets and vortices. It may be shown (see Appendix D) that a general distribution of doublets may be represented by a distribution of vortices on the surface. The strength of the vortex sheet at any point is equal to the gradient of the doublet strength with vortices normal to that gradient. For the particular case of a surface element having a uniform doublet distribution, an equivalent representation is that of a vortex ring on the boundary of the element with strength equal to the element doublet strength. This is illustrated for a two-dimensional surface element in Fig. 2.2.9.

We may determine the influence coefficients by evaluating the vortex equivalents of the doublet elements. Referring to Fig. 2.2.9, the potential influence coefficient may be written as

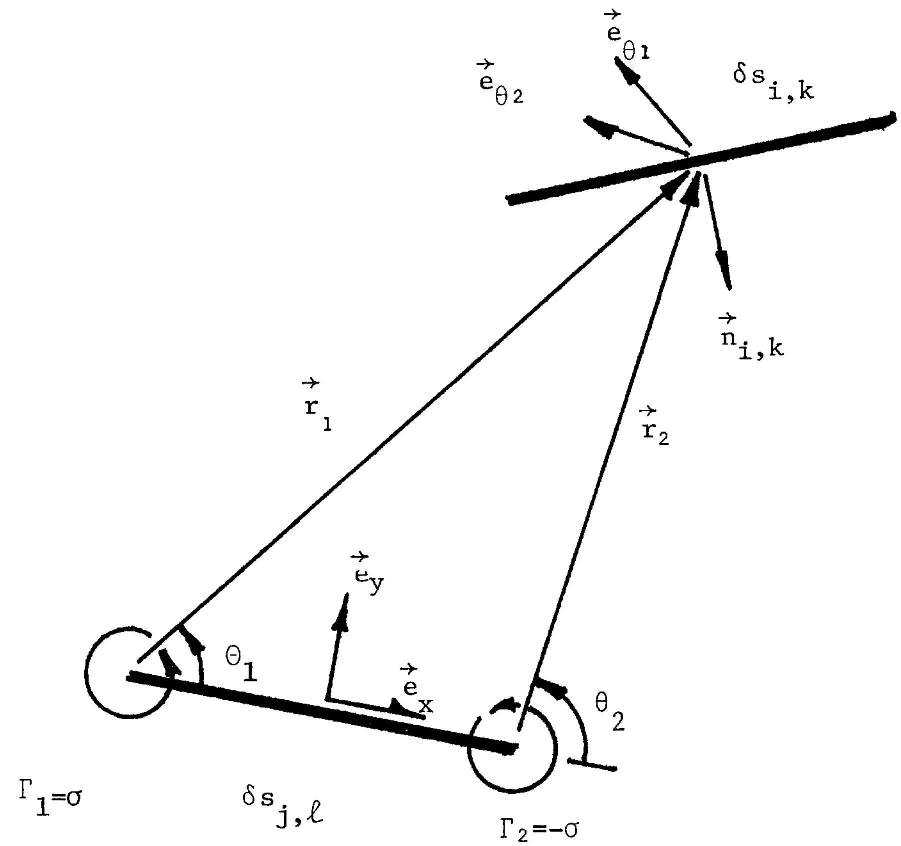

Figure 2.2.9 Evaluation of Element Influence Coefficients

$$C_j = \frac{\theta_1}{2\pi} - \frac{\theta_2}{2\pi}$$

$$= \frac{1}{2\pi}\left[\tan^{-1}\left(\frac{\vec{r}_1 \cdot \vec{e}_y}{\vec{r}_1 \cdot \vec{e}_x}\right) - \tan^{-1}\left(\frac{\vec{r}_2 \cdot \vec{e}_y}{\vec{r}_2 \cdot \vec{e}_x}\right)\right] \tag{2.2.42}$$

For the normal velocity influence coefficient, we may write

$$A_{i,j} = \left[\frac{1}{2\pi} \frac{\vec{e}_{\theta_1}}{|\vec{r}_1|} - \frac{1}{2\pi} \frac{\vec{e}_{\theta_2}}{|\vec{r}_2|} \right] \cdot \vec{n}_i$$

$$= \frac{1}{2\pi} \left[\frac{\vec{e}_z x \vec{r}_1}{r_1^2} - \frac{\vec{e}_z x \vec{r}_2}{r_2^2}\right] \cdot \vec{n}_i \tag{2.2.43}$$

It should be noted that all of the vector quantities of Eqns. 2.2.42 and 2.2.43 are given with respect to the element coordinate system illustrated in Fig. 2.2.8.

2.2.7 Calculation of Airloads

In Appendix A, it is shown that the pressure at any point in an irrotational, ideal flow may be found with the unsteady Bernoulli equation,

$$P = P_\infty - \rho\left\{\frac{\partial\Phi}{\partial t} + \frac{1}{2} (\nabla\Phi)^2 \right\}. \tag{2.2.44}$$

One should recall that Eqn. 2.2.44 is valid for a fluid fixed coordinate system. In Section 2.2.4, the equivalent expression for a body fixed coordinate system was written as

$$P = P_\infty - \rho\left\{\frac{\partial\Phi}{\partial t} + (\vec{U}_\infty - \vec{U}_B - \vec{\omega} x \vec{r}) \cdot \nabla\Phi + \frac{1}{2} (\nabla\Phi)^2\right\}. \tag{2.2.45}$$

Eqn. 2.2.45 may be rewritten in a more convenient form for numerical computation by expressing $\nabla\phi$ as

$$\nabla\Phi = \nabla_s\Phi + \frac{\partial\Phi}{\partial n}\vec{e}_n \tag{2.2.46}$$

where $\nabla_s \equiv$ surface gradient. In addition, recall that the surface tangency condition was written in body fixed coordinates as

$$\frac{\partial\Phi}{\partial n} = -(\vec{U}_\infty-\vec{U}_B-\vec{\omega}_B x\vec{r})\cdot\vec{n}. \tag{2.2.47}$$

With Eqn. 2.2.46, Eqn. 2.2.45 may be expanded to yield

$$\begin{aligned} P = P_\infty-\rho\{&\frac{\partial\Phi}{\partial t} + (\vec{U}_\infty-\vec{U}_B-\vec{\omega}_B x\vec{r})\cdot\nabla_s\Phi \\ &+ \frac{\partial\Phi}{\partial n}(\vec{U}_\infty-\vec{U}_B-\vec{\omega}_B x\vec{r})\cdot n \\ &+ \frac{1}{2}(\nabla_s\Phi)^2 + \frac{1}{2}(\frac{\partial\Phi}{\partial n})^2\}. \end{aligned} \tag{2.2.48}$$

By substituting Eqn. 2.2.47 into Eqn. 2.2.48, we arrive at

$$\begin{aligned} P = P_\infty-\rho\{&\frac{\partial\Phi}{\partial t} + (\vec{U}_\infty-\vec{U}_B-\vec{\omega}_B x\vec{r})\cdot\nabla_s\Phi \\ &- \frac{1}{2}[(\vec{U}_\infty-\vec{U}_B-\vec{\omega}_B x\vec{r})\cdot\vec{n}]^2 \\ &+ \frac{1}{2}(\nabla_s\Phi)^2\}. \end{aligned} \tag{2.2.49}$$

Eqn. 2.2.49 provides the advantage of reducing the computation of the gradient of the distribution potential to the computation of its surface gradient. With Eqn. 2.2.49, the airloads on the body surface may be calculated by integrating the pressure force vector components over the surface.

2.3 The Boundary Layer Model

There were several general requirements which had to be met by the boundary layer model used in this work. The model had to be able to predict both laminar and turbulent portions of the boundary layer flow as well as the location of the transition region between them as indicated in Fig. 2.3.1. Unsteady effects had to be an intrinsic part of the formulation since they have been shown to contribute to stall delay in a significant manner [see McCroskey and Phillippe (1975)]. The boundary layer model had to also be capable of making reasonably accurate predictions in the vicinity of separation so that appropriate separation criteria could be applied. In addition, calculation times had to be reasonable.

2.3.1 Overview of Unsteady Boundary Layer Codes

Several investigators have made extensive calculations using unsteady turbulent boundary layer codes in recent years, e.g., Nash, Carr, and Singleton (1975); Dwyer and McCroskey (1971); Telionis (1975); Daneshyar and Mugglestone (1978); and Lyrio, Ferziger, and Kline (1981). Notable among the codes which have been developed are the several variations of a differential boundary layer model due to Nash, et al. (1978). This model met most of the general requirements in that it predicts both laminar and turbulent flow, includes unsteady effects, and is capable of predicting flow in the vicinity of separation. In addition, the model has been applied to dynamic stall problems and has been shown to give good results according to McCroskey and Phillippe (1975). While the computational time required

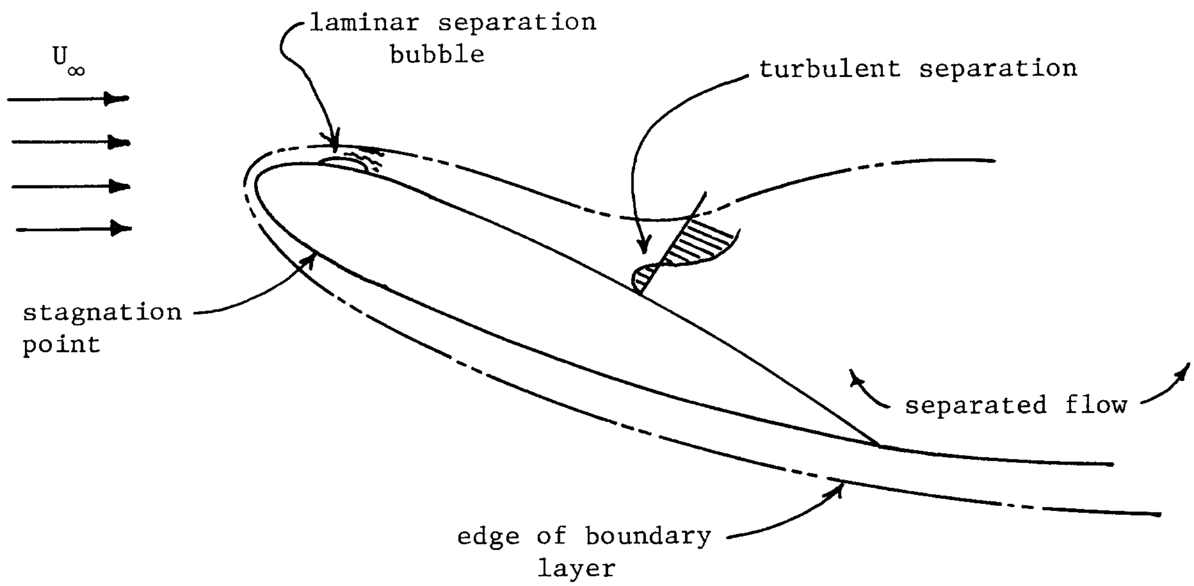

Fig. 2.3.1 Boundary Layer Characteristics of an Airfoil at High Incidence

for this method is not excessive in comparison with other differential boundary layer codes, it was felt that an integral technique might be more appropriate due to the large number of boundary layer calculations required.

Only very recently have integral techniques for unsteady turbulent boundary layers appeared in the literature. The method due to Daneshyar and Mugglestone (1978) utilizes the unsteady momentum integral equation along with the entrainment equation and a skin-friction equation derived from the Coles (1956) velocity profile. Other assumptions and linearizations which are a part of this formulation restrict its use to cases of small amplitude periodic fluctuations of the freestream. Very recently, however, Lyrio, Ferziger, and Kline (1981) formulated and tested a similar integral technique which gives excellent results for the steady turbulent flows of Tillman, Herring and Norbury; Stratford, Samuel and Joubert [see Coles and Hirst (1968) for these four flows]; Kim (1980); Simpson and Strickland (1977); and Wieghardt [see Kim (1980)]. More importantly, this method predicts the unsteady turbulent boundary layer data of Karlson (1959), and Houdeville, et al. (1979), and compares well with the finite difference methods of McCroskey and Philippe (1975), and Singleton and Nash (1974) while being an order of magnitude faster.

2.3.2 Present Boundary Layer Model

The turbulent boundary layer analysis used in the present work is essentially that due to Lyrio et al. (1981). This method gives good results prior to actual separation of the boundary layer as evidenced in Figures 2.3.2 and 2.3.3. Predictions near separation as well as

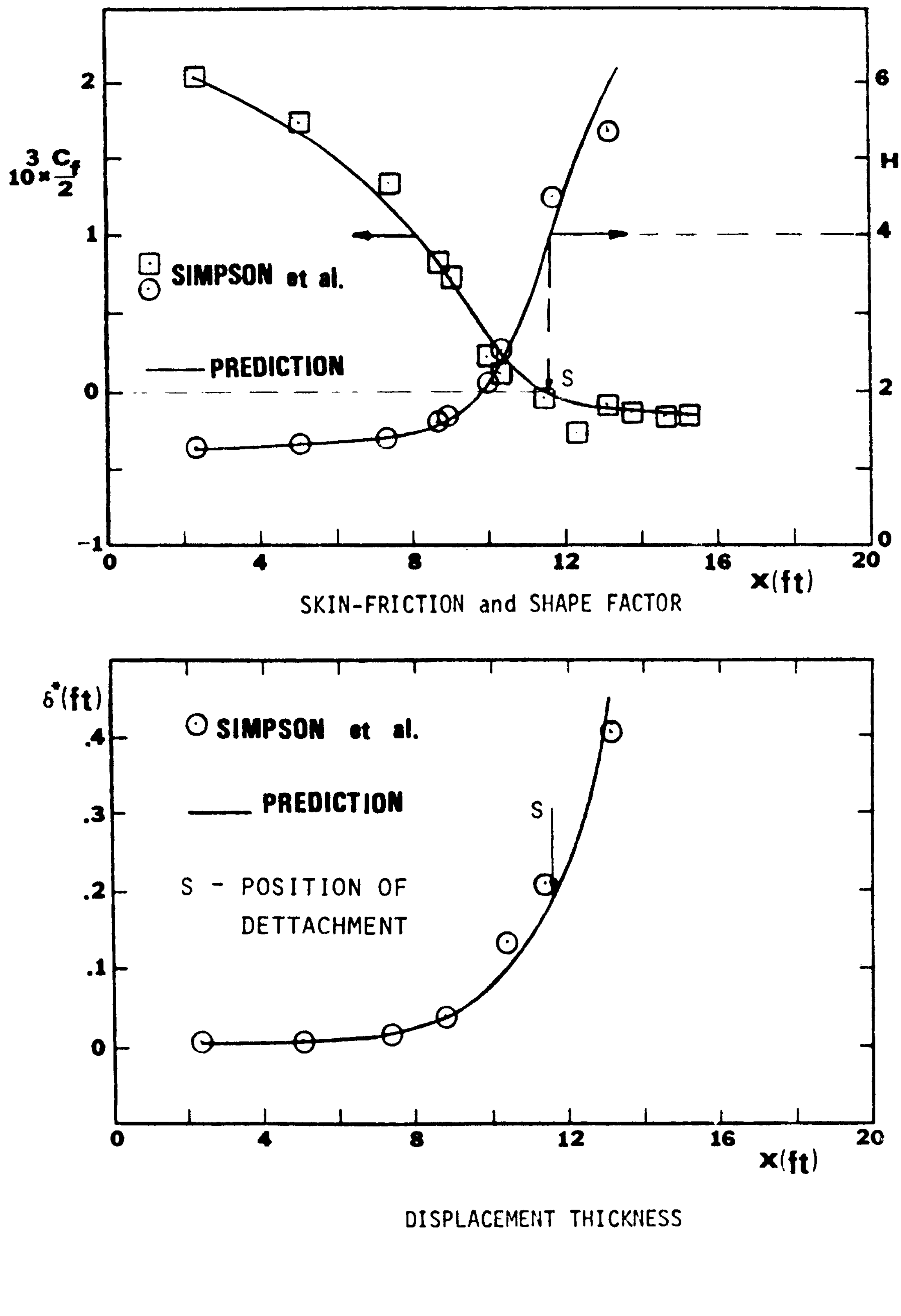

Fig. 2.3.2 Typical Predictive Capability of Lyrio et al. (1981) Boundary Layer Code for Steady Separating Flows

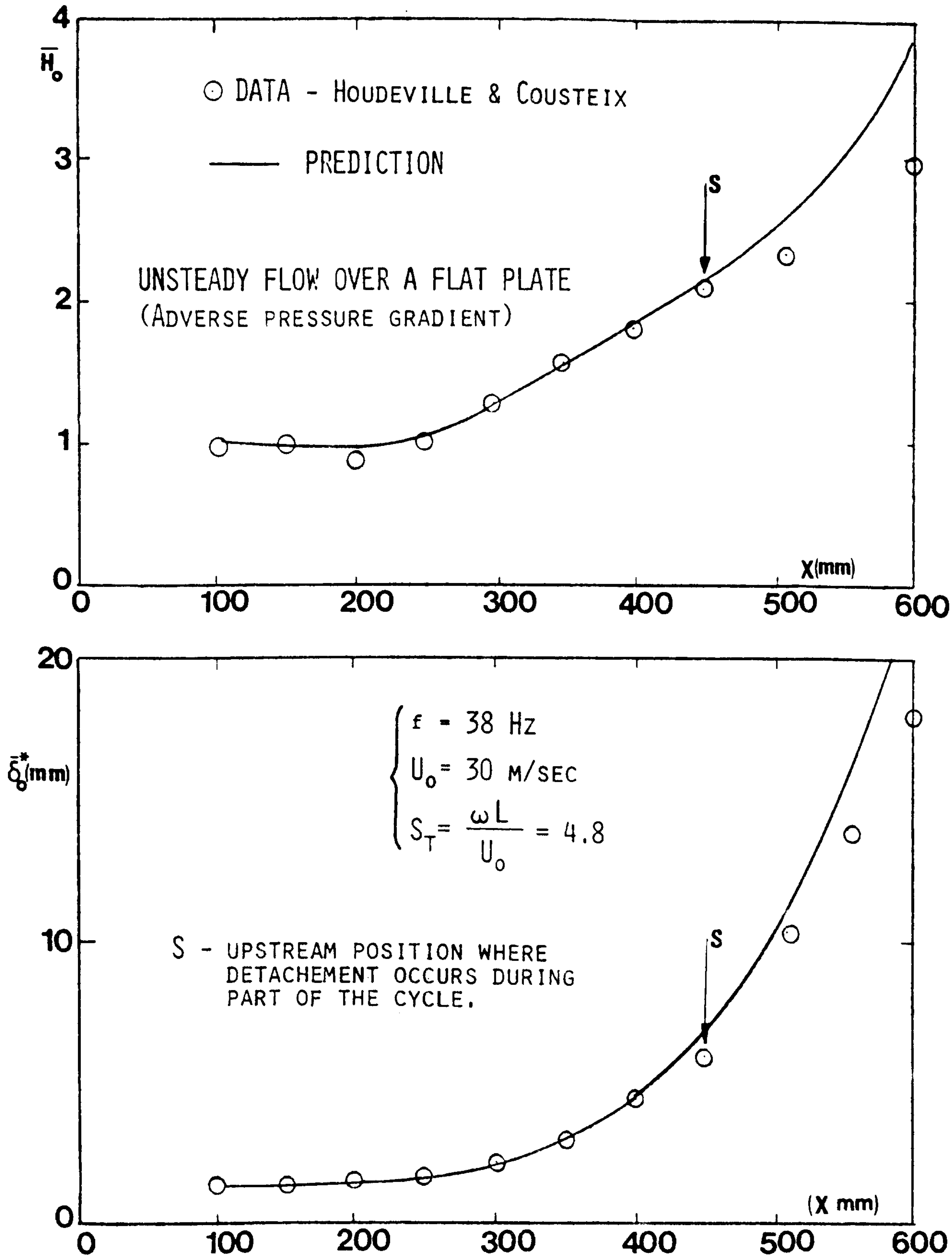

Fig. 2.3.3 Typical Predictive Capability of Lyrio et al. (1981) Boundary Layer Code for Unsteady Separating Flows

downstream of separation tend to be very sensitive to freestream velocity gradients as evidenced by the present author's experience with the analysis. The formulation for the laminar portion of the boundary layer is based upon an extension of Thwaites method [see Cebecci and Bradshaw (1977)]. The major extension of Thwaites method is the inclusion of unsteady terms in the momentum integral equation.

The unsteady momentum integral equation which is valid for both laminar and turbulent flow can be written as

$$\frac{1}{U_e^2}\frac{\partial}{\partial t}(U_e\,\delta^*) + \frac{\partial\theta}{\partial x} + \frac{1}{U_e}\frac{\delta U_e}{\partial x}(2\theta + \delta^*) = \frac{C_f}{2} \tag{2.3.1}$$

where U_e, θ, δ^* and C_f are the freestream velocity, momentum thickness, displacement thickness, and friction factor, respectively. For the laminar formulation, a pressure gradient parameter, λ, is defined as

$$\lambda = \frac{\theta}{U_e} R_\theta \left(\frac{\partial U_e}{\partial x} + \frac{1}{U_e}\frac{\partial U_e}{\partial t}\right) \tag{2.3.2}$$

where R_θ is the Reynolds number based on U_e and θ. In order to obtain a solution to the laminar case a connection between $C_f/2$, θ, and δ^* must be made. The following correlations were obtained based on wedge flow solutions which make this connection:

$$\frac{C_f}{2} = \frac{1.91 - 4.13\Lambda}{Re^*}$$

$$H = (0.680 - 0.922\Lambda)^{-1} \tag{2.3.3}$$

$$\Lambda = 0.325 - 0.130\lambda H^2$$

Here, H is the usual shape parameter, δ^*/θ, Λ is the blockage factor δ^*/δ, and Re^* is the Reynolds number based on U_e and δ^*.

The turbulent boundary layer model of Lyrio, Ferziger, and Kline utilizes the entrainment equation given by

$$\frac{1}{U_e}\frac{\partial}{\partial x}\left[U_e\,(\delta - \delta^*)\right] = F \tag{2.3.4}$$

The entrainment function F is calculated from the following auxiliary equations

$$\begin{aligned}
\frac{dF}{dx} &= \frac{.025}{\delta}\,(Fe - F) \\
Fe &= 4.24\;Ke\left(\frac{\Lambda}{1-\Lambda}\right)^{.916} \\
Ke &= .013 + .0038e^{-\beta/15} \\
\beta &= \frac{\delta^*}{\tau_w}\frac{dP}{dx}
\end{aligned} \tag{2.3.5}$$

where t_w is the wall shearing stress and dP/dx is the streamwise pressure gradient. Shape factor relationships are obtained from the following general velocity profile.

$$\begin{aligned}
\frac{U}{U_e} &= 1 + V_T \ln\left(\frac{y}{\delta}\right) - V_B\,\cos^2\left(\frac{\pi y}{2\delta}\right) \\
V_T &= \frac{1}{.41}\sqrt{\frac{C_f}{2}}\,(\mathrm{sgn}\;C_f/2) \\
V_B &= 2(\Lambda - V_T) \\
\frac{C_f}{2} &= \frac{\tau_w}{\rho U_e^2}
\end{aligned} \tag{2.3.6}$$

where U is the velocity in the boundary layer at a distance y from the wall and ρ is the fluid density. The skin friction law is given by

$$\frac{C_f}{2} = .051 \left| 1-2\Lambda \right|^{1.732} \left(\frac{Re^*}{\Lambda}\right)^{-.268} \text{sgn}\ (1-2\Lambda) \qquad (2.3.7)$$

2.3.3 Transition and Separation

Transition of the laminar boundary layer (found near the forward stagnation point of the airfoil) to a turbulent boundary layer can be triggered in one of several ways. In the first case, a separation bubble can be formed near the leading edge which consists of a laminar separation and turbulent transition with subsequent reattachment. In some cases the shear layer may not reattach. In the present model the streamwise extent of the separation bubble is assumed to be small and a turbulent boundary layer is assumed to begin at the point of laminar separation given by a value of $H \geqslant 4.0$. A model for the separation bubble has been proposed and tested by Roberts (1980) and Arena and Mueller (1980) and should eventually be included in the boundary layer code. In the absence of a laminar separation bubble, transition may occur by virtue of laminar instabilities which can be predicted using the criteria due to Cebecci and Smith (1974)

$$R_{\theta tr} = 1.174 \left(1 + \frac{22,400}{Re_{x_{tr}}}\right) Re_{x_{tr}}^{0.46} \qquad (2.3.8)$$

Here R_θ and Re_x are Reynolds numbers based on the momentum thickness and distance from the forward stagnation point, respectively. As pointed out by McCroskey (1975), this latter type of instability occurs only at high Reynolds numbers and low angles of attack.

Separation criteria associated with the unsteady boundary layer is more complicated than for the steady case in which it is generally assumed that separation occurs at a position of zero wall shear stress. For example, it is evident that no separation occurs from a flat plate oscillating parallel to its own surface in an otherwise still fluid even though the wall shear stress goes to zero twice during each cycle. Several investigators have examined the Moore (1958)-Rott (1956)-Sears (1956) model and have concluded that if properly interpreted, it yields an unsteady boundary layer separation criteria. Basically, the model requires that the shear stress must vanish at some point within the boundary layer and, in addition, the velocity relative to a coordinate frame moving with the separation point must vanish at the same location. This criteria is also consistent with the findings of Nash and Patel (1975) in that they conclude that separation will occur if and only if the typical reversed flow velocities (which their model calculates) exceed the rate of penetration of the reversed flow into the oncoming boundary layer. An alternate separation criteria is based on monitoring any rapid increase in the various boundary parameters such as the displacement thickness δ^* or the v component of velocity normal to the surface. Nash and Patel (1975), in fact, use a crude criteria to enable them to locate the approximate location of separation by noting the region where $\delta^*/C > 0.1$ where C is the airfoil chord length. In the work of Lyrio, Ferziger, and Kline the "fully developed" separation point is found to occur when $\Lambda = 0.5$. The "intermittent" separation point occurs prior to the "fully developed" separation point. The intermittent separation point occurs when

$$H > \frac{2 - \Lambda}{1 - \Lambda} \tag{2.3.9}$$

according to the Sandborn (1961) correlation. the intermittent separation point is much more reliably predicted than the fully developed separation point and was thus used as the point of introduction of the nascent vortex in the present work. The exact point in the separation region at which the nascent vortex should be introduced for optimum results is presently unknown. Further study regarding this detail should be undertaken.

2.3.4 Numerical Solution of Boundary Layer Equations

Numerical solutions are obtained in the present model using an explicit finite difference formulation of Eqn. 2.3.1. For the laminar formulation equations 2.3.1, 2.3.2, and 2.3.3 can be cast in the following form:

$$A \frac{\partial \delta^*}{\partial x} = B \tag{2.3.10}$$

This equation is integrated over an interval Δx using a fourth order Runge-Kutta method to yield the variation of δ^* as a function of x at a given time step. Time derivatives in the coefficient B are obtained from backward differences while derivatives with respect to x are obtained from forward differences. These derivatives are held constant over the integration interval Δx. The integration interval Δx is further subdivided into at least eight subintervals. For the turbulent formulation using equations 2.3.1, 2.3.4, 2.3.5, 2.3.6, and 2.3.7 a pair of simultaneous equations results which can be symbolized as:

$$\begin{bmatrix} A_{11} & A_{12} \\ A_{21} & A_{22} \end{bmatrix} \begin{Bmatrix} \frac{\partial \delta^*}{\partial x} \\ \frac{\partial \Lambda}{\partial x} \end{Bmatrix} = \begin{Bmatrix} B_1 \\ B_2 \end{Bmatrix} \qquad (2.3.11)$$

A fourth order Runge-Kutta method is used to yield simultaneous values of δ^* and Λ as a function of x.

In the work completed to date the time dependent terms in the code have been suppressed such that the solution obtained is of a quasi-steady nature.

3. CALCULATION RESULTS

Contained in the following sections are calculation results illustrating the current capability of DYNA2 to predict steady and unsteady, attached flows and steady, separated flows over two-dimensional airfoils. Possible enhancements to the model which would improve the accuracy of those calculations are outlined.

3.1 Steady, Attached Flows

Figures 3.1.1 through 3.1.4 are representative of the capability of DYNA2 to predict the pressure distributions on two-dimensional bodies resulting from steady flows without boundary layer separation. The calculation results presented are for the cases of a cylinder and typical turbulent and laminar airfoils. The model does an excellent job for the cases of the cylinder and turbulent airfoil but is less successful for the laminar airfoil.

Figures 3.1.3 and 3.1.4 illustrate calculation results for the same laminar airfoil at identical angles of attack. The only difference in the two calculations is a slight repositioning of the doublet panels near the nose. The sensitivity of the calculations to this modification is a consequence of the use of flat, uniform strength doublet panels as the basic surface modeling elements. Since only one degree of freedom (the doublet panel strength) is allowed for each element by this representation, there can be only one boundary condition enforced on each element. The choice made for DYNA2 is a surface tangency condition applied at the centroid of the elements. A higher order doublet strength distribution on the panels would allow extra degrees of freedom which could be utilized to enforce

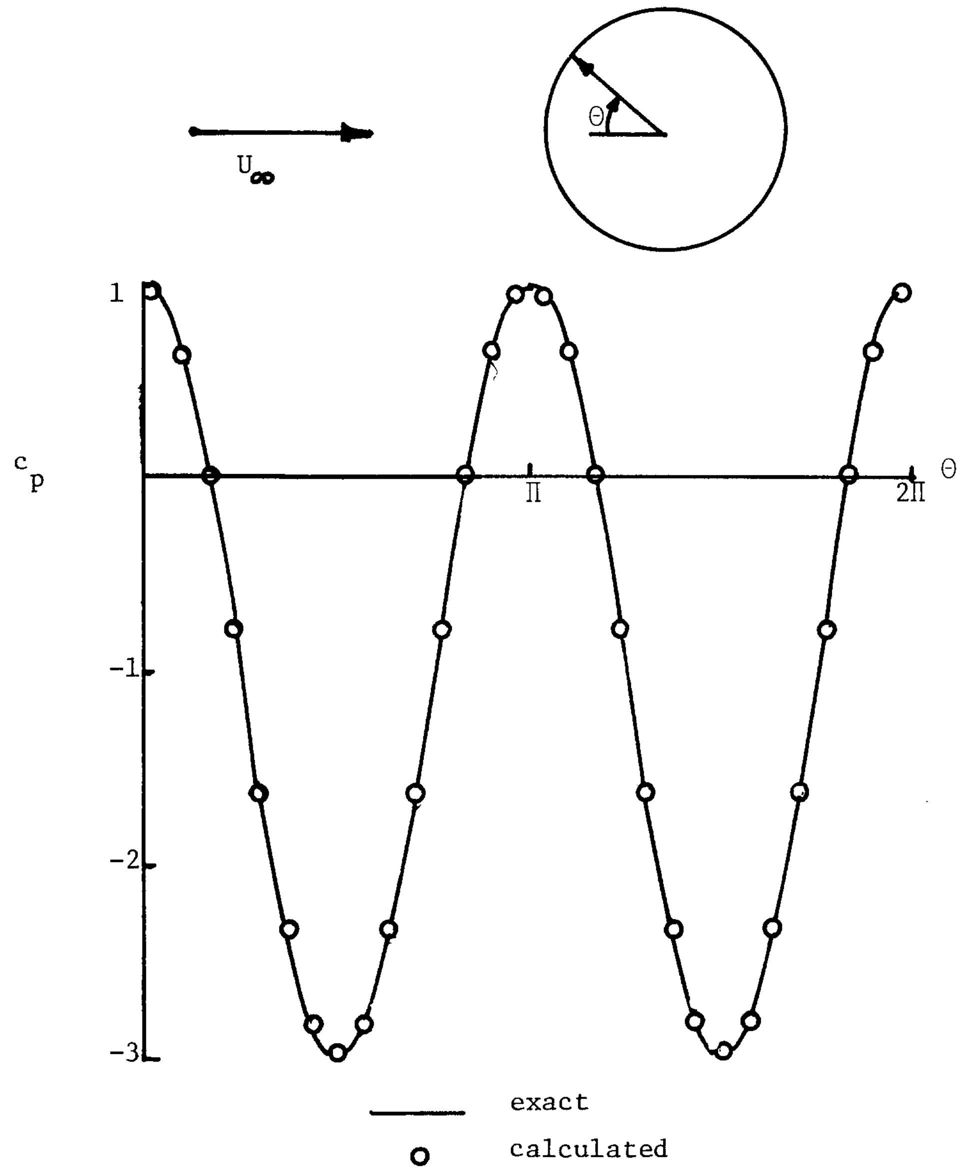

Figure 3.1.1 Pressure Distribution on a Two-Dimensional Cylinder

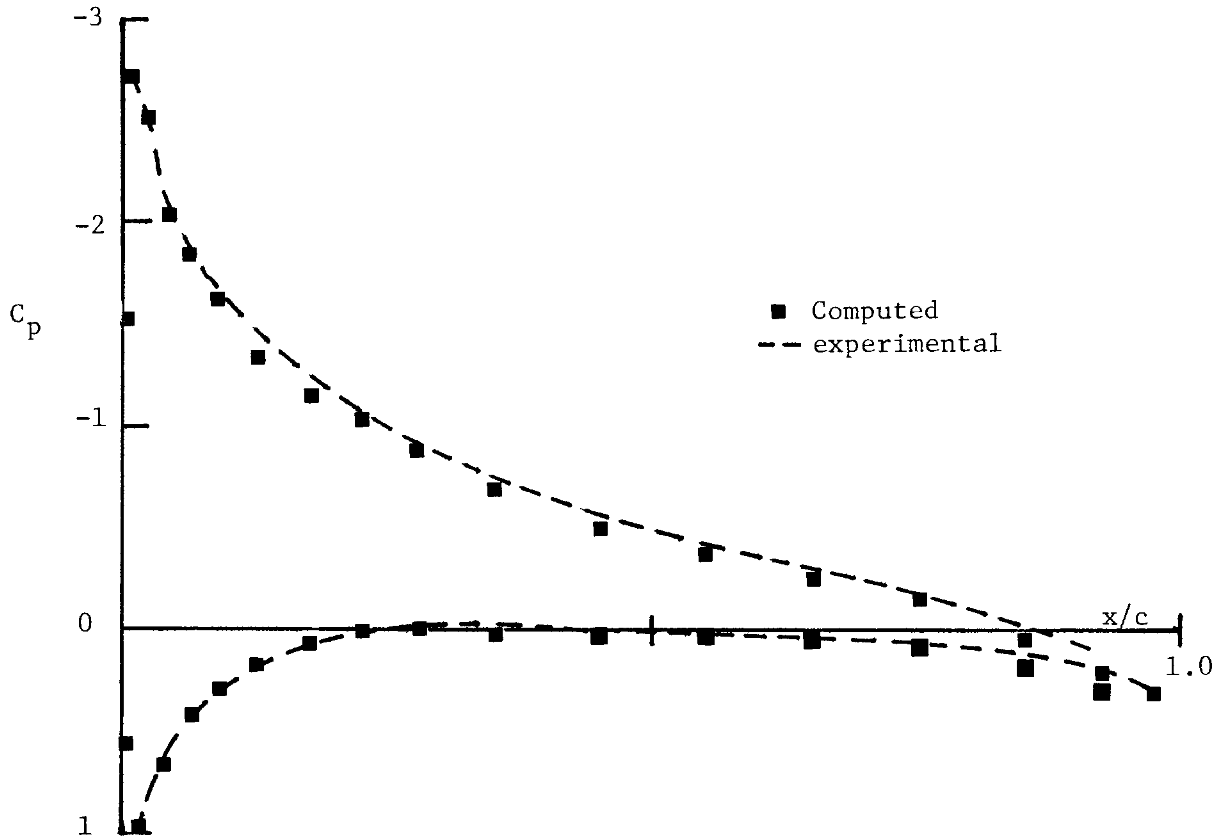

Figure 3.1.2 Pressure Distribution on a NACA 0015 Airfoil at 6° Angle of Attack

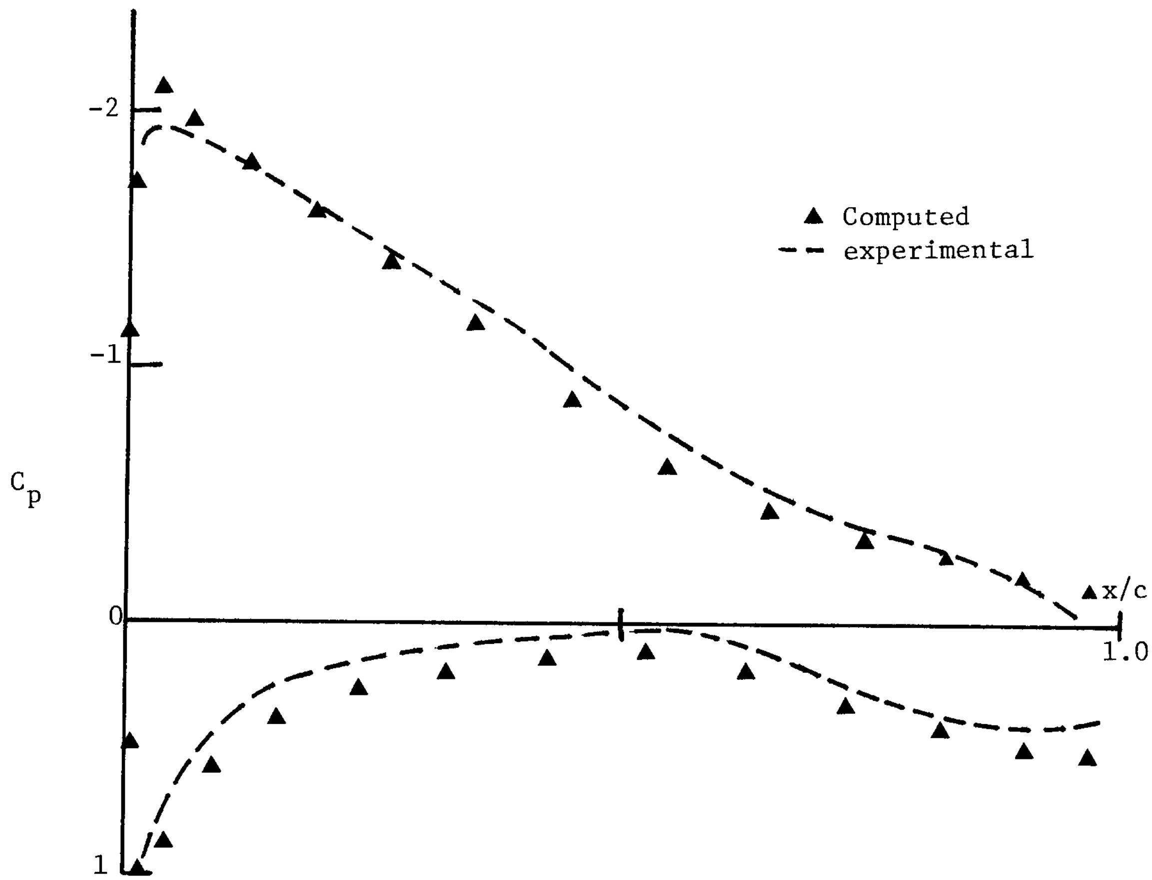

Figure 3.1.3 Pressure Distribution on a Laminar Airfoil at 6.1° Angle of Attack

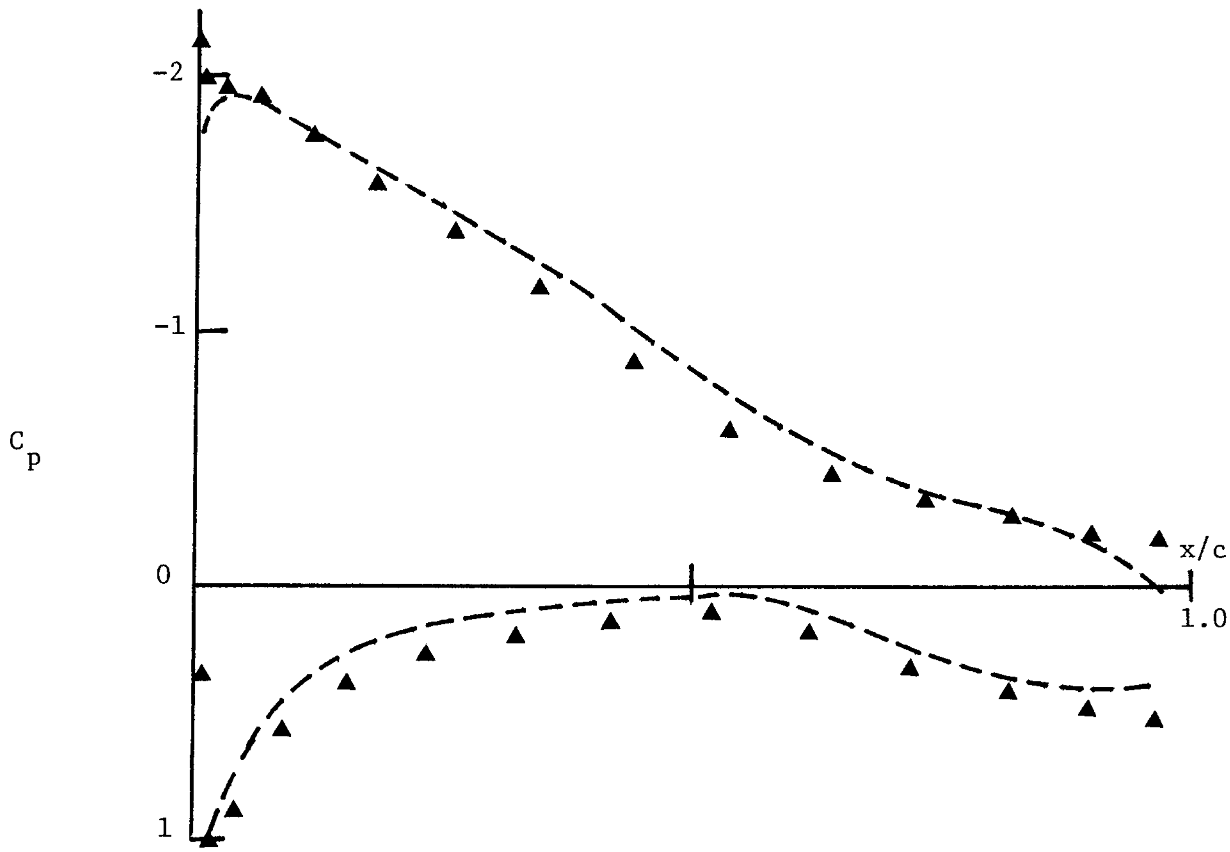

Figure 3.1.4 Same as Figure 3.1.3 Except With Slightly Modified Leading Edge Modeling

additional boundary conditions. These might include multiple surface tangency conditions on individual elements and a requirement for continuity of the surface fluid velocity between adjacent panels.

The use of planar surface elements causes the centroids of the elements to actually be below the true curved airfoil surface in most cases. For turbulent airfoils and the majority of the surface of laminar airfoils, this presents no problem since the deviation will be small if the curvature is small. However, difficulties can arise near the leading edge of laminar airfoils where the radius of curvature is typically small and the rate of change of fluid velocity with respect to a surface coordinate is large. Many, very small elements are required to adequately model regions such as this and there is little tolerance in their positioning. The situation could be improved by utilizing curved doublet panels which would more closely follow the true airfoil surface.

One disadvantage of using curved, multiple degree of freedom doublet panels as the basic surface modeling element is that the corresponding influence coefficients can not be evaluated in closed form. Their calculation through a numerical integration scheme would increase the computation time requirments significantly as compared to the planar, uniform strength elements. However, on the basis of the current calculations, it appears that the more complex elements are necessary to achieve a satisfactory degree of flexibility and reliability in calculations for any arbitrary airfoil which one might wish to consider.

3.2 Steady, Attached Flows

Figures 3.2.1 through 3.2.4 are typical of calculations for non-separated flows over airfoils involved in unsteady motions. Figure 3.2.1

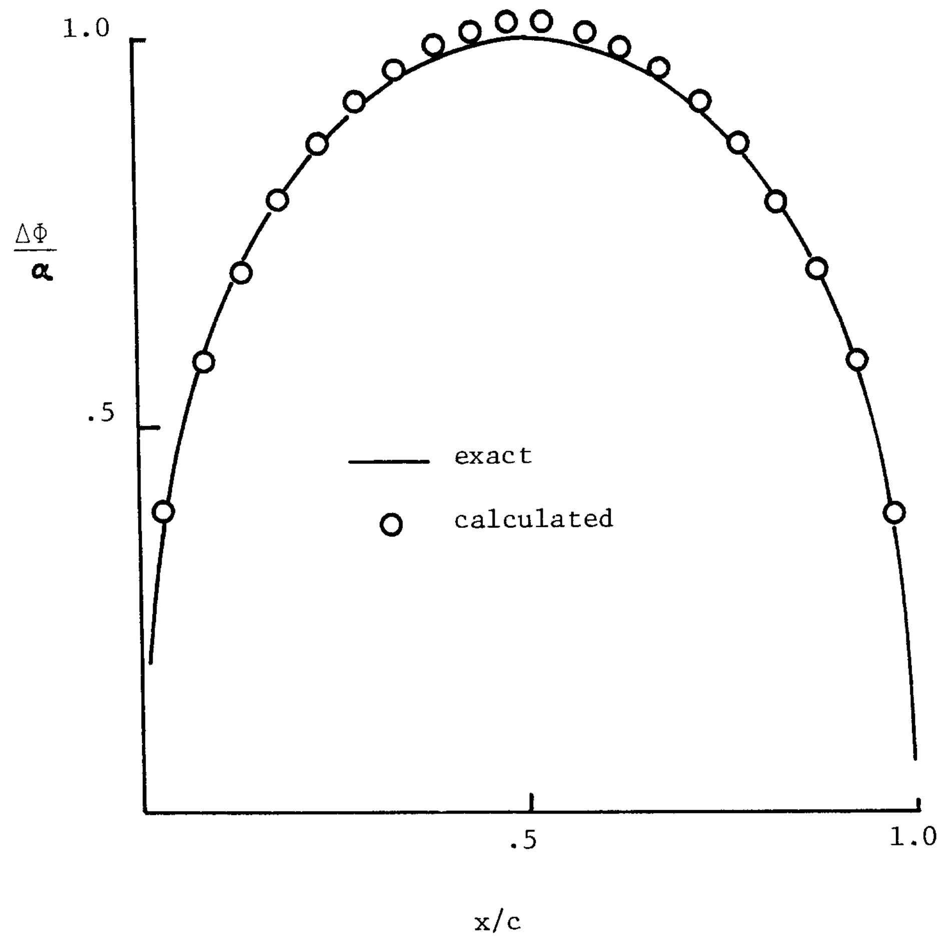

Figure 3.2.1 Potential Jump Distribution on an Impulsively Started Flat Plate

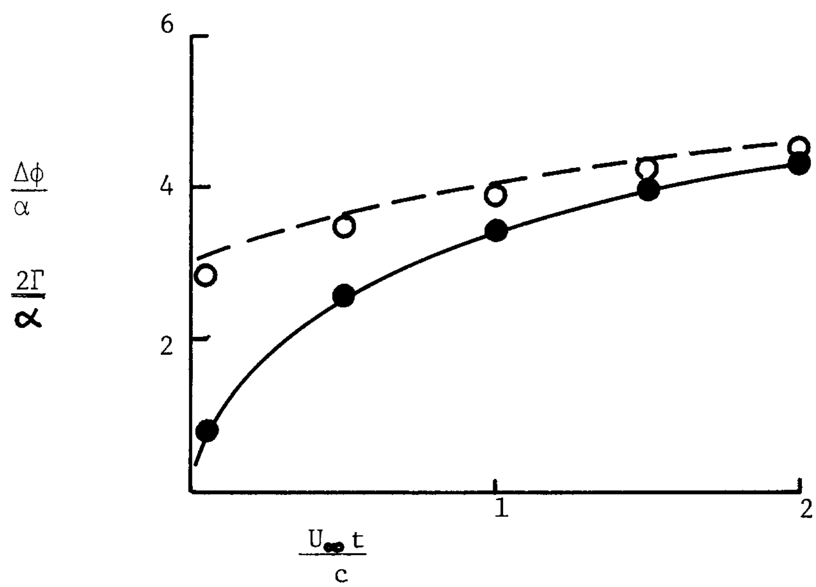

---- indicial lift - Wagner's Function

O indicial lift - present method

—— indicial circulation - R. T. Jones

● indicial circulation - present method

Figure 3.2.2 Impulsively Started Flat Plate Airfoil

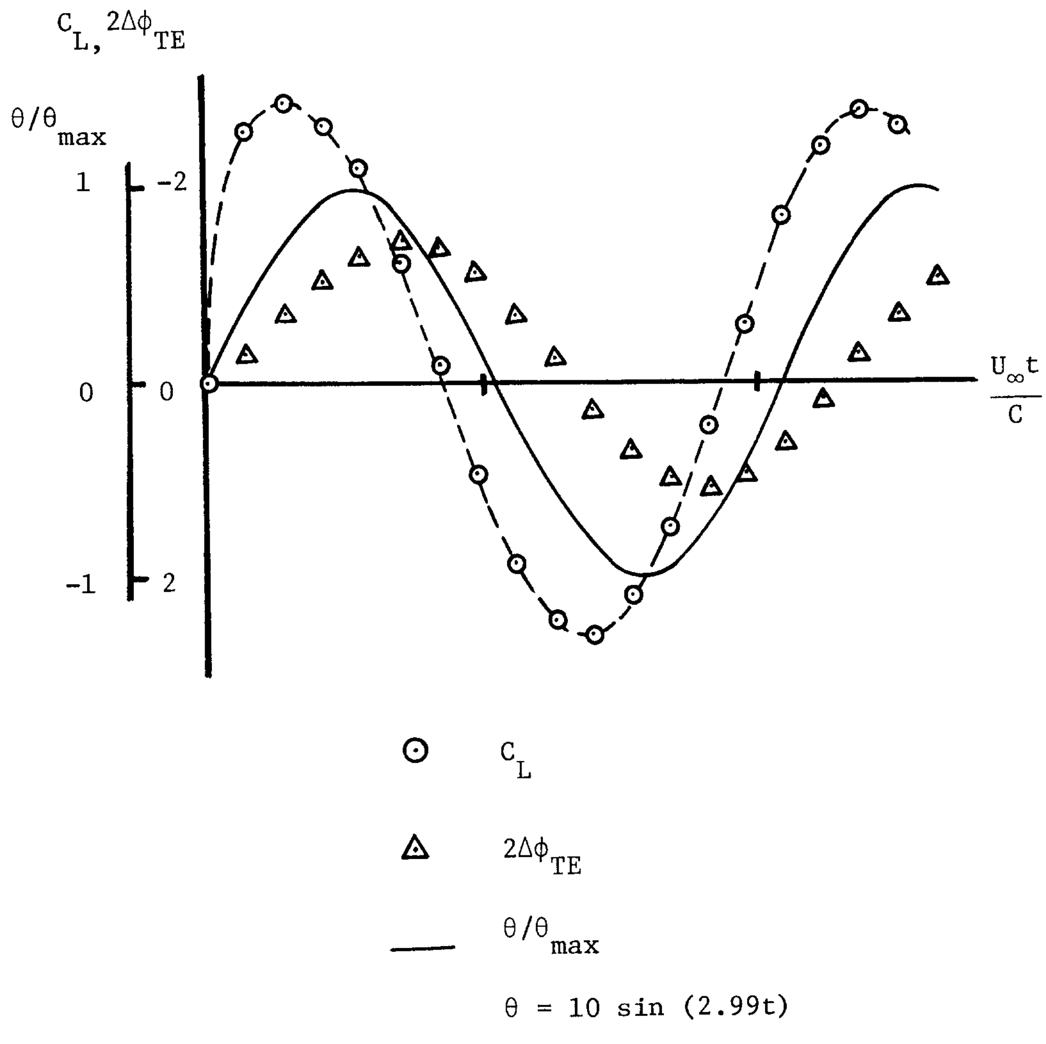

Figure 3.2.3 Variation of Lift and Circulation on an Oscillating NACA 0015 Airfoil

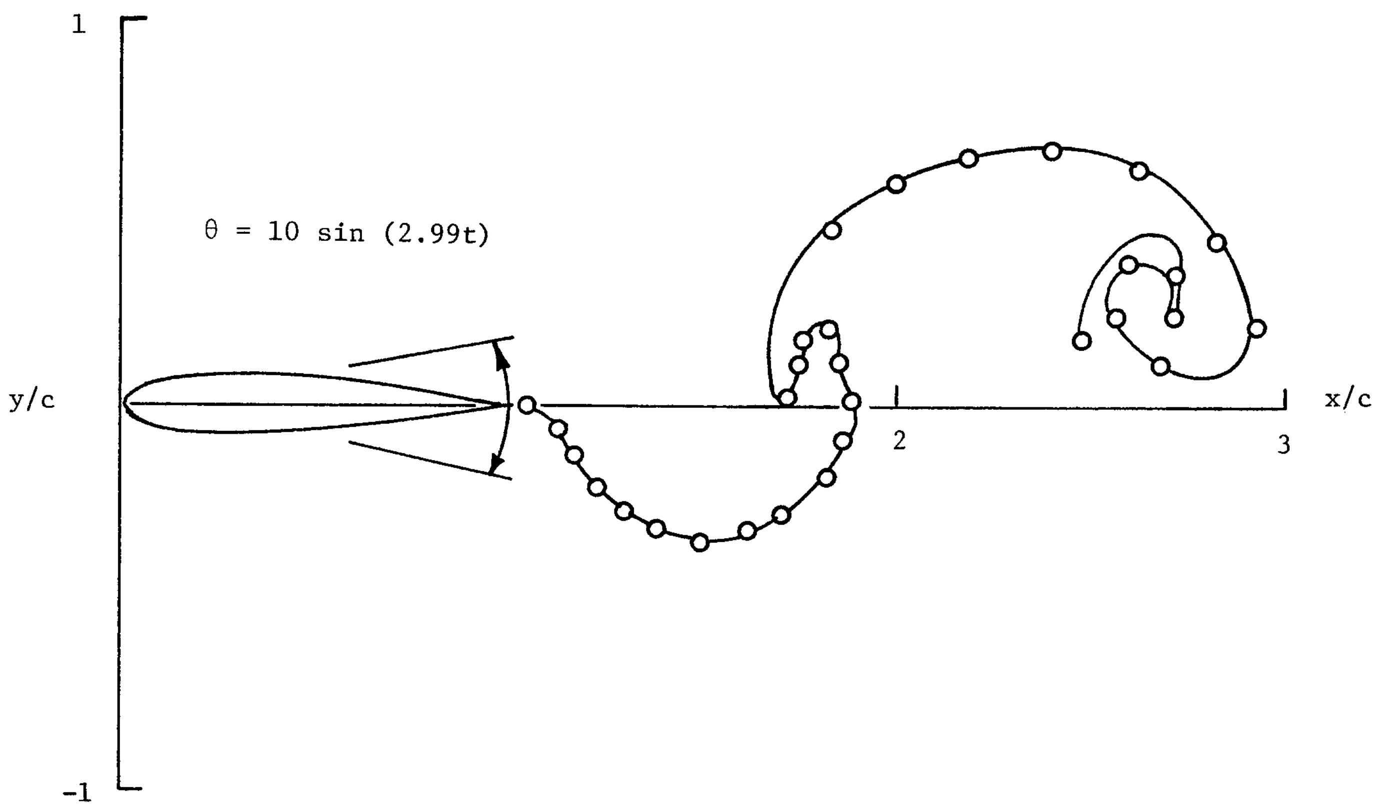

3.2.4 Wake Geometry Behind an Oscillating NACA 0015 Airfoil presents a comparison between the computed and exact potential jump distributions over an impulsively started flat plate airfoil at the starting instant. Figure 3.2.2 illustrates the subsequent development of the circulation and lift.

Figures 3.2.3 and 3.2.4 present the results of calculations for a NACA 0015 airfoil oscillating in pitch. From Figure 3.2.3, it is noted that the maximum lift leads the maximum angle of attack due to the apparent mass effects. The sectional circulation, however, lags behind the angle of attack as a result of the downwash produced by the vorticity in the wake. The wake geometry produced by the oscillating airfoil motion is depicted in Figure 3.2.4. It is felt that the prediction of realistic wake geometries such as this will be an essential element in the eventual calculation of the unsteady airloads on airfoils in dynamic stall.

3.3 Quasi-Steady, Separated Flows

Figures 3.3.1 through 3.3.3 illustrate the comparison between computed and experimentally determined lift and drag curves for a NACA 0015 airfoil at three Reynolds numbers. The boundary layer separation points for these calculations were predicted on the basis of pressure distributions for steady, nonseparated flows at equivalent angles of attack. The potential and boundary layer calculations were not coupled in a step-by-step solution procedure. The resulting variations of separation point location with respect to angle of attack are illustrated in Figure 3.3.4.

From the figures, it is noted that the lift curves are predicted with reasonable accuracy for the $R_e = .665 * 10^6$ and $1.27 * 10^6$ cases and less well for the $R_e = .043 * 10^6$ case. The loss of accuracy there is most probably a consequence of the utilization of boundary layer correlations

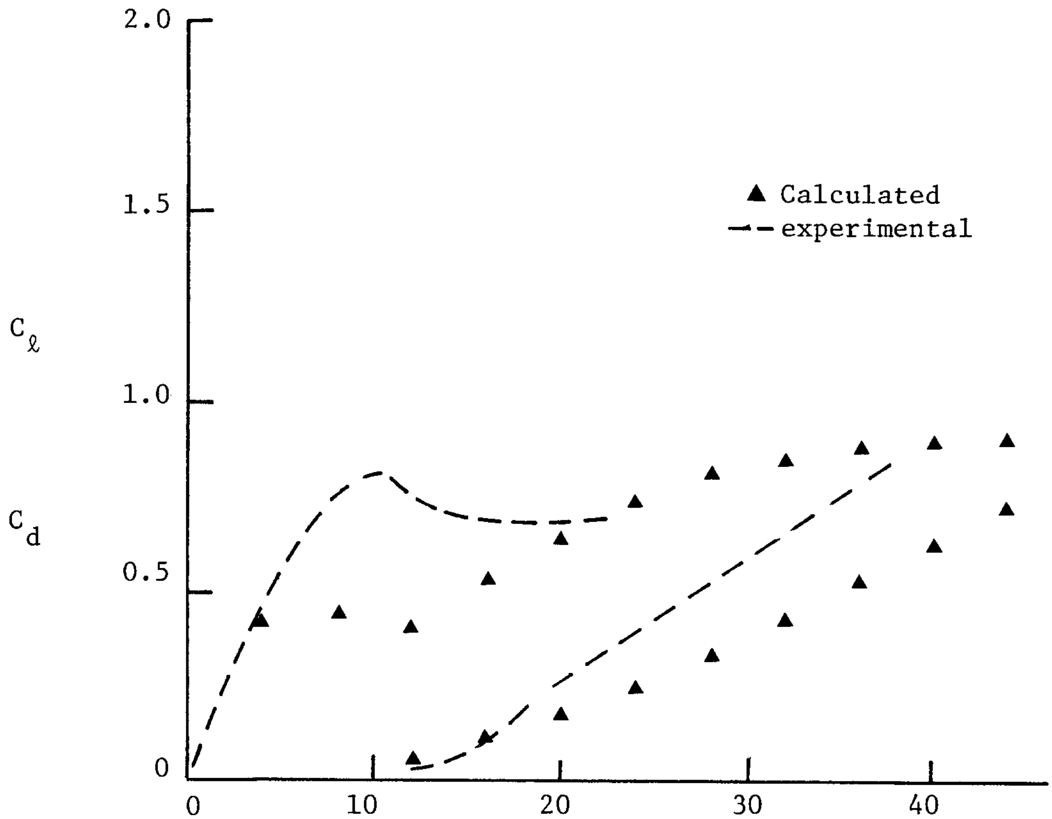

Figure 3.3.1 Variation of Lift and Drag Coefficients for a NACA 0015 at Re = 42,900

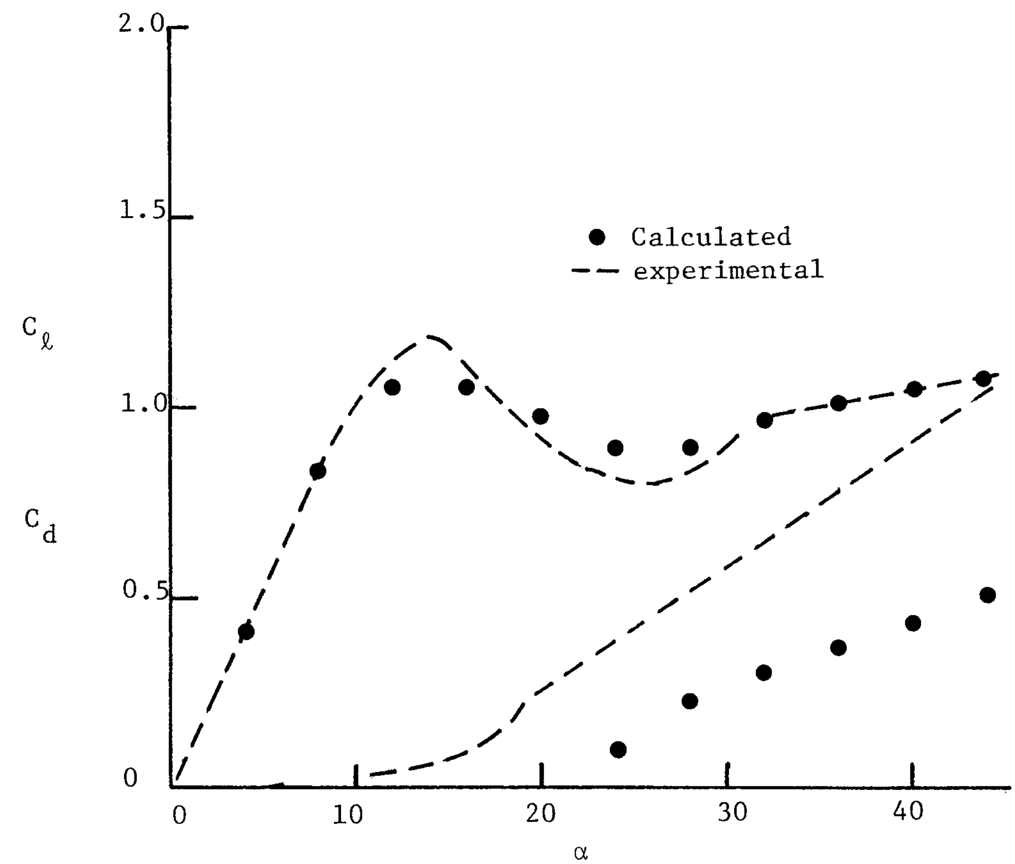

Figure 3.3.2 Variation of Lift and Drag Coefficients for a NACA 0015 at Re = 655,000

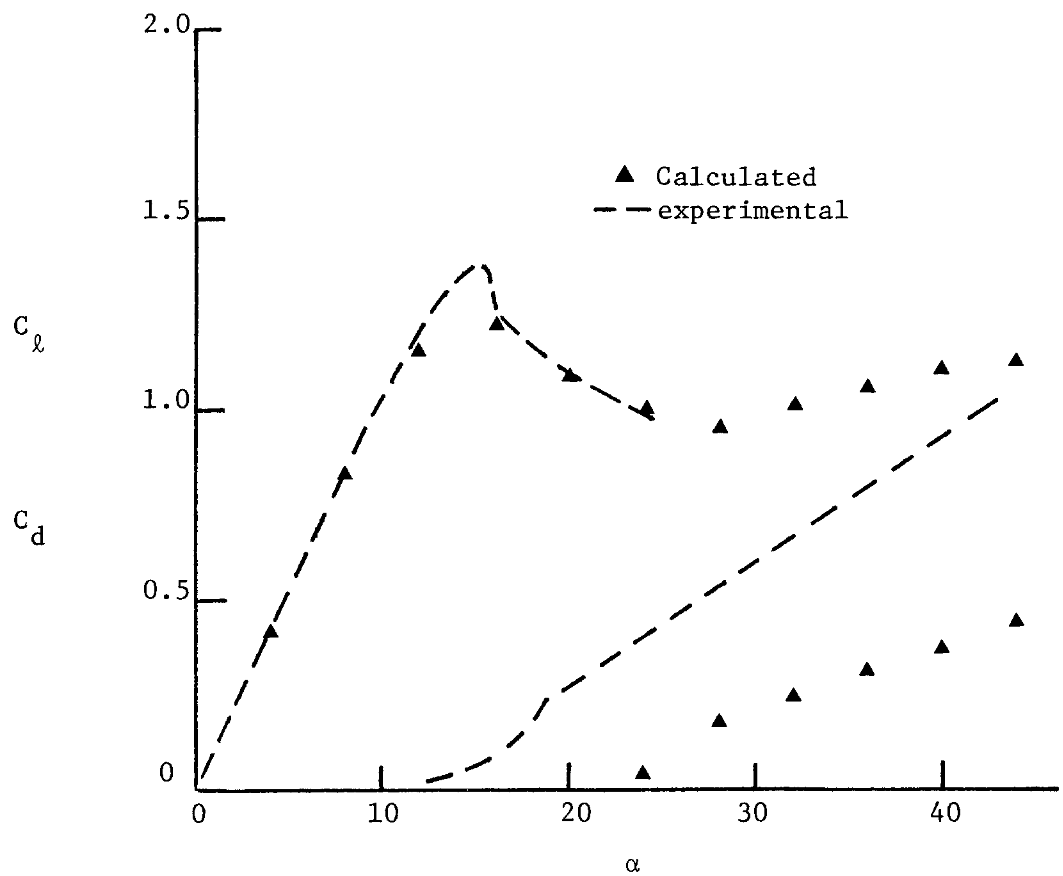

Figure 3.3.3 Variation of Lift and Drag Coefficients for a NACA 0015 Airfoil at Re = 1,270,000

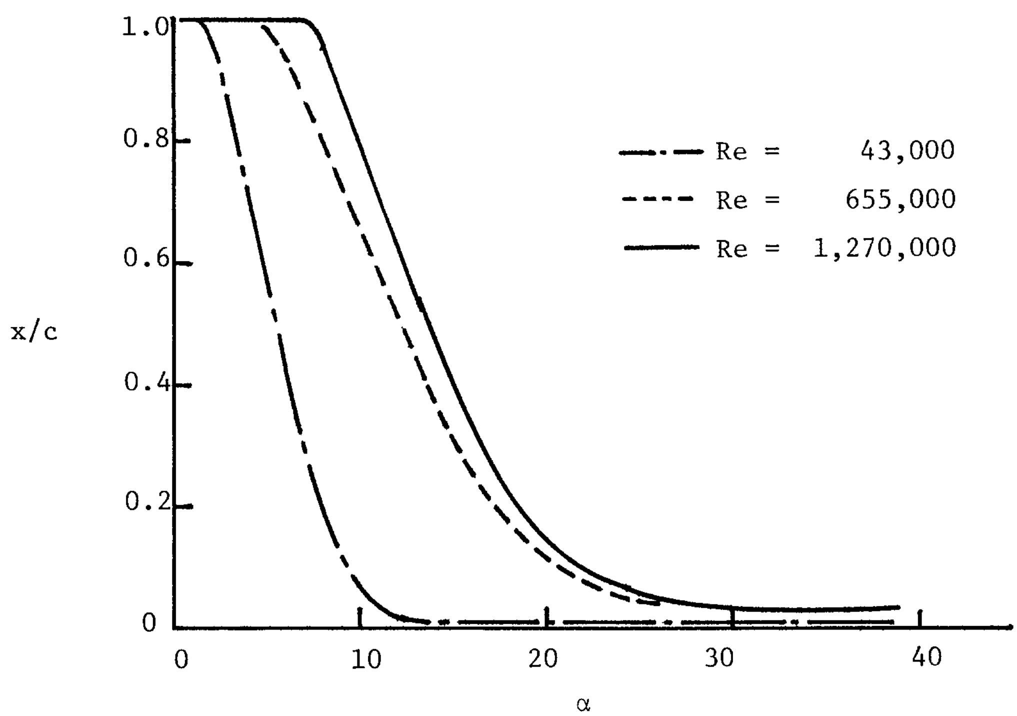

Figure 3.3.4 Variation of Boundary Layer Separation Point Location for a NACA 0015 Airfoil

at R_e below their range of applicability. It may also be noted that the drag is underestimated at all three Reynolds numbers.

As was described in the previous chapter, a reduction factor is utilized in determining the rate of vorticity shedding at the boundary layer separation point. Since the value of $\partial\phi/\sigma t$ and pressure in the separated region are directly related to the shedding rate, the reduction factor strongly affects the calculated airloads. The reduction factor for the illustrated calculations was chosen such that the best prediction of lift at post-stall angles of attack was achieved. The resulting value was 0.5. Unfortunately, this reduction factor value did not yield acceptable accuracy for the drag coefficients.

It is expected that there exists a unique combination of the reduction factor and separation point location that will yield satisfactory predictions of both lift and drag. Figure 3.3.5 illustrates a slight modification of the separation point versus angle of attack relationship for the $R_e = .655 * 10^6$ case. When used with a reduction factor of 0.55 instead of 0.5, the calculated lift and drag are significantly improved as illustrated in Figure 3.3.6. A modification of separation point location such as that in Figure 3.3.5 is likely to occur when the potential and boundary layer routines are directly coupled. Figure 3.3.7 illustrates the calculated <u>separated</u> flow pressure distribution for $\alpha = 24°$, $R_e = .655 * 10^6$. The difference between this distribution and the nonseparated distribution which was used in the boundary layer calculations is apparent.

In recent attempts to couple the viscid and inviscid calculations on a step-by-step basis, unrealistically erratic movement of the boundary layer separation point was predicted. This was a result of attempting to utilize

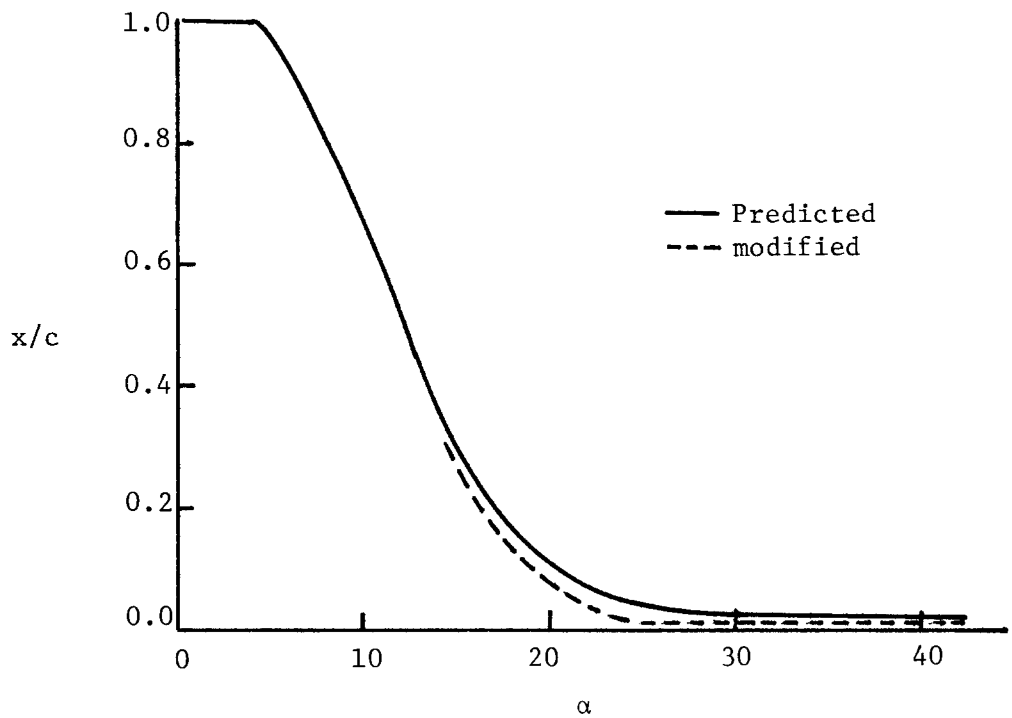

Figure 3.3.5 Alternate Variation of Boundary Layer Separation Point Location for a NACA 0015 Airfoil at Re = 655,000

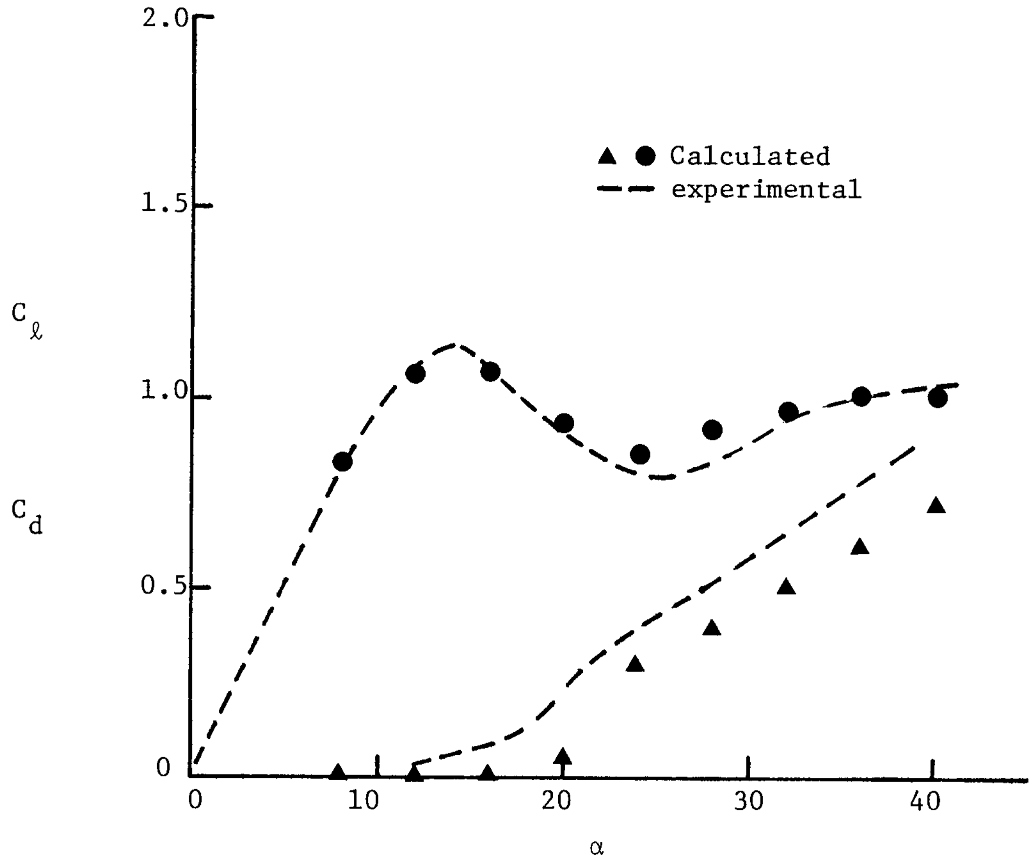

Figure 3.3.6 Variation of Lift and Drag Coefficients for a NACA 0015 Airfoil at Re = 655,000

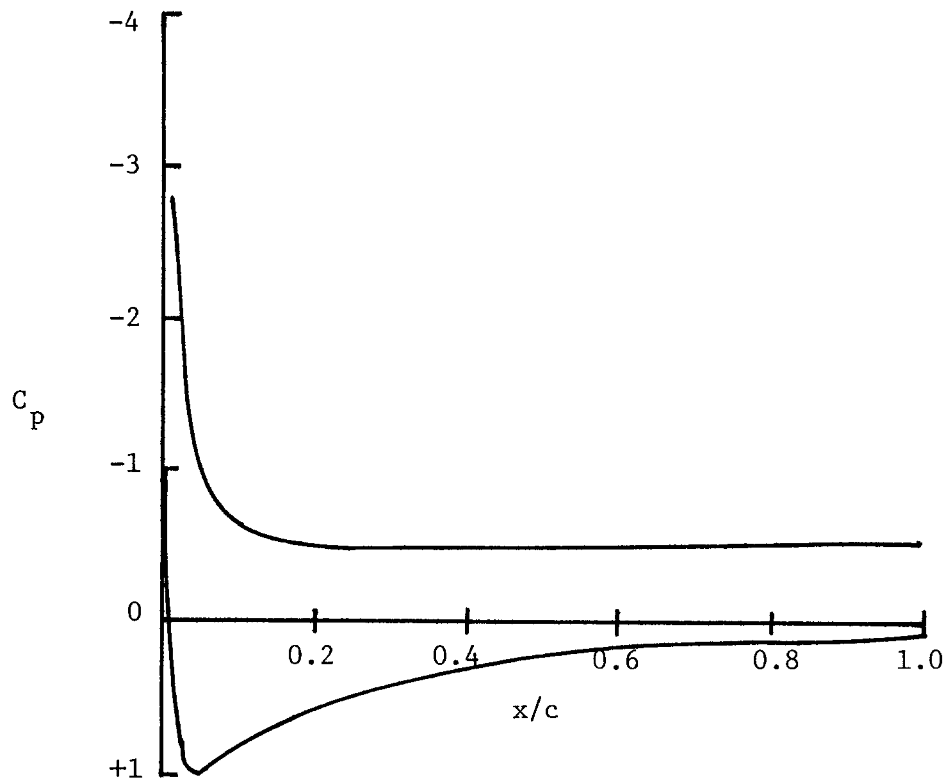

Figure 3.3.7 Calculated Pressure Distribution on a NACA 0015 Airfoil at 24° Angle of Attack and Re = 655,000

an incomplete and inaccurate modeling of the viscid/inviscid interactions in the immediate vicinity of the separation point. In DYNA2, the separation process is represented by a surface of potential discontinuity emanating from the boundary layer separation point. This wake surface influences the pressure distribution and, hence, has a feedback effect on the location of the boundary layer separation point. Therefore, the precise manner with which the wake surface is generated has a dramatic effect on the boundary layer calculations and the airload predictions as a whole. Additional development of DYNA2 in this area is needed.

Figure 3.3.8 illustrates a calculated wake geometry behind an airfoil with boundary layer separation. The geometry is qualitatively as would be expected.

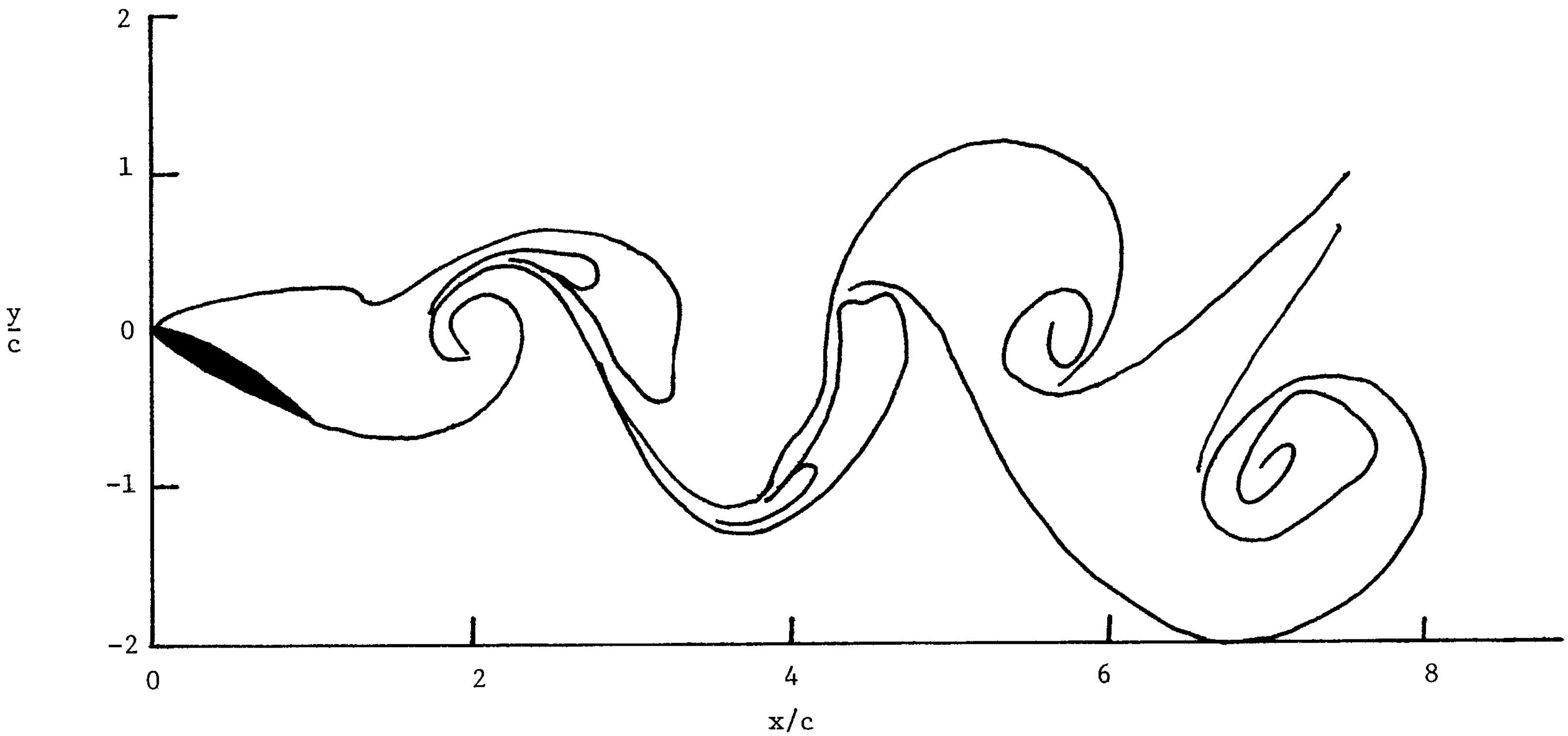

Figure 3.3.8 Computed Wake Geometry Behind a NACA 0015 Airfoil at an Angle of Attach Equal to 30°

4. DYNAMIC STALL EXPERIMENT

4.1 Objectives

The original motivation for pursuing an experimental investigation in parallel with the analytical study was to provide a means of verifying the model DYNA2 which is described in the previous sections. Unfortunately the present status of DYNA2 does not allow direct comparison since DYNA2 has not progressed to the point where the Darrieus flight path can be simulated. Eventually, however, DYNA2 will yield predictions of Darrieus turbine aerodynamic characteristics for which there are currently no available experimental counterparts. While it is true that there is a large amount of available experimental data for oscillating airfoils, there is also a need for unsteady aerodynamic data specific to Darrieus turbines. The experimental work described in the following sections represents a significant beginning effort aimed at alleviating that need.

The experiments which were conducted were designed to determine the characteristics of the unsteady blade loadings and dynamic stall phenomena as they occur on Darrieus turbines. Similar experiments on airfoils oscillating in pitch have revealed that the oscillation amplitude and reduced frequency of the oscillations are key parameters in determining the significance of the unsteady aerodynamic effects (see Martin, et al., 1974 and Cebecci and Smith, 1974). In the present work the tip-to-wind speed ratio is indicative of the oscillation amplitude and will be varied over a limited range. The chord to radius ratio is indicative of the oscillation frequency and will be fixed a a value of C/R = 0.25.

4.2 General Test Setup

The general test setup is described by Strickland (1980) in detail and will be described only briefly herein. In general, a straight-one-bladed rotor with a NACA 0015 airfoil was built and operated in a water tow tank with a depth of 1.25 meters, a width of 5 meters, and a length of 10 meters. Some testing was also done using a SANDIA 0015/47 airfoil. The rotor blades extended to within 15 centimeters of the tank bottom. This simple rotor appeared to be adequate for validating the major features of the analytical model. The use of water as a working fluid greatly facilitates the ability to make relatively low frequency measurements while working at appropriate blade Reynolds numbers. In addition, blade forces and pressures are more easily measured. An airfoil chord length of 15.24 cm and a rotor tip speed of 45.7 cm/sec were chosen to yield a blade Reynolds number of 67,000. Three towing speeds of 18.3 cm/sec, 9.1 cm/sec, and 6.1 cm/sec were chosen to yield tip-to-wind speed ratios of 2.5, 5.0, and 7.5, respectively. The rotor diameter was chosen to be 1.22 meters, thus giving a chord to radius value (C/R) of 0.25. Blade attachment was at mid chord in all cases.

Data were acquired using the Mechanical Engineering Department HP9835A desktop computer coupled to a multichannel HP6940B analog to digital converter and a HP7225A plotter. The system is capable of acquiring analog signals from an experiment at rates in excess of 1 KHz, which was quite adequate in light of the rotor rotational speed of 0.12Hz. The synchronization of the rotor position for various runs was extremely important. The rotor has a transducer (Waters Mfg. Analyzer APT 55) mounted on the main shaft, which allowed the rotor angular position to be monitored and recorded along with whatever other parameter was being measured.

Calibration and input data for each run were stored on magnetic tape cartridges which are compatible with the HP9835A. Each cartridge is capable of storing 256 K Bytes of information or about 128 K data points on 42 files.

4.3 Pressure Measurements

Pressure measurements were made on both sides of the NACA 0015 airfoil at five locations. The pressure ports were located at x/c values of 0.017, 0.042, 0.100, 0.360, and 0.810 at a uniform depth of about 30 cm below the water surface. The pressure ports were connected to diaphram pressure transducers (Validyne DP45-16) via copper tubing which was inserted through the hollow cores of the blade. The diaphram pressure transducers were connected to a Validyne demodulator unit (CD 18) which converted the pressure signal into an analog voltage suitable for introduction into the HP data acquisition system. A schematic of the arrangement is shown in Fig. 4.3.1.

The pressure measurements were made on one side of the airfoil and then the other. The inner side denotes the surface closest to the axis of rotation while the outer side denotes the side farthest from the axis of rotation. At least five repetitive runs were made to check the repeatability of the data.

Typical pressure data are shown in Fig. 4.3.2 for the inner and outer surfaces at $x/c = 0.10$ as a function of rotor position. Multiples of 360 degrees correspond to the nose of the foil pointing directly into the flow. These data are the average of five runs and differ very little from each individual run.

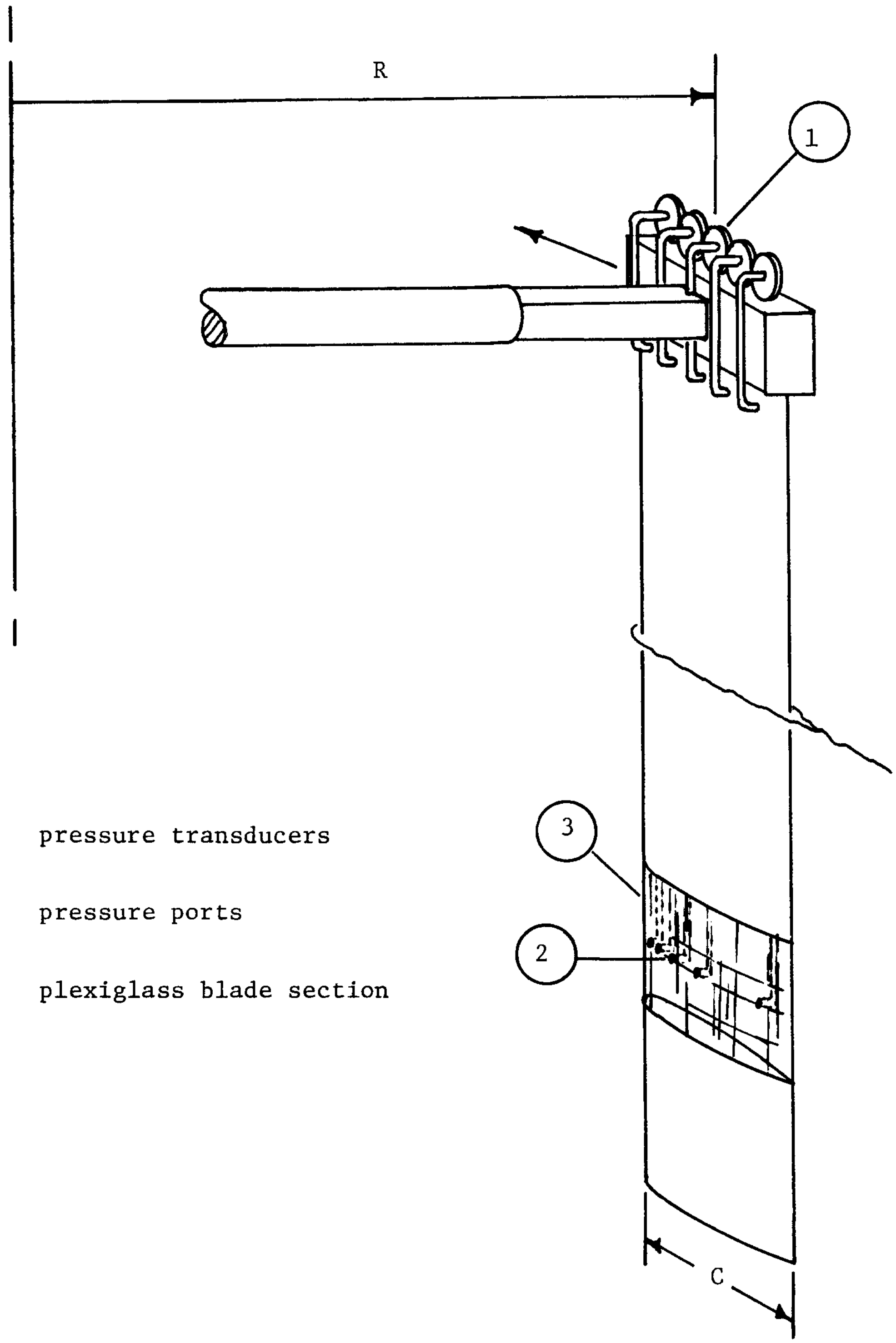

1 pressure transducers

2 pressure ports

3 plexiglass blade section

Fig. 4.3.1 Arrangement of Pressure Taps and Transducers

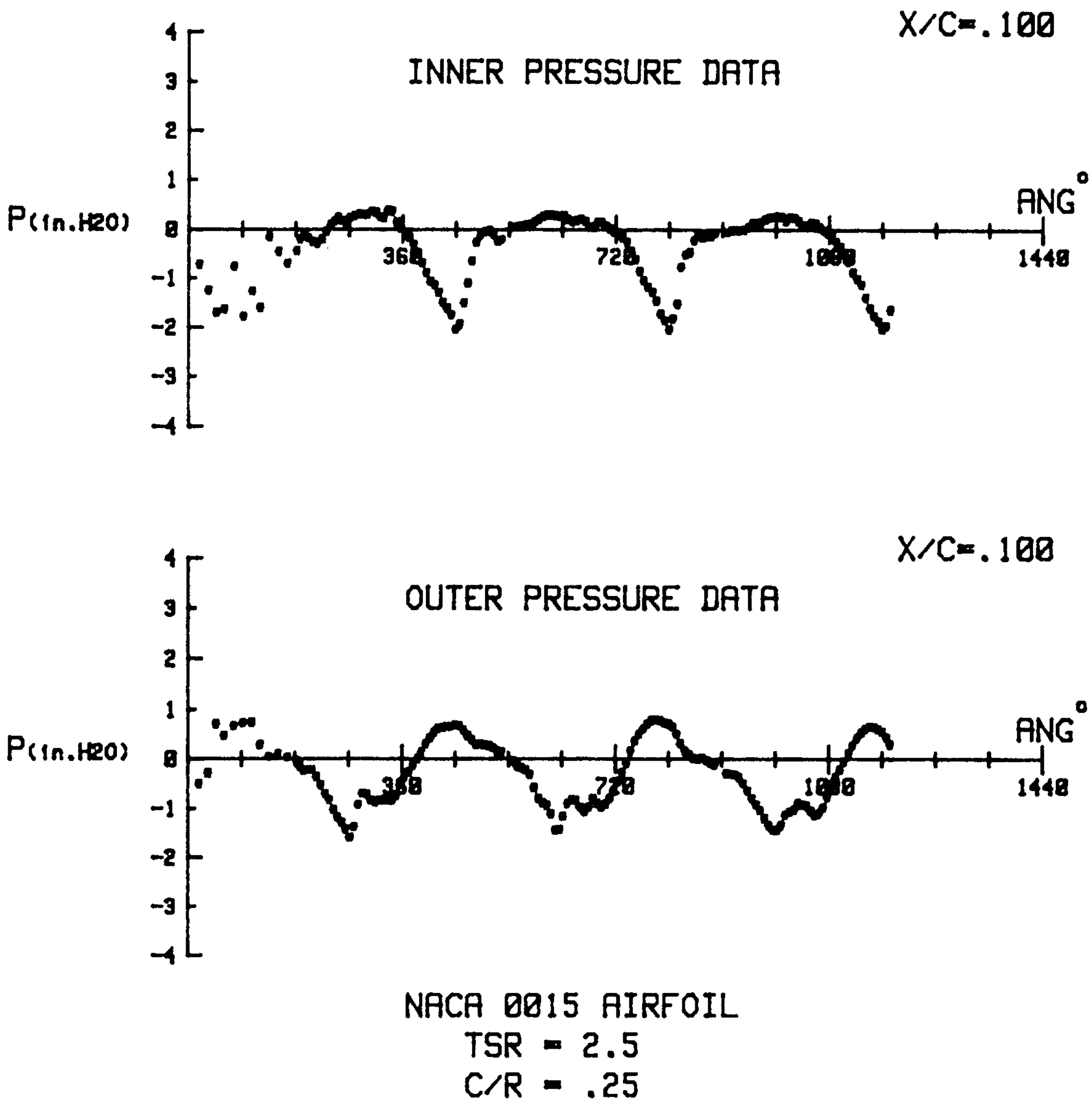

Fig. 4.3.2 Typical Pressure Data as a Function of Rotor Blade Azimuthal Angle

Typical pressure coefficient distributions for the airfoil at two different rotor angles are shown plotted in Fig. 4.3.3. The pressure coefficient in this case is defined by

$$C_p = \frac{P-P_\infty}{1/2\rho U_b^2}$$

where (4.3.1)

$$\vec{U}_b = \vec{U}_T + \vec{U}_\infty$$

Here the velocities U_T and U_∞ are the blade tangential speed and the carriage speed (wind speed far from the rotor), respectively. The pressure P_∞ is the static pressure at the depth below the surface corresponding to the pressure taps. A set of Cp curves taken during the second revolution are given in Appendix E for tip-to-wind speed ratios of 2.5, 5.1, and 7.6.

The normal and tangential forces can be obtained by integrating the Cp curves. Since only ten data points are available, the results may contain a reasonable amount of error. The integration was carried out using a second order polynomial fit to three data points in the subregion of integration. The results for the normal and tangential forces are given in Fig. 4.3.4 and Fig. 4.3.5 respectively. The nondimensional forces F_n^+ and F_t^+ are defined by

$$F_n^+ = \frac{F_n'}{1/2\rho C U_\infty^2}$$

(4.3.2)

$$F_t^+ = \frac{F_t'}{1/2\rho C U_\infty^2}$$

where F_n' and F_t' are the normal and tangential forces per unit blade length.

4.4 Strain Gage Measurements

Measurements of normal and tangential forces using strain gage instrumentation were performed for three tip-to-windspeed ratios of 2.5, 5.1, and 7.6. Five repetitive runs were made to determine the repeatability of the data. Tests were performed on both the NACA 0015 and the Sandia 0015/47.

The experimental arrangement for obtaining strain gauge data is shown in Fig. 4.4.1. As indicated in Fig. 4.4.1 the two forces were measured using strain gages located on a support mounted at the mid chord. Each bridge was arranged so that it was only sensitive to the desired force.

The instrumentation consisted of eight 350 ohm strain gages making up the two Wheatstone bridge configurations, a 15 vdc Calex power supply, a Calex model 176 amplifier, and a Krohnite model 3343 low pass filter. A 15 vdc signal was applied across the bridge. As the bridge was strained the voltage caused by the unbalanced bridge was measured. This output voltage was amplified approximately 1000 times to increase the signal level into the desired voltage range. The output signal from the bridge was passed through a filter to low pass the signal below a cutoff frequency of 0.6 Hz. This was necessary in order to eliminate extraneous mechanical noise at about 2 Hz. Finally, the signal was introduced into the data acquisition system.

The output voltages from the strain gage bridges E_1 and E_2 are related to the blade forces by

$$\begin{aligned} F_n &= C_1 E_1 \\ F_t &= C_2 E_2 \end{aligned} \qquad 4.4.1$$

where C_1 and C_2 are calibration constants. It should be noted that E_1 includes the effect of the centrifugal force given by

$$F_c = mR\omega^2 \qquad 4.4.2$$

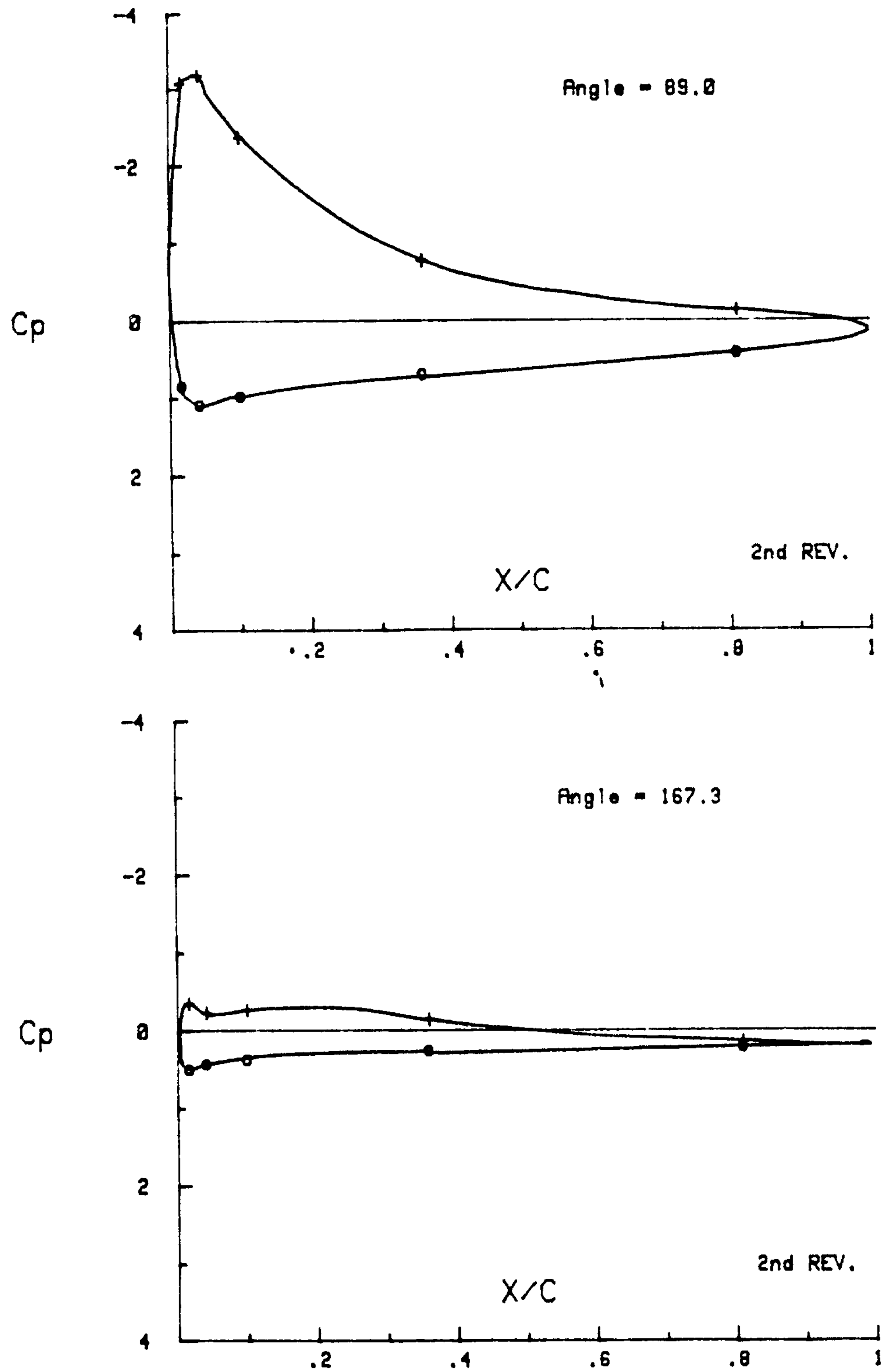

Fig. 4.3.3 Typical Pressure Coefficients
(TSR = 2.5, C/R = 0.25, NB = 1, NACA0015,
Outer Surface 0, Inner Surface +)

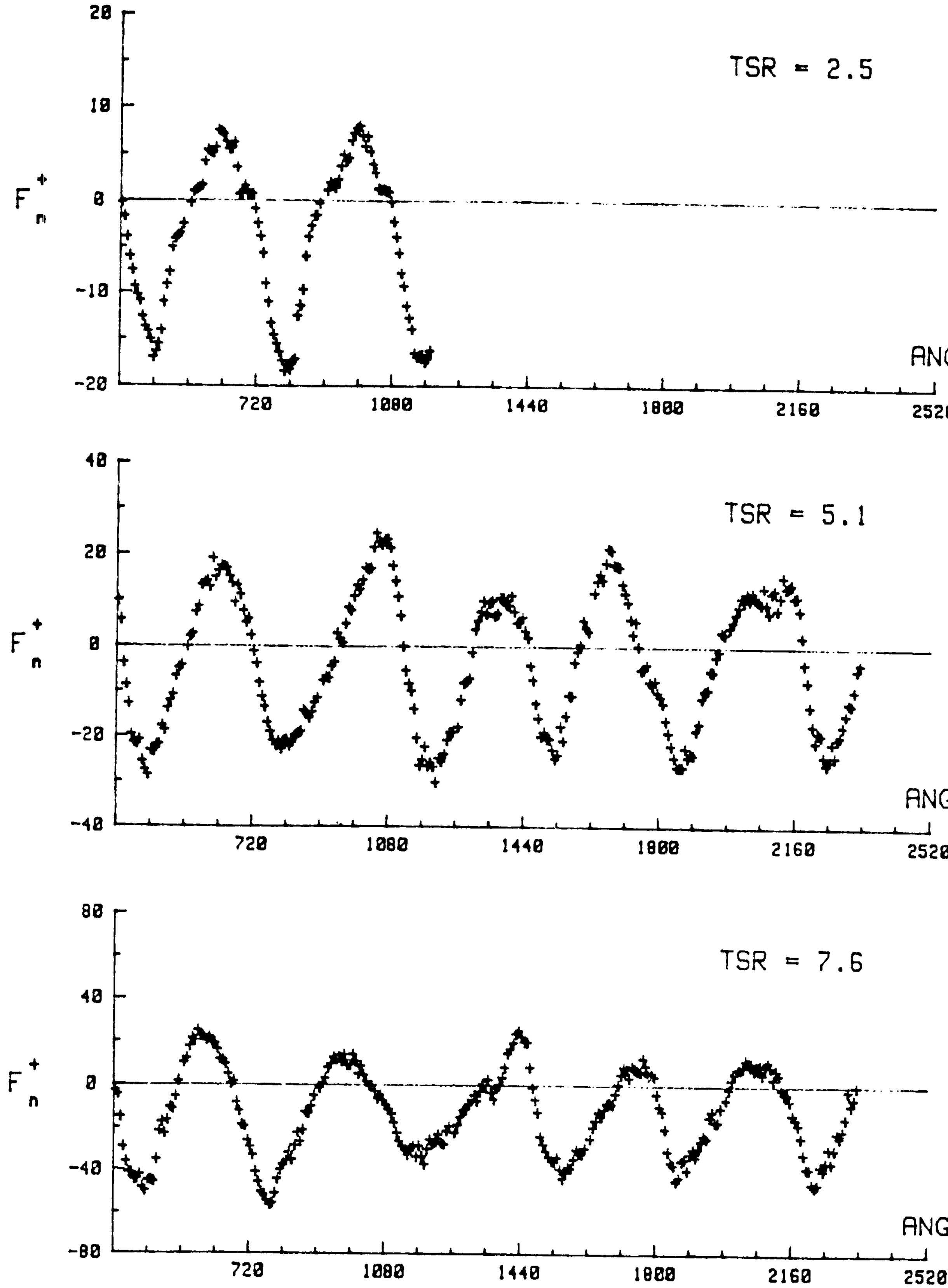

Fig. 4.3.4 Normal Pressure Force Data for NACA 0015 Rotor

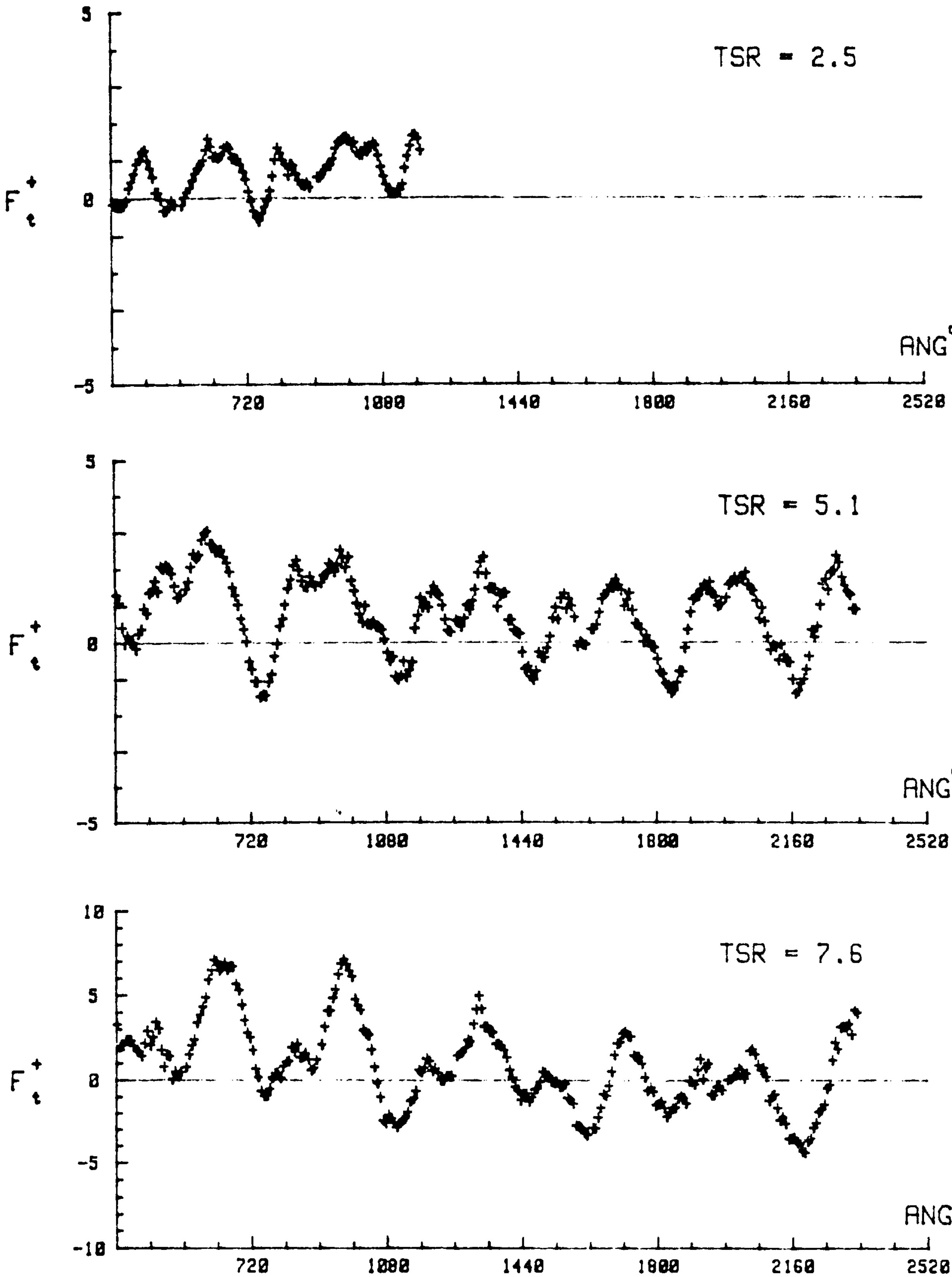

Fig. 4.3.5 Tangential Pressure Force Data for NACA 0015 Rotor

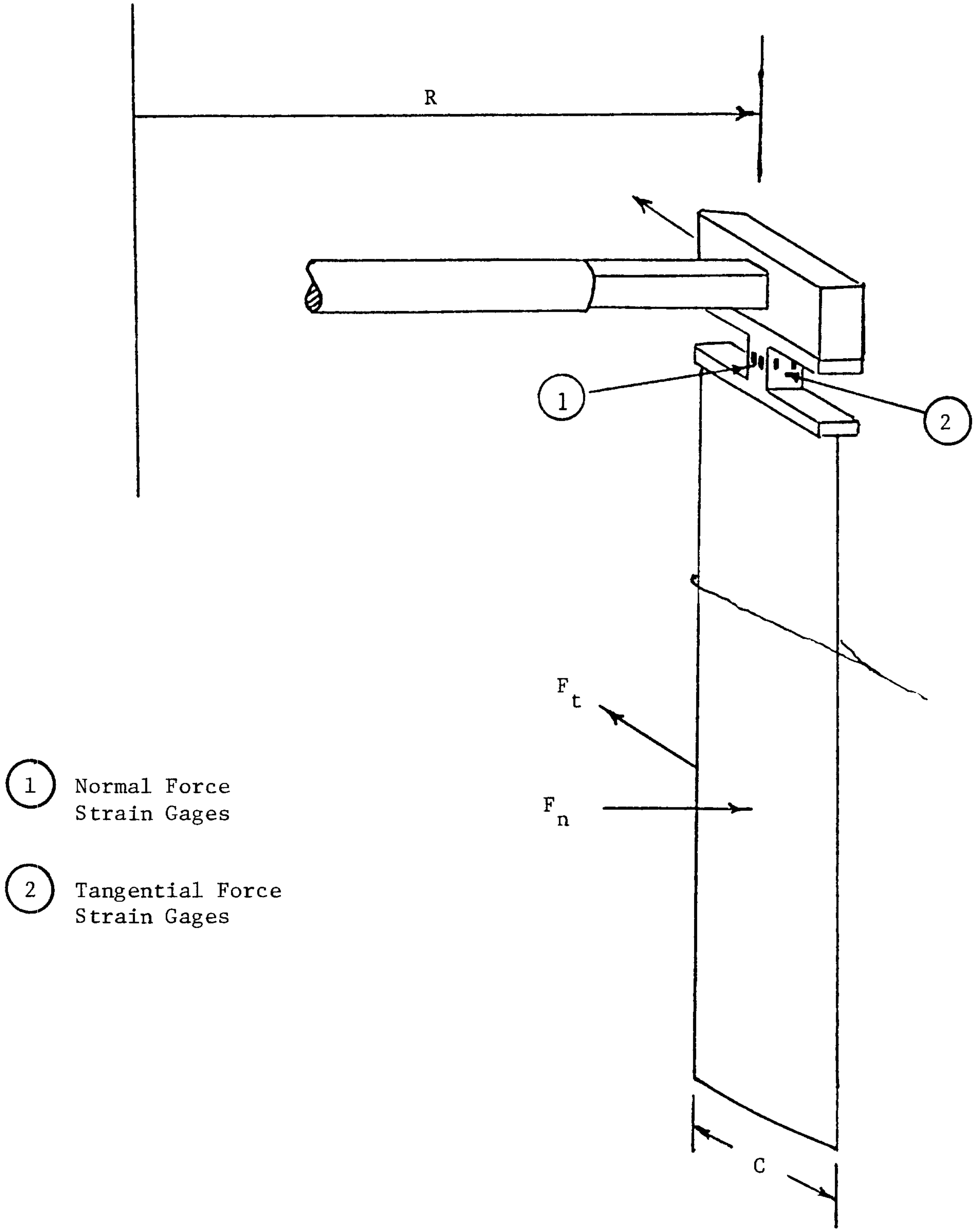

Fig. 4.4.1 Strain Gage Instrumentation

where m is the mass of the blade. While this effect is relatively small it was nevertheless subtracted from the equation for F_n. All cases were run at the same angular speed (tip speed) and thus F_c was constant for all cases. Additionally, the strain gage data were corrected for finite aspect ratio effects; i.e. induced drag and lift. The effective aspect ratio of the blade was approximately 10.5 and therefore these corrections tend to be small. Details of this correction are given by Graham (1982).

Strain gauge data for normal and tangential forces on the NACA 0015 rotor are given in Figures 4.4.2 and 4.4.3. Data for the Sandia 0015/47 rotor are shown superimposed on the NACA 0015 data in Figures 4.4.4 and 4.4.5.

4.5 Discussion of Results

The experimental results which were obtained as a part of this study cannot be compared to results from the DYNA2 model at the present time. Some comparisons between the VDART2 model by Strickland (1981(a) and 1981(b)) can be made along with comparisons between the integrated pressure force data and the strain gage data. In addition, the instantaneous pressure data can be used to yield some information on the progression of stall on the airfoil.

4.5.1 Blade Forces

Typical non-dimensional blade forces are shown in Figures 4.5.1, 4.5.2 and 4.5.3. These forces are defined by Equations 4.3.2. A positive normal force acts radially outward while a positive tangential force acts in the direction of motion of the airfoil. Blade forces obtained from integrated pressure measurements, strain gage measurements, and analysis are plotted in these figures.

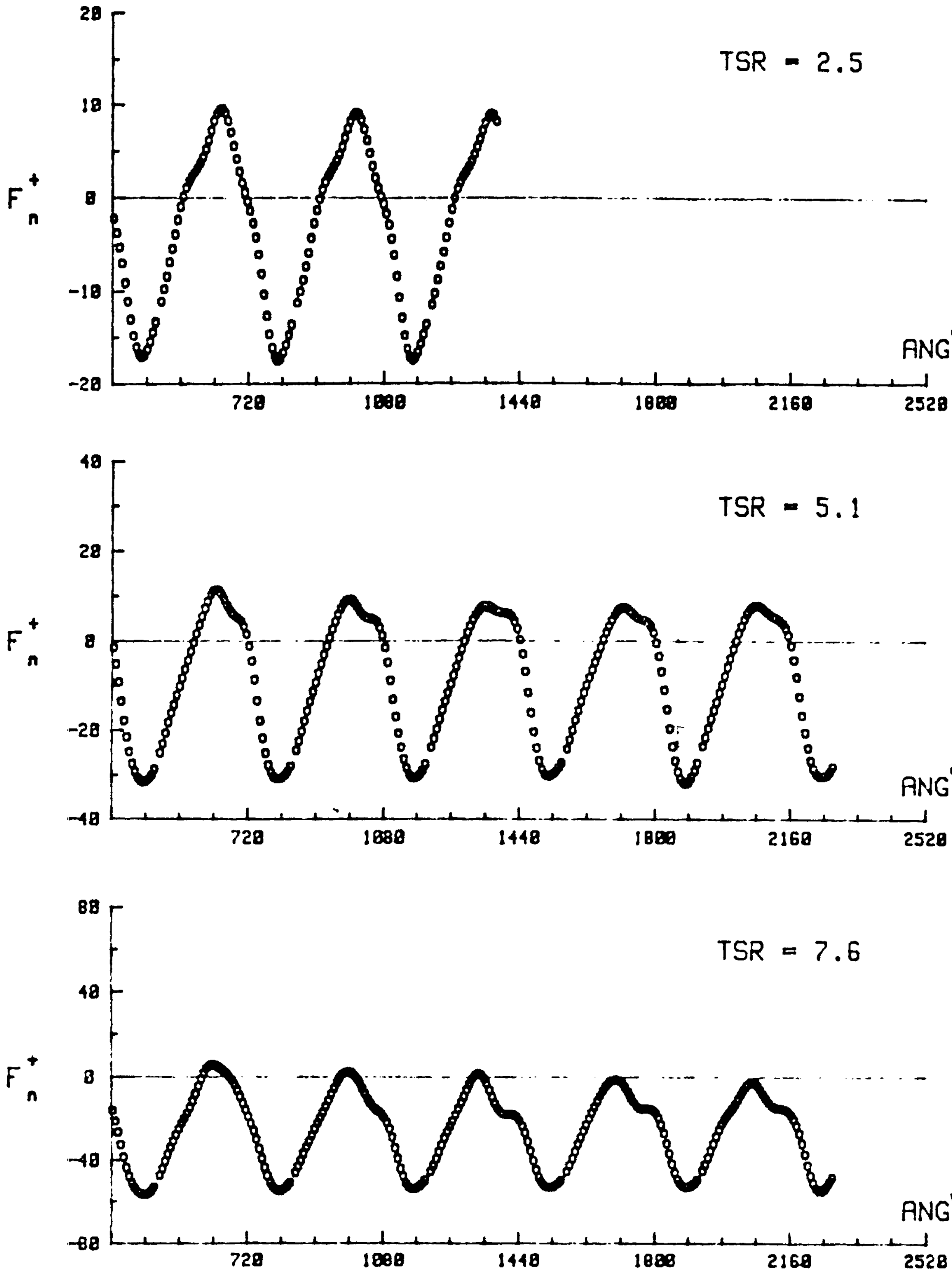

Fig. 4.4.2 Normal Strain Gage Force Data from NACA 0015 Rotor

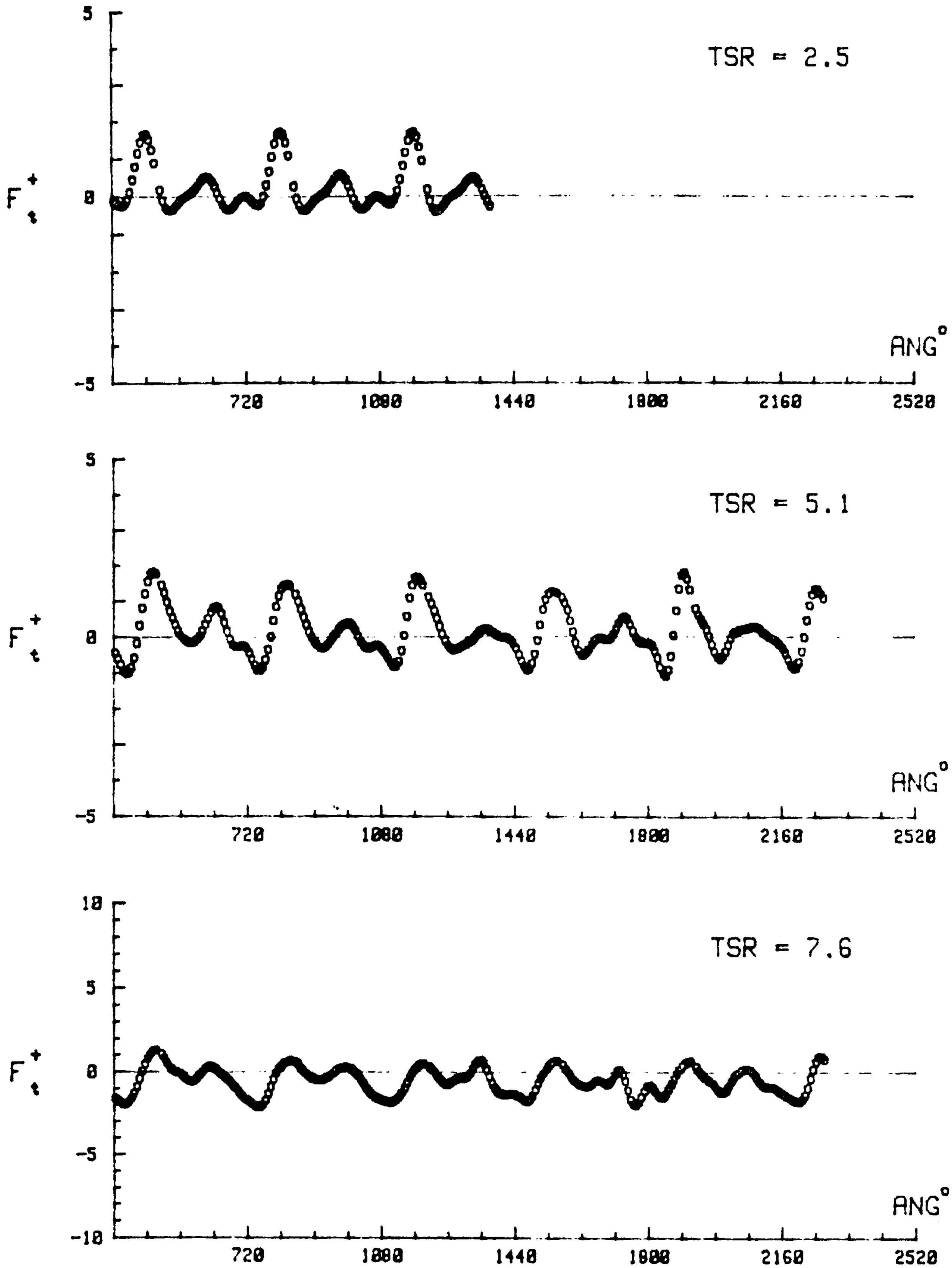

Fig. 4.4.3 Tangential Strain Gage Data from NACA 0015 Rotor

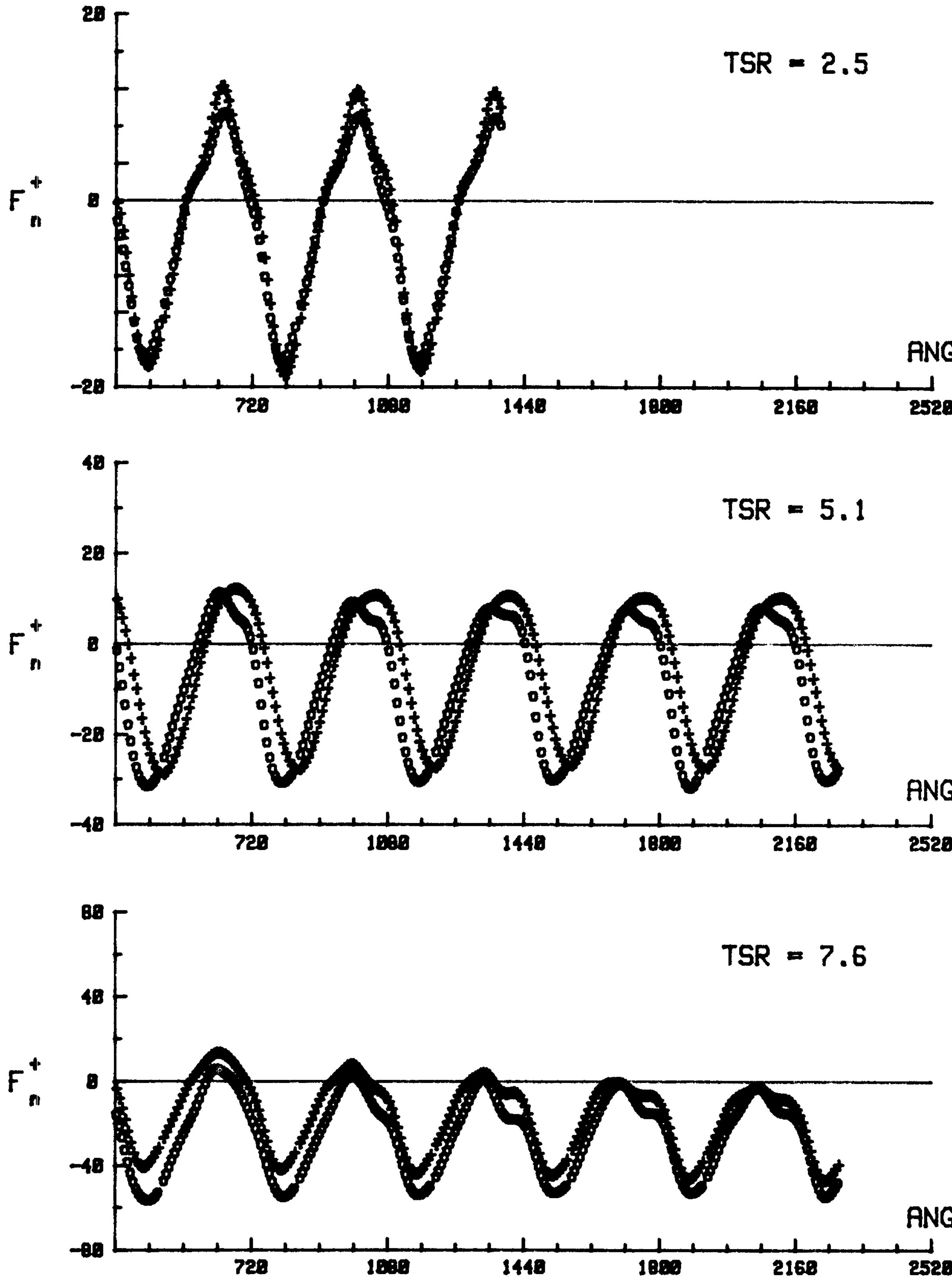

Fig. 4.4.4 NACA 0015 and SANDIA 0015/47 Strain Gage Normal Force Data

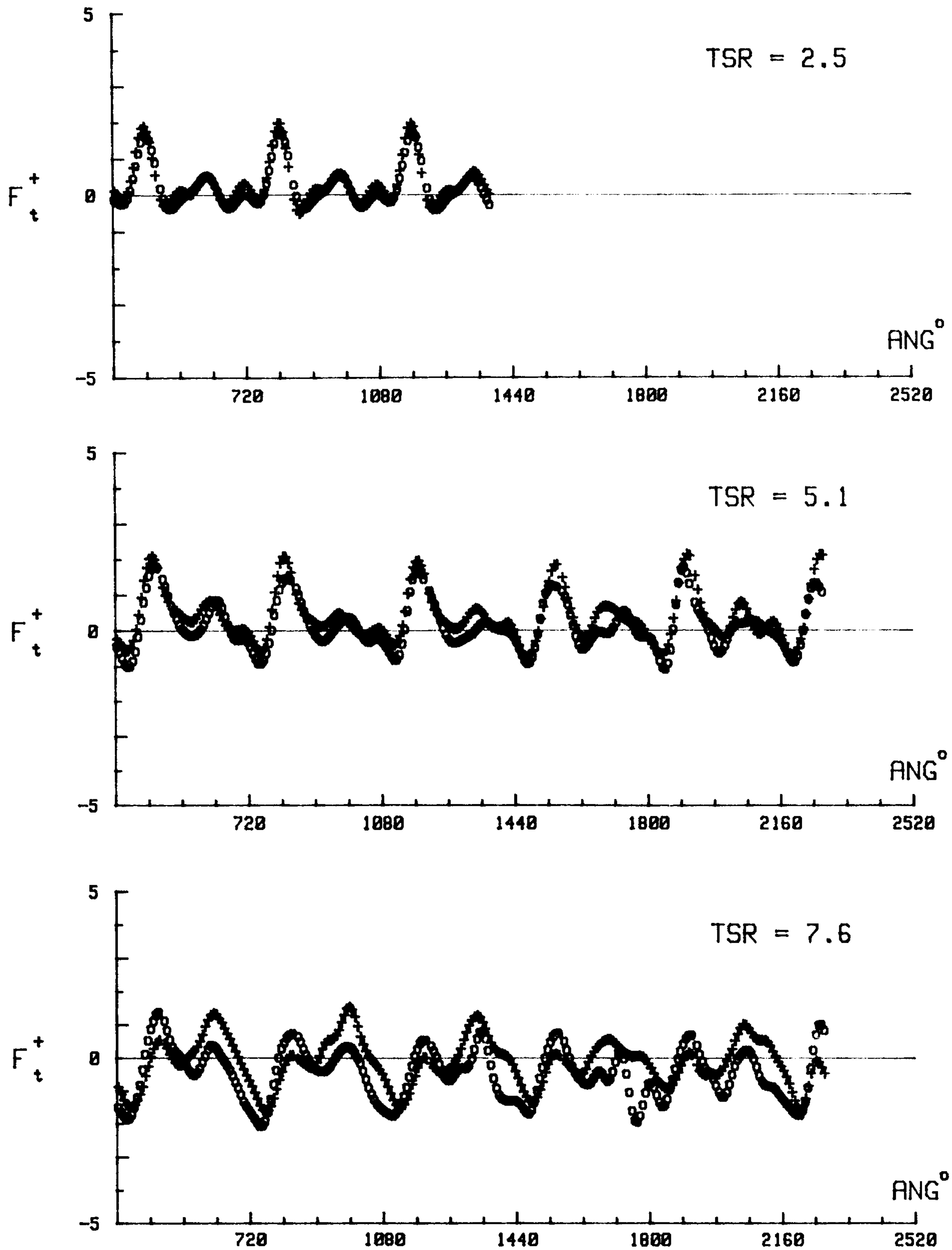

Fig. 4.4.5 NACA 0015 and SANDIA 0015/47 Strain Gage Tangential Force Data

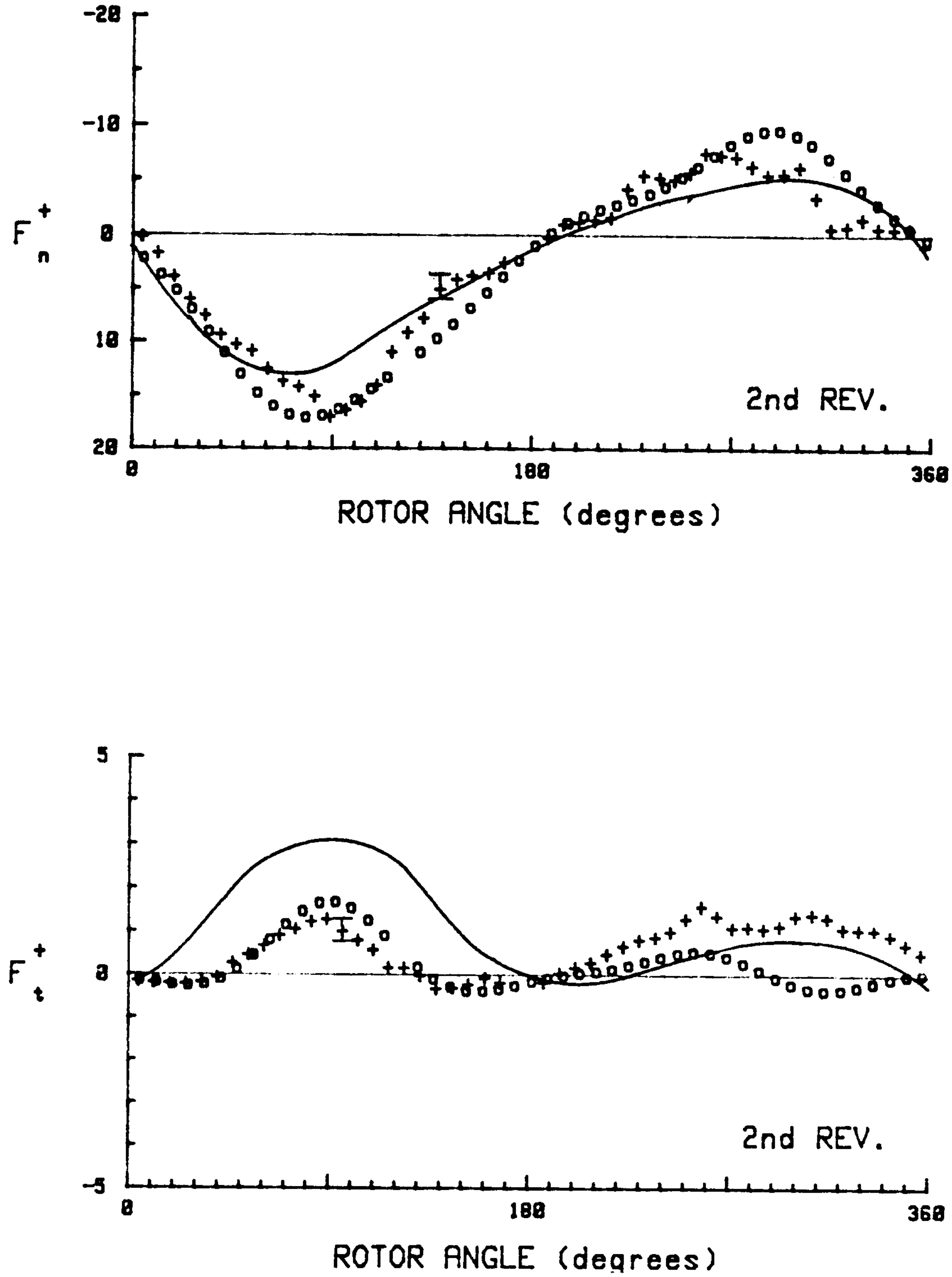

Fig. 4.5.1 Non-Dimensional Blade Forces
(TSR = 2.5, C/R = 0.25, NB = 1, Pressure Data +,
Strain Gage 0, VDART2 -)

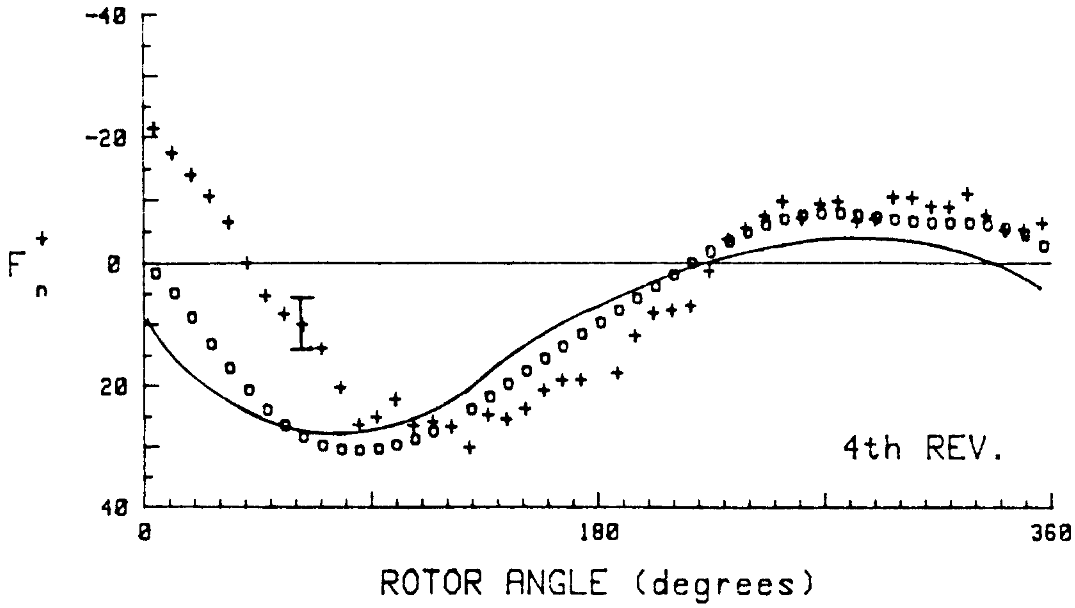

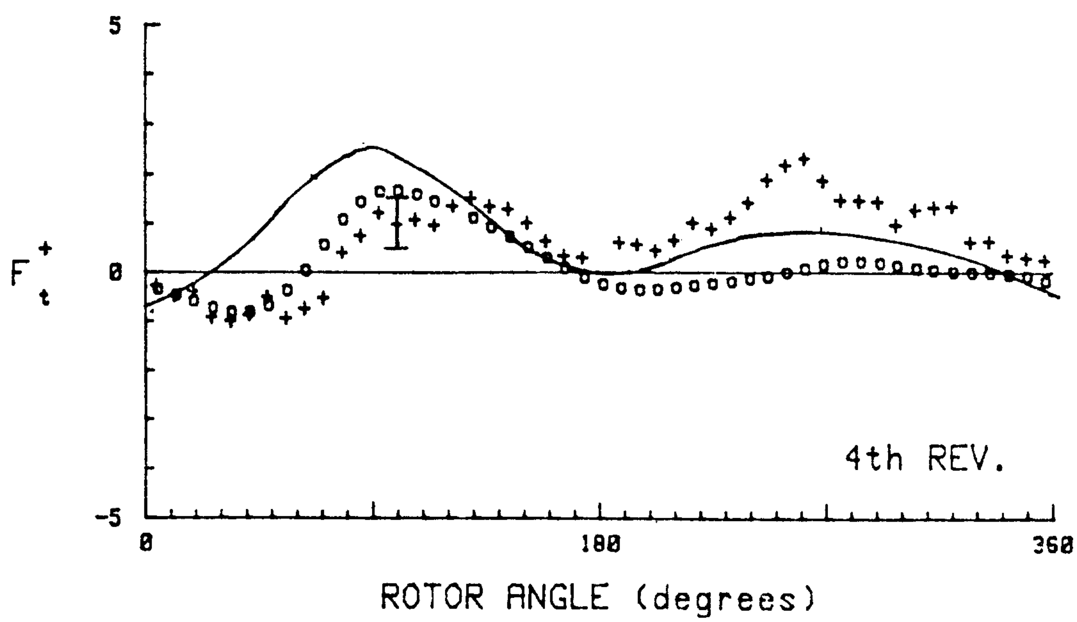

Fig. 4.5.2 Non-Dimensional Blade Forces
(TSR = 5.1, C/R = 0.25, NB = 1, Pressure Data +,
Strain Gage 0, VDART2 -)

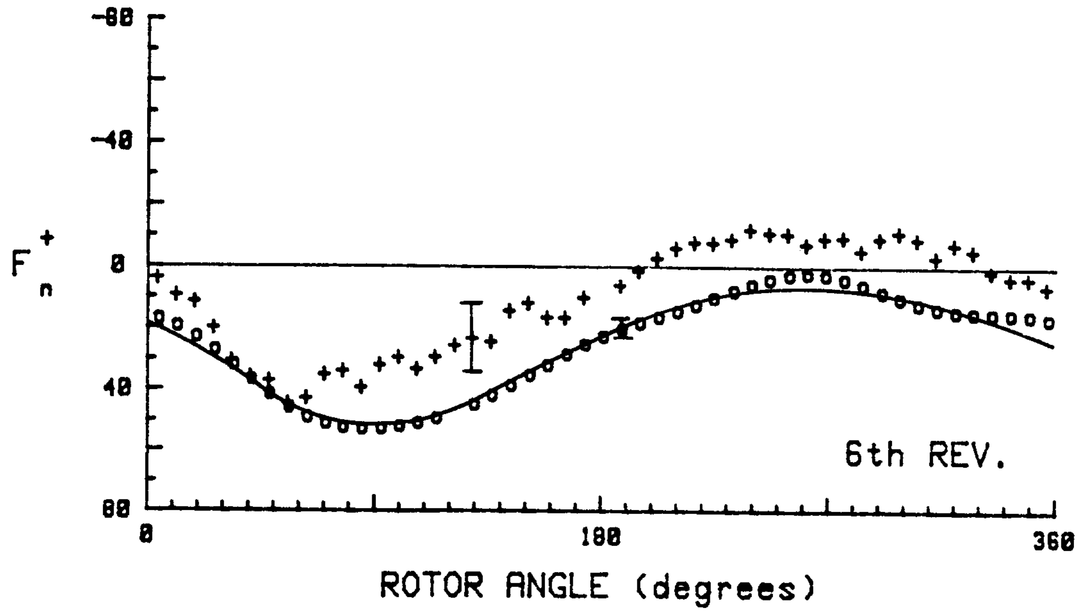

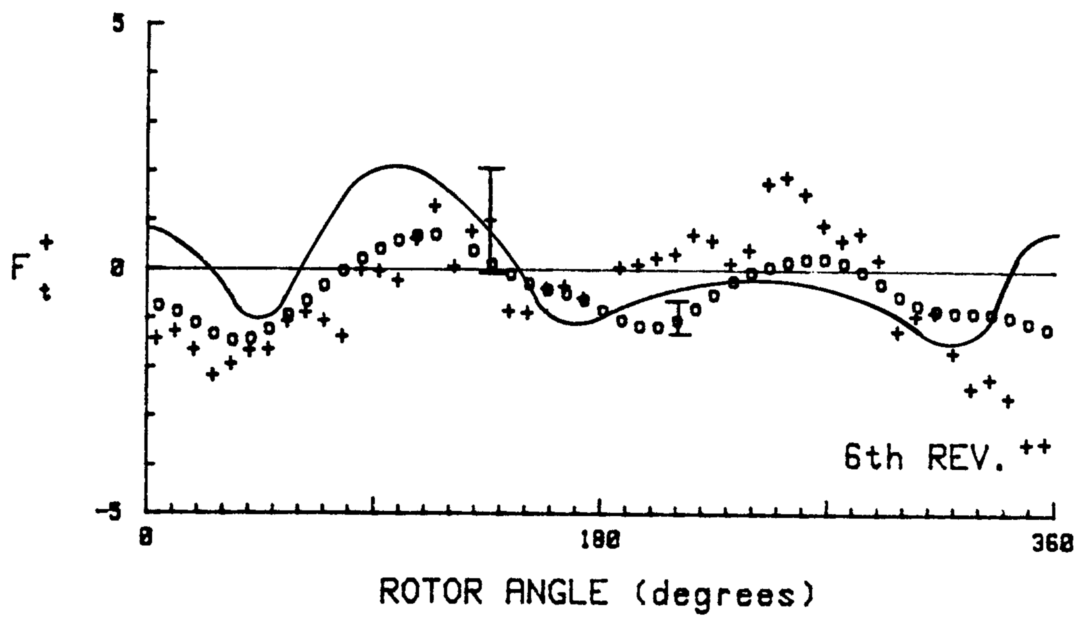

Fig. 4.5.3 Non-Dimensional Blade Forces
(TSR = 7.6, C/R = 0.25, NB = 1, Pressure Data +,
Strain Gage 0, VDART2 -)

Fair agreement exists for the normal force (F_n^+) results between the two experimental sets of data and the VDART2 analysis. The agreement between the strain gage data and the analysis is typical of that noted previously by Strickland (1981(a)) for two bladed rotors with C/R = 0.15.

The tangential forces (F_t^+) are an order of magnitude smaller than the normal forces and thus tend to be more difficult to measure. The agreement between the integrated pressure measurements and the strain gage measurements is seen to be reasonably good in the upstream region between 0° and 180°. The integrated pressure measurements typically tend to produce much larger values of F_t^+ than do the strain gage measurements in the region of 180° to 360°. The reason for this is presently not well understood. The VDART2 analytical predictions when compared with the strain gage data are again typical of those noted by Strickland (1981(a)). The peak value of F_t^+ predicted in the upstream region for a tip-to-windspeed ratio of 2.5 tends to be high in comparison to the strain gage measurements. This discrepancy can be traced to an inadequate dynamic stall model in the VDART2 analysis.

Several things can be said with regard to the accuracy of the various force data. The strain gage measurements appear to yield the best results in that the data are smooth and vary in a continuous fashion from one cycle to the next. This is readily seen, for instance, by comparing Figures 4.3.4 and 4.3.5 with 4.4.2 abd 4.4.3. The strain gage data are also quantitatively similar to strain gage data taken previously by Strickland (1982(a)) for slightly different cases. The strain gage data are subject to error due to aspect ratio corrections which were only approximately made in the present work. In addition, some error may have been introduced due to minor tangential accelerations of the blade caused by play in the drive train. These sources of error are not considered in the indicated error bars. The integrated pressure data, on the other hand, is subject to errors associated with local static pressure variations due to small vertical displacements of the blade as it moves through the water. This change in reference pressure affects the normal force since the blade was run once in each direction through the tow tank to obtain pressures on both sides of the airfoil. The numerical integration procedure used as well as the number of pressure taps can also significantly affect the integrated pressure results. In the present work the number of pressure taps may not have been adequate. Another source of error which can be significant at high tip to windspeed ratios is blade toe-in or toe-out. A toe-in or out of 5 degrees will, for instance, change the magnitude of F_t by about 2.5 at a tip to windspeed ratio of 7.6.

In summary, the integrated pressure measurements do not yield sufficiently accurate tangential force data and should be improved by eliminating some of the sources of experimental error. The normal forces obtained from integrated pressure measurements are, on the other hand, of fair quality.

4.5.2 Pressure Data

In this section the pressure data are analyzed to extract information concerning the phenomenon of dynamic stall. The data indicate that dynamic stall occurs primarily at the lowest tip-to-windspeed ratio of 2.5 although some stall may occur at the tip-to-windspeed ratio of 5.1 The data shown in Figures 4.5.4-4.5.10 obtained at a tip-to-windspeed ratio of 2.5 during the second revolution of the NACA 0015 blade. The data presented in this section are the result of a single run to avoid any averaging of the pressure pulse moving across the airfoil. The non-dimensional pressure coefficient is defined by equation 4.3.1.

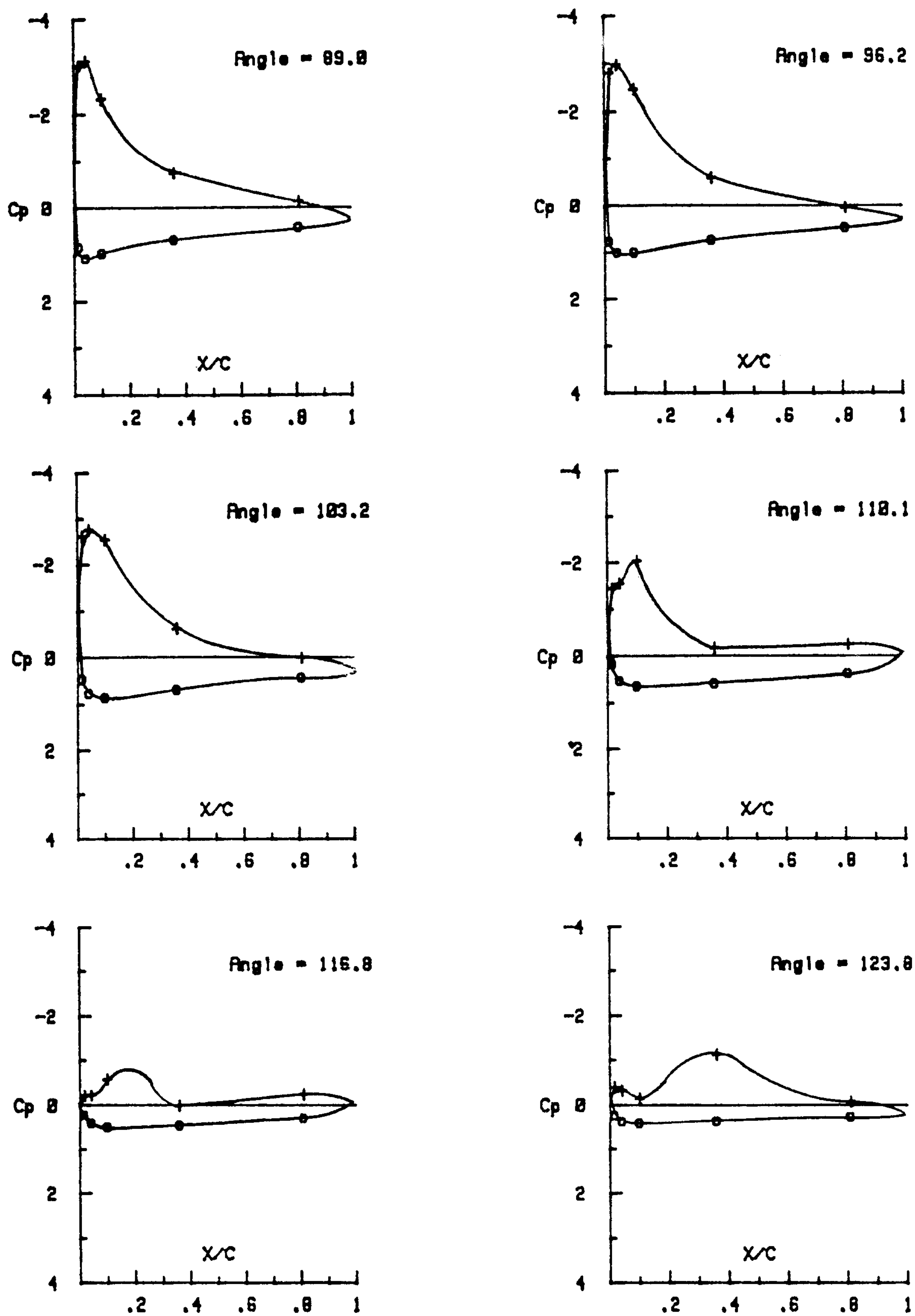

Fig. 4.5.4 Effect of Rotor Angle on Pressure Coefficient
(TSR = 2.5, C/R = 0.25, N = 1, Outer Surface 0,
Inner Surface +)

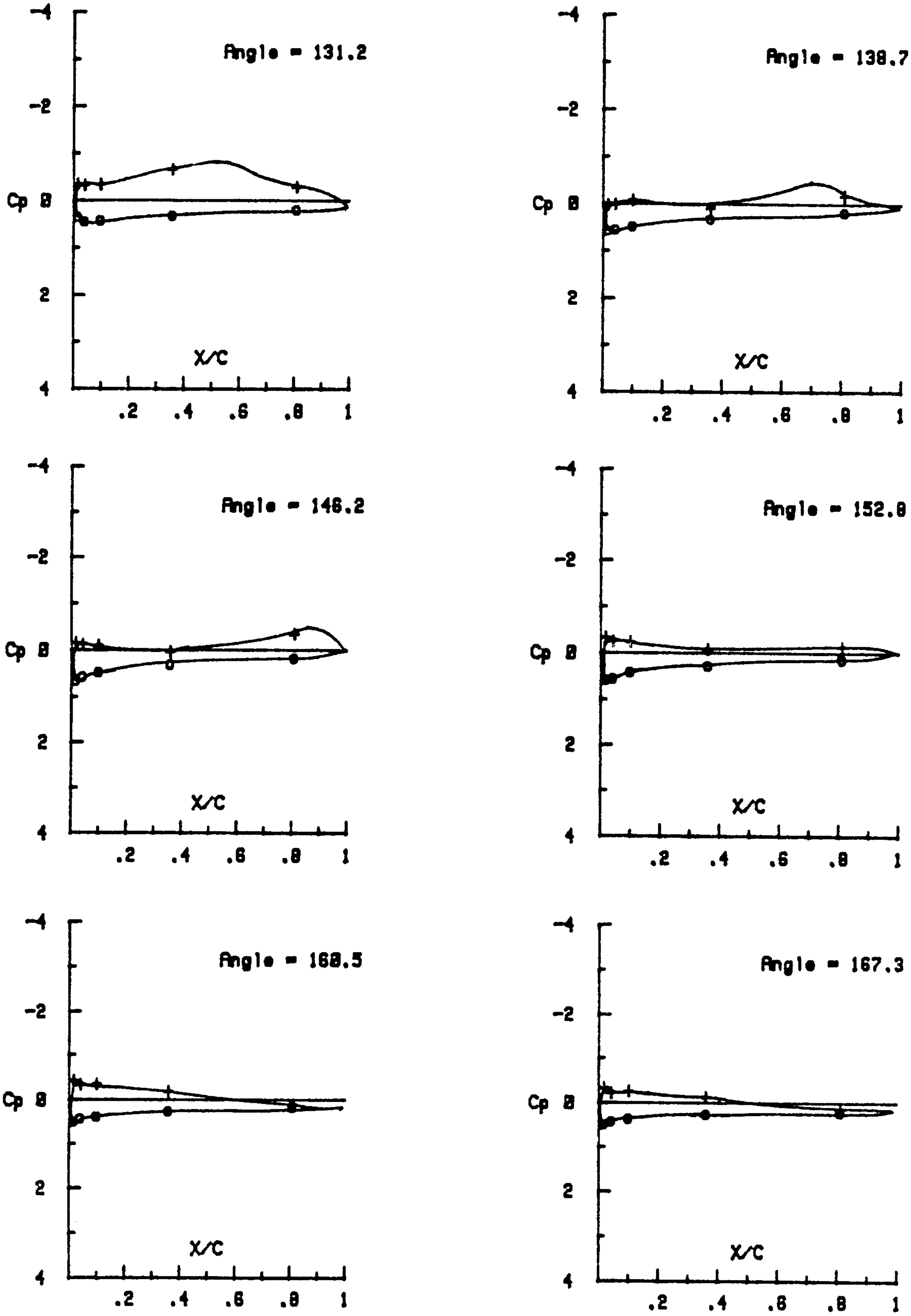

Fig. 4.5.5 Effect of Rotor Angle on Pressure Coefficient (TSR = 2.5, C/R = 0.25, N = 1, Outer Surface 0, Inner Surface +)

As seen in Figure 4.5.4, at a rotor angle of 110.1° there is a flattening of the C_p curve over the aft inner surface of the airfoil indicating separation. Simultaneously the suction peak begins to decrease in magnitude. At a rotor angle of 116.8° the angle of attack is approximately 23° and the airfoil appears to be fully stalled over the inner surface. In the vicinity of this rotor angle it is believed that a vortex is shed at the nose and begins moving along the surface of the airfoil. At a rotor angle of 123.8° this vortex appears to be passing through the vicinity of x/C = 0.36 and has significantly affected the pressure on the surface of the airfoil at this location. The airfoil remains in a stalled condition until a rotor angle of approximately 150°. At this point the flow reattached as indicated by the slight suction over the nose of the airfoil as shown in Figure 4.5.5 at a rotor angle of 152.8°.

Figures 4.5.6 and 4.5.7 show the Cp curves at rotor angular positions where the outer surface of the airfoil is experiencing stall. Separation of the flow over the aft portion of the airfoil appears to begin at a rotor angle of 264.9°. At a rotor angle of 271.9° the angle of attack is approximately -23° and the blade is fully stalled over the outer surface. As in the case of the inner surface stall described above, a vortex is shed at the nose of the airfoil and begins moving along the surface. The effect of this vortex on the pressure tap located at x/C - 0.36 may be seen at a rotor angle of 279.4°. The flow appears to have nearly reattached at a rotor angle of 300.4°. However, the C_p value at the x/C location of 0.81 indicates a strong pressure disturbance probably due to the vortex shed at the onset of stall.

Figures 4.5.8 - 4.5.10 show the effect of angle of attack on the pressure coefficient. The bars indicate suspected regions of stall. In

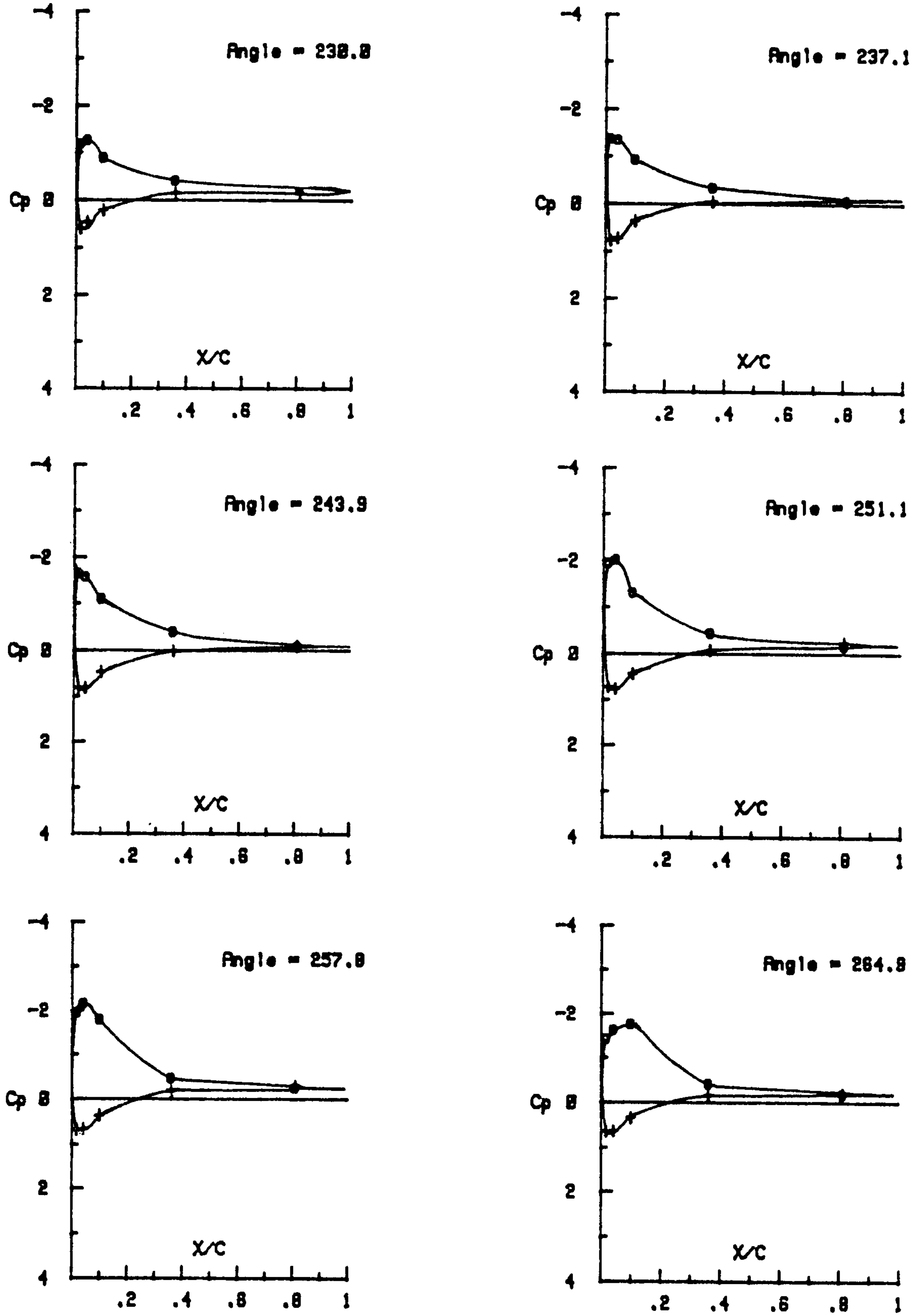

Fig. 4.5.6 Effect of Rotor Angle on Pressure Coefficient (TSR = 2.5, C/R = 0.25, N = 1, Outer Surface 0, Inner Surface +)

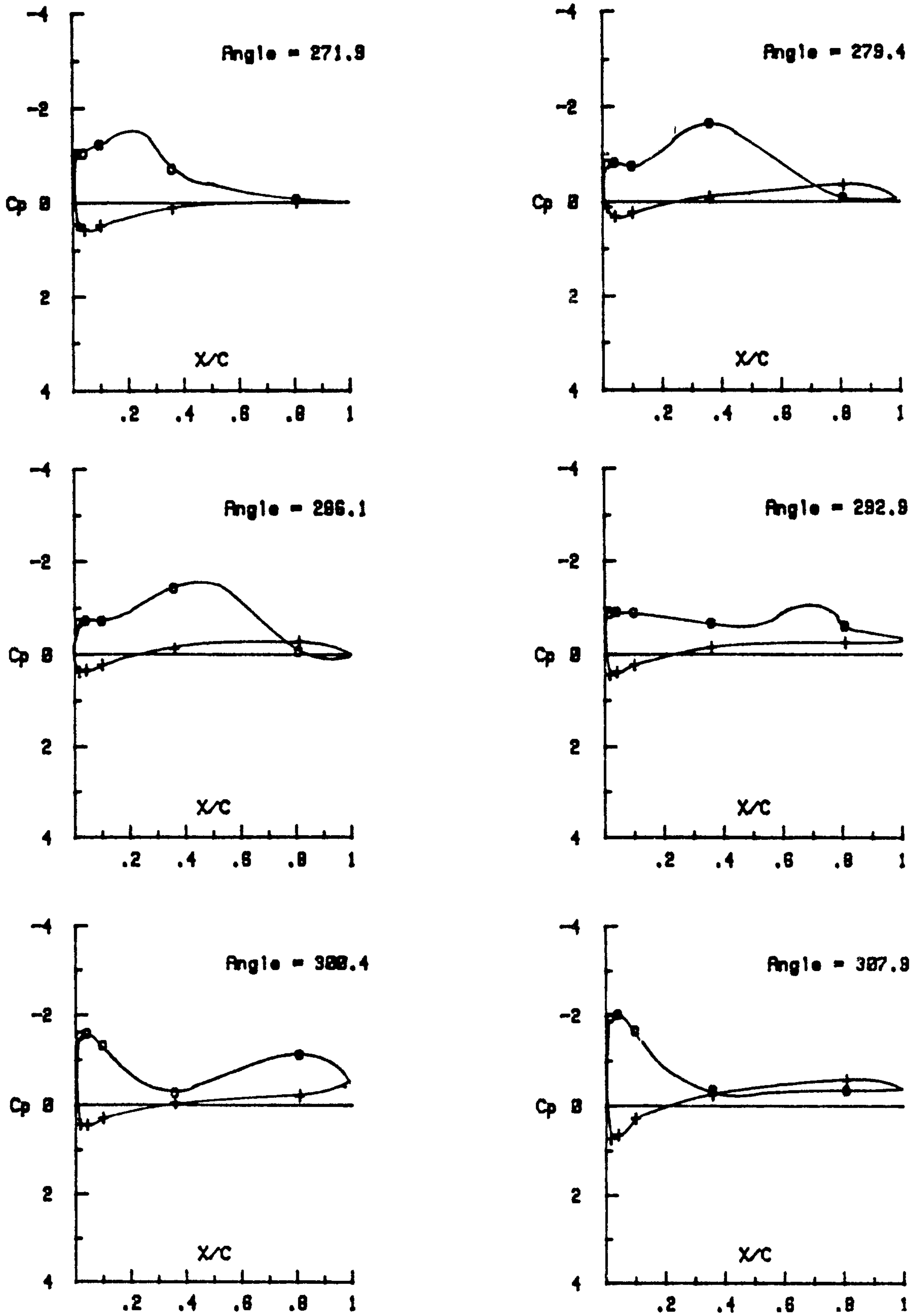

Fig. 4.5.7 Effect of Rotor Angle on Pressure Coefficient (TSR = 2.5, C/R = 0.25, N = 1, Outer Surface 0, Inner Surface +)

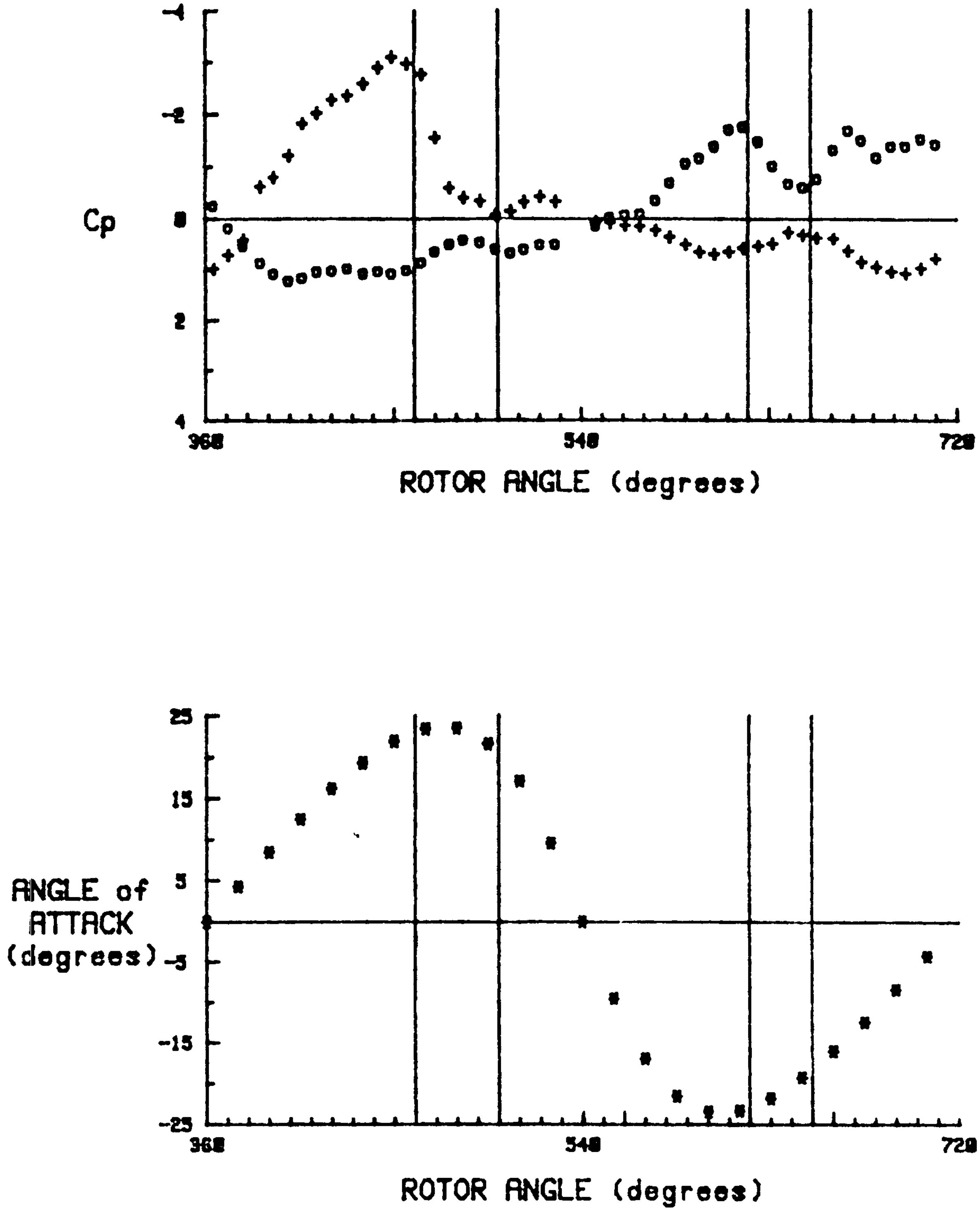

Fig. 4.5.8 Effect of Angle of Attack on the Pressure Coefficient for the Nose Region (0.017 < X/C < 0.1) (TSR = 2.5, C/R = 0.25, NB = 1, Outer Surface 0, Inner Surface +)

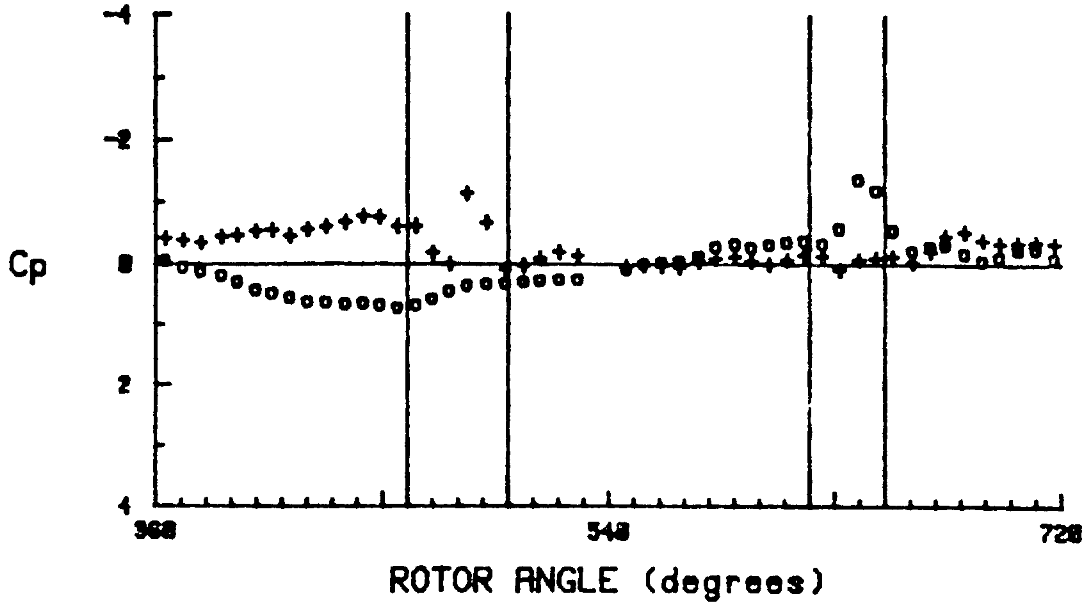

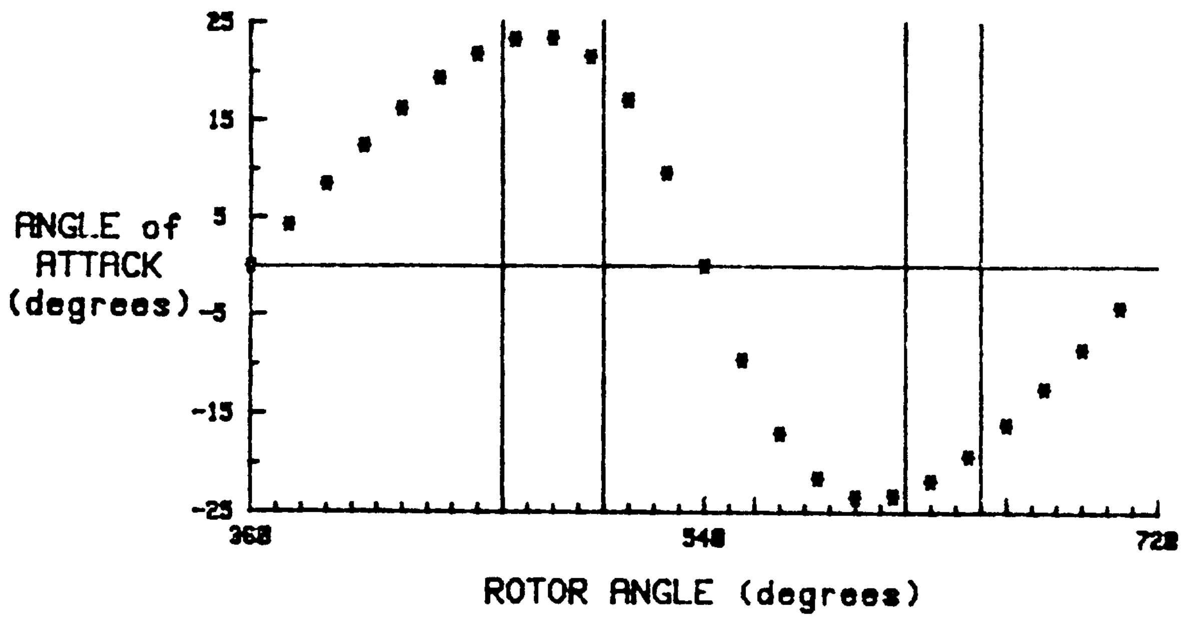

Fig. 4.5.9 Effect of Angle of Attack on the Pressure Coefficient for X/C = 0.36
(TSR = 2.5, C/R = 0.25, NB = 1, Outer Surface 0, Inner Surface +)

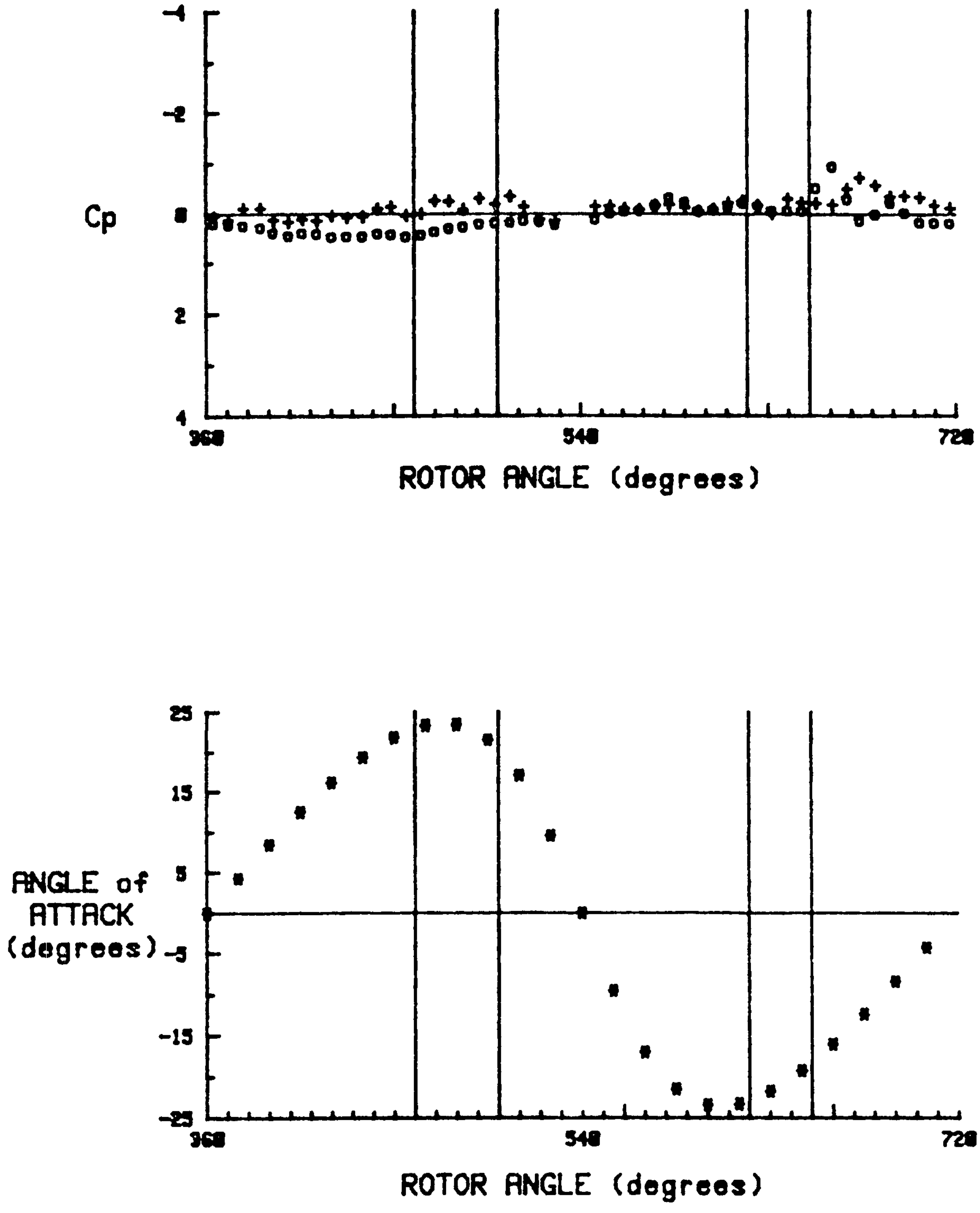

Fig. 4.5.10 Effect of Angle of Attack on the Pressure Coefficient for X/C = 0.81 (TSR = 2.5, C/R = 0.25, NB = 1, Outer Surface 0, Inner Surface +)

Figure 4.5.8 the maximum value of the pressure coefficient over the first three pressure taps is plotted versus the rotor position. The C_p values on the inner surface increase with increasing angle of attack until dynamic stall occurs. At this point, a dramatic loss of suction is observed until the flow reattaches. This effect is also observed in the region of outer surface stall. Figure 4.5.9 shows the effect of dynamic stall on the pressure coefficient at $x/C = 0.36$. The abrupt increase in the magnitude of the pressure coefficient in the regions of stall indicates passage of a vortex through this vicinity. This phenomenon is observed in both regions of stall.

A comparison of Figures 4.5.9 and 4.5.10 indicates a time delay between the effect of the moving vortex on the pressure coefficient at x/C locations of 0.36 and 0.81. The motion of this vortex can also be seen in figures 4.5.4 through 4.5.7. From these figures it can be seen that the vortex moves with a nearly constant velocity toward the trailing edge of the airfoil at about 30% of the airfoil speed (rotor-tip-speed) or in other words the airfoil moves about 3.5 chord lengths while the vortex moves from the nose to the trailing edge.

5. CONCLUSIONS and RECOMMENDATIONS

In this chapter, a summary of the work performed is presented followed by a list of conclusions. Also, recommendations for future work are discussed.

5.1 Summary of the Analytical Study

The long-term goal for the present investigation is the development of a numerical model of dynamic stall as it occurs on Darrieus turbines. The current project has produced a numerical model theoretically capable of accomplishing this. The model is capable of predicting, with reasonable accuracy, steady and unsteady flows over aifoils with attached boundary layers and quasi-steady, separated flows.

The principal difficulty yet to be overcome before calculations of unsteady, separated flows can be made is the coupling of the viscid and inviscid calculations on a step-by-step basis. DYNA2 must incorporate this feature before any attempt can be made to simulate a dynamically stalled airfoil.

Of lesser importance is the issue of the basic surface modeling element. If higher order curved panels are utilized, then significantly higher computation costs will be incurred. Without their adoption, the DYNA2 will lack the reliability and generality needed of an aerodynamic design tool. It is suggested that the current planar elements be preserved during the continued development of DYNA2. The incorporation of advanced panel elements can be made during the final refinements.

5.2 Summary of the Experimental Investigation

The primary purpose of the investigation was to obtain instantaneous pressure distributions which are characteristic of the Darrieus turbine. In addition, measurements of transient aerodynamic blade forces were made using strain gage instrumentation.

From the measurements, it is apparent that dynamic stall is prevalent at a tip-to-windspeed ratio of 2.5. No stall was observed at tip-to-windspeed ratios of 5.1 and 7.6.

At the tip-to-windspeed ratio of 2.5, dynamic stall occurs over the inner surfaces at rotor angles of approximately $100° < \Theta < 140°$ corresponding to angles of attack of $20° < \alpha < 23°$. Dynamic stall over the outer surface occurs at rotor angles of approximately $265° < \Theta < 290°$ corresponding to angles of attack of $18° < \alpha < 23°$.

Boundary layer separation appears to proceed from the trailing edge to the leading edge. This is accompanied by the shedding of a vortex at the nose and the subsequent movement of the vortex over the stalled surface. The vortex moves toward the trailing edge at about one-half the airfoil speed.

For future experimental studies, it is recommended that the number of pressure taps be doubled and that additional probes be located on the opposite side of the airfoil.

6. REFERENCES

Arena, A. V., Mueller, T., 1980; "Laminar Separation, Transition, and Turbulent Reattachment Near the Leading Edge of Airfoils," AIAA Journal, 18(7), pp. 747-753.

Ashley, H.; "Machine Computation of Aerodynamic Loads in Linear and Nonlinear Situations," Fluid Dynamics Research Lab. Rept. 66-5, AFOSR 66-1440.

Cebecci, T. and Smith, A. M. O., 1974; Analysis of Turbulent Boundary Layers, Academic Press.

Cebecci, T. and Bradshaw, P., 1977; Momentum Transfer in Boundary Layers, McGraw-Hill.

Clements, R. R. and Maull, D. J., 1971; "The Representation of Sheets of Vorticity by Discrete Vortices," Prog. in Aerospace Sciences, 16, p. 129.

Coles, D., 1956; "The Law of the Wake in the Turbulent Boundary Layer," JFM, 1, pp. 191-226.

Coles, D. and Hirst, E. A., 1969; Computation of Turbulent Boundary Layers, 1968 AFOSR-RFP, Vol. 2, Stanford University.

Daneshyar, H. and Mugglestone, P. R., 1978; "An Integral Method for Calculating the Development of a Turbulent Boundary Layer with a Fluctuating Mainstream," Iranian J. of Science and Technology, 7, pp. 17-35.

Djojodihardjo, R. H. and Widaal, S. E., 1969; "A Numerical Method for the Calculation of Nonlinear, Unsteady Lifting Potential Flow Problems," AIAA J., 7, pp. 2001-2009.

Dwyer, H. A. and McCroskey, W. J., 1971; "Crossflow and Unsteady Boundary Layer Effects on Rotating Blades," AIAA J., 9, pp. 1498-1505.

Fanucci, J. B. and Walters, R. E., 1976; "Innovative Wind Machines: The Theoretical Performance of a Vertical Axis Wind Turbine, "Proceedings - Vertical Axis Wind Turbine Technology Workshop, Sandia Laboratory Report SAND76-5586.

Gormont, R. E., 1973; "A Mathematical Model of Unsteady Aerodynamics and Radial Flow for Application to Helicopter Rotors," USAAMRDL Technical Report 72-67.

Graham, G. M., 1982; "Measurement of Instantaneous Pressure Distributions and Blade Forces on an Airfoil Undergoing Cycloidal Motion," M.S. Thesis, Texas Tech University.

Green, J. E., Weeks, D. J., and Brooman, J. W. F., 1973; ARC R&M, 3791.

Ham, N. D., 1968; "Aerodynamic Loading on a Two-Dimensional Airfoil During Dynamic Stall," AIAA J., 6, p. 1927-1934.

Head, M. R., and Patel, V. C., 1969; "Improved Entrainment Method for Calculating Turbulent Boundary Layer Development," ARC R&M 3643.

Houdeville, R. and Cousteix, J., 1979, "Premiers Resultats D'une Etude sur les Couches Limites Turbulentes en Encoulement Pulse Avec Gradient de Pression Moyen Defavorable," 15E Collogue D;Aerodynamique, AAAF NT-79-05, 1978. Translated into English in NASA TN-75799, 1979.

Kadlec, E. G., 1980; "Overview of Current and Future Design Characteristics (of VAWT's), Proceedings - VAWT Design Technology Seminar for Industry, Sandia Laboratory Rept. SAND80-0984.

Karamcheti, K., 1966; Principles of Ideal-Fluid Aerodynamics, John Wiley and Sons.

Karlson, S. K. F., 1959; "An Unsteady Turbulent Boundary Layer," J. Fluid Mechanics, 5(4).

Kim, J., Kline, S. J., and Johnston, J. P., 1980; "Investigation of Separation and Reattachment of a Turbulent Shear Layer: Flow Over a Backward-Facing Step," Rpt. MD-37, Thermosciences Div., Mech. Engrg. Dept., Stanford University, 1978. See also TASME, J. Fluids Engrg., 102, pp. 392-308, 1980.

Klimas, P. C., 1980; "Vertical Axis Wind Turbine Aerodynamic Performance Prediction Methods," Proceedings - VAWT Design Technology Seminar for Industry, Sandia Laboratory Rept. SAND80-0984.

Klimas, P. C., 1980; "Possible Aerodynamic Improvements for Future VAWT Systems," Proceedings - VAWT Design Technology Seminar for Industry, Sandia Laboratory Reporrt SAND80-0984.

Kraus, W., 1978; "Panel Methods in Aerodynamics," Numerical Methods in Fluid Dynamics, McGraw-Hill, Editors Wirz and Smolderen, pp. 237-297.

Lyrio, A. A.,Ferziger, J. H., and Kline, S. J., 1981; "An Integral Method for the Computation of Steady and Unsteady Turbulent Boundary Layer Flows, Including the Transitory Stall Regime in Diffusers," Stanford University Report PD-23.

Martin, J. M., Empey, R. W., McCroskey, W. J., and Caradonna, F. S., 1974; "An Experimental Analysis of Dynamic Stall on an Oscillating Airfoil," J. Am. Helicopter Soc., 19, pp. 26-32.

McCroskey, W. J. and Phillippe, J. J., 1975; "Unsteady Viscous Flow on Oscillating Airfoils," AIAA J., 13, pp. 71-79.

Moore, F. K., 1958; "On the Separation of the Unsteady Boundary Layer," Boundary Layer Research, Gortler, H., (Ed.), Springer-Verlag, Berrlin, pp. 296-310.

Myring, D. F., 1970; RAE Tech Report 70147.

Nash, J. F. and Patel, V. C., 1969; "Improved Entrainment Method for Calculating Turbulent Boundary Layer Development," NASA CR-2546.

Nash, J. F., Carr L. W., and Singleton, R. E., 1975; Unsteady Turbulent Boundary Layers in Two-Dimensional Incompressible Flow," AIAA J., 13, pp. 176-183.

Nash, J. F., Carr, L. W., and Singleton, R. E., 1975; Unsteady Turbulent Boundary Layers in Two-Dimensional Incompressible Flow," AIAA J., 13, pp. 167-173.

Nash, J. F. and Scruggs, R. M., 1978; "Unsteady Boundary Layers with Reversal and Separation," Proceedings - Unsteady Aerodynamics, AGARD CP-227, pp. 18.1-18.12.

Newman, B. G., 1951; "Some Contributions to the Study of the Turbulent Boundary Layer Near Separation," Austr. Dept. Supply Rept. ACA-53.

Oler, J. W., 1976; "An Investigation of a Numerical Method for the Exact Calculation of Unsteady Airloads Associated with Wing Interaction Problems," M.S. Thesis, University of Texas - Austin.

Roberts, W. B., 1980; "Calculation of Laminar Separation Bubbles and Their Effect on Airfoil Performance," AIAA Journal, 18(1), pp. 25-31.

Rott, N., 1956; "Unsteady Flow in the Vicinity of a Stagnation Point," Quart. J. of Appl. Math., 13, pp. 444-451.

Sandborn, V. A. and Kline, S. J., 1961; "Flow Models in Boundary Layer Stall Inception," Journal of Basic Engineering, Trans. ASME, pp. 317-327.

Sarpkaya, T. and Schoaff, R. L., 1979; "Inviscid Model of Two-Dimensional Vortex Shedding by a Circular Cylinder," AIAA J., 17(11), pp. 1193-1200.

Sears, W. R., 1956; "Some Recent Developments in Airfoil Theory," 23, pp. 490-499.

Simpson, R. L., Strickland, J. H., and Barr, P. W., 1977; "Features of a Separating Turbulent Boundary Layer in the Vicinity of Separation," JFM, 79, pp. 553-594.

Singleton, R. E. and Nash, J. F., 1974; "Method for Calculating Unsteady Turbulent Boundary Layers in Two- and Three-Dimensional Flows," AIAA Journal, 12(5), pp. 590-595.

Smith, A. M. O. and Hess, J. L., 1962; "Calculation of the Nonlifting Potential Flow About Arbitrary Three-Dimensional Bodies," Douglas Rept. No. E.S. 40622.

Strickland, J. H., 1976; "Aerodynamics of the Darrieus Turbine," Proceedings - Vertical Axis Turbine Technology Workshop, Sandia Laboratory Rept. SAND76-5586.

Strickland, J. H., Webster, B. T., and Nguyen, T., 1979; "A Vortex Model of the Darrieus Turbine: An Analytical and Experimental Study," J. Fluids Engineering, 101(12), pp. 500-505.

Strickland, J. H., 1981; "Vortex Model of the Darrieus Turbine: An Analytical and Experimental Study," Sandia Laboratory Report SAND81-7017, 165 pages.

Strickland, J. H., Smith T., and Sun, K., 1981; "A User's Manual for the Vertical Axis Wind Turbine Code VDART2," Sandia Laboratory Report SAND81-7039, 50 pages.

Summa, J. M., 1976; "Potential Flow About Impulsively Started Rotors," J. Aircraft, 13, pp. 317-319.

Telionis, D. P., 1975; "Calculations of Time-Dependent Boundary Layers," Unsteady Aerodynamics, R. B. Kinney (Ed.), Vol. 1, p. 155.

Wilson, R. E., 1978; "Vortex Sheet Analysis of the Giromill," J. Fluids Engineering, 100(3), pp. 340-342.

Woodward, F. A., 1973; "An Improved Method for the Aerodynamic Analysis of Wing-Body-Tail Configurations in Subsonic and Supersonic Flow," NASA Cr-2228.

7. APPENDICES

APPENDIX A

FUNDAMENTALS OF POTENTIAL AERODYNAMICS

As an aid to understanding the unsteady aerodynamic solution method described in the preceeding chapters, a brief introduction to the fundamentals of low speed aerodynamic theory will now be given. Particular attention will be directed to the somewhat subtle aspects of lifting potential flow theory. Most of the theoretical relationships will be stated without proof. Their physical significance will be emphasized, however, and references given where the derivations and additional discussion may be found.

A.1 The Governing Equations

We are concerned with finding an Eulerian or "field" description of the motion of an ideal fluid through which one or more bodies move. An ideal fluid is defined as one that is inviscid, homogeneous, and incompressible. These assumptions are compatible with the physical realities of low speed aerodynamics.

The objective is to determine a set of governing equations which specify the relationship between the unknown vector velocity and scalar pressure fields. With these relationships and properly specified initial and boundary conditions, the unknown fields may be determined. The basis for these equations are the natural laws of conservation of mass and momentum.

Newton's second law of motion states that at any instant, the rate of change of momentum of any mechanical system is equal to the force acting on it at that instant. This requirement is described by

Euler's equation (see Karamcheti, pp. 175-190);

$$\frac{D}{Dt}(\rho\vec{U}) = \rho\vec{F} - \nabla P$$

or

$$\rho\{\frac{\partial\vec{U}}{\partial t} + [\vec{U}\cdot\nabla]\vec{U}\} = \rho\vec{F} - \nabla P$$

$$\text{mass x acceleration} = \begin{matrix}\text{body}\\ \text{force}\end{matrix} + \begin{matrix}\text{pressure}\\ \text{force}\end{matrix}.$$

Conservation of mass requires that the mass of an infinitesimal fluid element be constant. Since the fluid is incompressible, the mass per unit volume is a constant and it is sufficient to require that the velocity field not diverge. This is expressed by

$$\nabla\cdot\vec{U} = 0.$$

The vector conservation of momentum requirement provides three nonlinear equations, while the continuity equation yields a linear fourth. The simultaneous solution of these is sufficient to determine the unknown velocity components and pressure. The actual determination of that solution is quite difficult in most cases, however, due to the nonlinearity of the momentum equations.

A.2 Irrotational Motion

The Helmholtz theory of vortex motion states that in the motion of an ideal fluid through an irrotational force field, the material rate of change of the circulation around any fluid surface element is zero. This is expressed as (Karamcheti, p. 239)

$$\frac{D}{Dt}\oint_{C_S}\vec{U}\cdot\vec{ds} = \frac{D}{Dt}\Gamma_{C_S} = 0.$$

Kelvin's circulation theorem provides a slightly stronger statement of the same concept; in the motion of an ideal fluid through an irrotational force field, the circulation around a closed fluid curve remains constant for all time. This theorem is expressed as (Karamcheti, p. 242)

$$\frac{D}{Dt} \oint_C \vec{U} \cdot \vec{ds} = \frac{D}{Dt} \Gamma_C = 0.$$

Application of Stokes theorem on rotation to the Kelvin-Helmholtz circulation theorem yields a significant result. Through purely kinematical arguments, Stokes demonstrated that for any vector field in a region, R, the vorticity flux through an open surface contained in R is equal to the circulation around the closed curve which bounds the open surface. This is stated as (Karamcheti, p. 132)

$$\iint_S \vec{n} \cdot \vec{\zeta} \, dS = \int_C \vec{U} \cdot \vec{ds}$$

where

$$\vec{\zeta} = \nabla \times \vec{U}.$$

Combining this with the Kelvin-Helmholtz theorem yields

$$\frac{D\Gamma}{Dt} = \frac{D}{Dt} \iint_S \vec{n} \cdot \vec{\zeta} \, dS = 0.$$

Therefore, one concludes that for an ideal fluid in an irrotational force field, the vorticity flux through any fluid surface element is a constant. Furthermore, if that vorticity flux is zero for any instant, it must be zero for all times. This is the reason for generally assuming that ideal fluid motion is started from a state of rest or uniform motion in which case, $\vec{\zeta} = 0$ over the entire region occupied by the fluid. Since the vorticity is equal to twice the angular rotation rate of the fluid, it is said that the motion must be rotation free or irrotational for all times after the starting instant.

The requirement of irrotationality for all times is a necessary and sufficient condition to guarantee the existance of a velocity potential, i.e.,

$$\vec{\zeta} = \nabla \times \vec{U} = 0$$

therefore,

$$\vec{U} = \nabla\Phi.$$

The existence of a velocity potential has several important consequences with respect to the governing equations.

Euler's equation was given previously as

$$\rho\{\frac{\partial\vec{U}}{\partial t} + [\vec{U}\cdot\nabla]\vec{U}\} = \rho\vec{F} - \nabla P.$$

This may be rewritten as

$$\frac{\partial\vec{U}}{\partial t} + \nabla\left(\frac{U}{2}\right)^2 - \vec{U} \times [\nabla \times \vec{U}] = \vec{F} - \nabla\left(\frac{P}{\rho}\right).$$

Assuming an irrotational motion and force field yields

$$\frac{\partial}{\partial t}\nabla\Phi + \nabla[\frac{\nabla\Phi\cdot\nabla\Phi}{2}] = \nabla\Omega - \nabla\left(\frac{P}{\rho}\right)$$

or

$$\nabla\{\frac{\partial\Phi}{\partial t} + \frac{(\nabla\Phi)^2}{2} - \Omega + \frac{P}{\rho}\} = 0$$

where

$$\nabla\Phi = \vec{U} \text{ and } \nabla\Omega = \vec{F}.$$

After integration of the last expression, one arrives at

$$\frac{\partial\Phi}{\partial t} + \frac{1}{2}(\nabla\Phi)^2 - \Omega + \frac{P}{\rho} = f(t)$$

which is the unsteady Bernoulli's equation.

The conservation of mass requirement was previously given as

$$\nabla\cdot\vec{U} = 0.$$

Substitution of the velocity potential yields

$$\nabla^2\Phi = 0$$

which is the familiar Laplace equation.

Prior to the assumption of irrotationality and, thereby, the existence of a velocity potential, there were four equations for the unknown vector velocity and scalar pressure fields. Now, there are just two equations for the scalar velocity potential and pressure fields. Furthermore, the governing equation is now the linear Laplace equation. Since it is linear, complicated solutions for Φ may be constructed from the superposition of elementary ones. Once Φ is determined, the pressure field may be found from Bernoulli's equation.

A.3 The Circulation Theory of Lift

Consider the irrotational flow of an ideal fluid past a two-dimensional body. Since the body is two-dimensional, the flow field is said to be doubly connected and the possibility exists for a finite circulation around a circuit which includes the body.

d'Alembert considered the case in which the circulation is specified to be zero and came to the surprising conclusion that the net resistance forces of the fluid on the body are zero. This is commonly known as d'Alembert's paradox.

Kutta and Joukowski independently considered the case of nonzero circulation and found that a finite lift force was produced. The result is known as the Kutta-Joukowski theorem of lift and is stated as: if there is a circulation of magnitude Γ around the cylinder and if the undisturbed velocity at infinity has the magnitude U_∞, then a lift exists with a magnitude of $\rho U_\infty \Gamma$ per unit span.

The requirement of a net circulation for the generation of lift complicates the potential flow problem. From topology considerations (Karamcheti, pp. 252-263), it may be shown that a finite circulation can only exist for an irreducible circuit in a multiply connected region. A consequence of the multiple connectivity is that the potential field is not unique unless the circulations around the irreducible circuits are specified. Additional relationships based upon physical experience must be found to determine the circulation strengths, since the previously applied natural laws are of no help. In addition, consideration must be given to the Kelvin-Helmholtz theorem and how the circulation was established in the first place.

A.4 Two-Dimensional Airfoil Theory

If the flow field around an airfoil having a sharp trailing edge is calculated assuming zero circulation, a streamline pattern similar to the one shown in Figure A.1 results. As a consequence of the surface gradient discontinuity at the trailing edge, a velocity singularity exists at that point. Physical experience has demonstrated that an infinite velocity cannot exist in any real fluid with a finite viscosity. Realization of this deficiency in the ideal fluid representation led Kutta and Joukowski to propose that the circulation about the airfoil be such that the flow from the trailing edge be smooth and finite. This is typically known as the Kutta condition. It provides the additional relationship which is necessary to uniquely specify the circulation strength and potential field.

Now consider a two-dimensional airfoil at rest in an ideal fluid. Since the fluid velocity is everywhere zero, the circulation around the airfoil is zero. At the initial instant, $t = 0$, the fluid is instantaneously brought into motion such that at infinity, $U = U_\infty$. The Kutta condition requires that the fluid flow smoothly off of the trailing edge and, consequently, that there be a finite circulation around the airfoil. The Kelvin-Helmholtz theorem, however, requires that the circulation about any closed curve in the fluid be zero. The simultaneous satisfaction of these apparently contradictory conditions is accomplished by the generation of a trailing wake which forms the starting vortex illustrated in Figure A.2.

For any incremental time interval, δt, the vorticity shed from the trailing edge into the wake is equal to the negative of the change in "bound vorticity" or equivalently, circulation strength about the air-

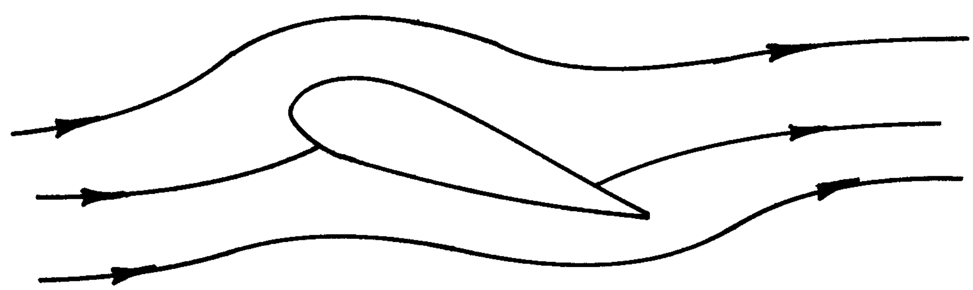

Figure A.1 Flow Field About an Airfoil With Zero Circulation

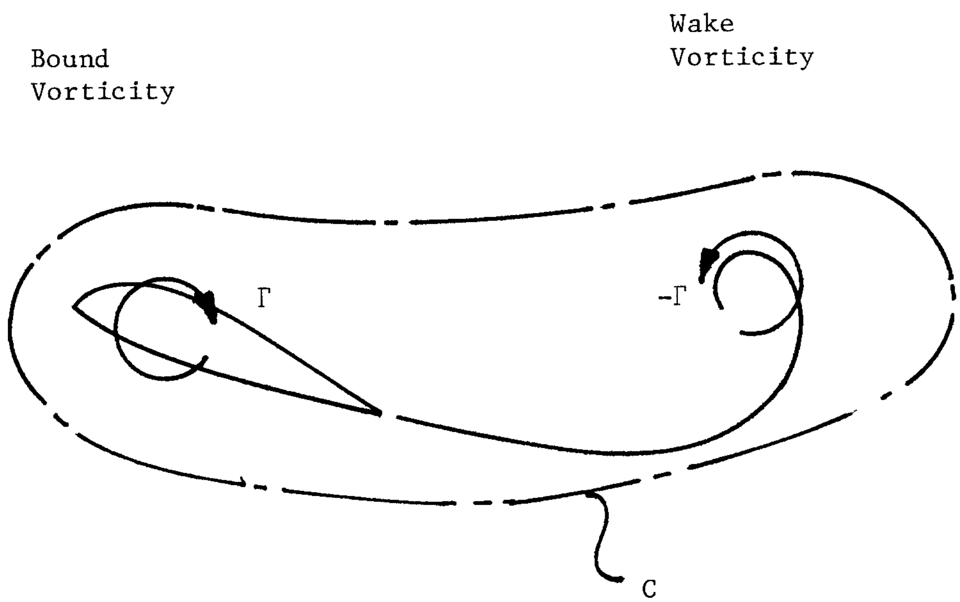

$$\Gamma_c = \int_C \vec{U} \cdot \vec{d\ell} = 0$$

Figure A.2 Flow About an AirFoil Which Satisfies the Kutta Condition foil during that time interval. Referring to Figure A.2, this can be expressed mathematically as

$$\delta\Gamma_w = -\frac{d\Gamma_b}{dt}\,\delta t.$$

Therefore, the net circulation around the wake is always the exact negative of the circulation around the airfoil, i.e.,

$$\Gamma_w = \int_0^T -\frac{d\Gamma_b}{dt}\,dt = -\Gamma_b.$$

The wake surface is a sheet of potential discontinuity and, consequently, a boundary in the flow field. All closed fluid circuits of the Kelvin-Helmholtz type must include the entire lifting system of airfoil plus the trailing wake as shown in Figure A.2. The net circulation around these circuits, Γ_{K-H}, is zero for the starting instant and all later times.

A.5 Three-Dimensional Airfoil Theory

A similar situation exists for finite wings as illustrated in Figure A.3. Before the starting instant, the fluid is at rest and the circulation strengths about all closed fluid curves in the region are zero. After the starting instant, a unique circulation strength of the bound vortex is determined by the Kutta condition at the trailing edge. Since it is not possible for a vortex tube to end in a fluid, away from the boundaries, two tip vortices must be shed. Downstream, the tip vortices are joined to the starting vortex. For the simplified flow situation depicted in Figure A.3,

$$|\Gamma_T| = |\Gamma_b| = |\Gamma_w|.$$

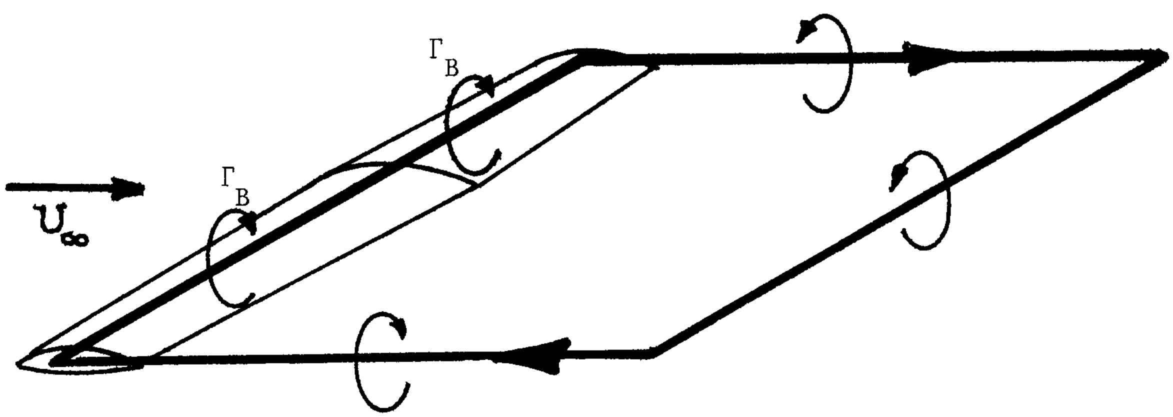

Figure A.3 Vortex System for a Finite Wing

Consequently, any closed circuit about the complete lifting system will have zero circulation. This is sufficient to satisfy the Kelvin-Helmholtz theorem.

APPENDIX B

AN INTEGRAL SOLUTION TO LAPLACE'S EQUATION

In this appendix, it will be shown that any solution to Laplace's equation may be expressed in terms of integrals of potential doublets and sources distributed over the boundaries of the solution domain. We will begin in the first section with a derivation of Green's theorem and in the following section demonstrate its application for the determination of the desired integral solution to Laplace's equation.

B.1 Green's Theorem

Gauss' divergence theorem expresses the equivalence of the divergence of a vector field within an enclosed volume with the flux of that vector field across the boundary surface. The mathematical statement of the theorem is

$$\iiint_V \nabla \cdot \vec{A} \, dV = \oiint_S \vec{A} \cdot \vec{n} \, dS \qquad (B.1)$$

where $\vec{A}$ = any vector field

V = enclosed volume

S = bounding surface

$\vec{n}$ = outwardly directed surface normal.

For the vector field, $\vec{A}$, we may choose

$$\vec{A} = \phi \nabla \phi'$$

where ϕ and ϕ' are continuous functions having finite first and second derivatives within the volume, V. Substitution for $\vec{A}$ in Equation B.1

yields

$$\iiint_V \nabla\cdot\phi\nabla\phi' \, dV = \oiint_S \phi\nabla\phi'\cdot\vec{n} \, dS. \tag{B.2}$$

Equation B.2 may be expanded to give

$$\iiint_V [\nabla\phi\cdot\nabla\phi' + \phi\nabla^2\phi']dV = \oiint_S \phi \frac{\partial\phi}{\partial n} \, dS \tag{B.3}$$

which is known as Green's theorem in the first form.

We may alternately choose for A in Equation B.1

$$\vec{A} = \phi'\nabla\phi - \phi\nabla\phi'$$

Performing the substitution yields

$$\iiint_V \nabla(\phi'\nabla\phi - \phi\nabla\phi')dV = \oiint_S (\phi'\nabla\phi - \phi\nabla\phi')\cdot\vec{n} \, dS$$

or

$$\iiint_V (\phi'\nabla^2\phi - \phi\nabla^2\phi')dV = \oiint_S (\phi' \frac{\partial\phi}{\partial n} - \phi \frac{\partial\phi}{\partial n})dS. \tag{B.5}$$

Equation B.5 is known as Green's theorem in the second form.

B.2 Green's Theorem for Irrotational Acyclic Flow

We now wish to consider the motion of a body having surface S in an ideal fluid with an outer boundary surface Σ. It is assumed that the fluid motion was started from a state of rest or uniform motion so that it is irrotational for all times. We further assume that the flow is acyclic (i.e., $\Gamma = 0$ about all closed fluid curves) so that a single-valued solution, $\phi(\vec{r},t)$, to Laplace's equation must exist.

Recalling Green's theorem in the second form, Equation B.5, let

$$\phi = \phi(\vec{r},t) \quad \text{where} \quad \nabla^2\phi = 0$$

and

$$\phi' = \frac{1}{R} \quad \text{where} \quad R = |\vec{r}-\vec{\zeta}|.$$

Here we note that R is simply the distance between a fixed point, P, located by $\vec{r}$ and any point in the volume, V. Since $\nabla^2\phi' = 0$ except at $\vec{\zeta} = \vec{r}$, an infinitesimal spherical boundary surface, σ, is placed about P as shown in Figure B.1, thereby excluding it from the volume, V.

Under these conditions, Equation B.5 becomes

$$0 = I_1 + I_2 + I_3 \tag{B.6}$$

where

$$I_1 = \oiint_S \left[\frac{\partial\phi}{\partial n}\frac{1}{R} - \phi\frac{\partial}{\partial n}\left(\frac{1}{R}\right)\right]dS \tag{B.6a}$$

$$I_2 = \oiint_\Sigma \left[\frac{\partial\phi}{\partial n}\frac{1}{R} - \phi\frac{\partial}{\partial n}\left(\frac{1}{R}\right)\right]dS \tag{B.6b}$$

$$I_3 = \oiint_\sigma \left[\frac{\partial\phi}{\partial n}\frac{1}{R} - \phi\frac{\partial}{\partial n}\left(\frac{1}{R}\right)\right]dS \tag{B.6c}$$

To determine the potential, $\phi(\vec{r},t)$, due to the motion of S, we consider the limits of I_2 and I_3 as $\Sigma\rightarrow\infty$ and $\sigma\rightarrow 0$, respectively. Equation B.6b may be shown to go to zero as $\Sigma\rightarrow\infty$, since the fluid at infinity is at rest or in uniform motion and ϕ and $\frac{\partial\phi}{\partial n}$ must vanish there. Now consider Equation B.6c. Noting that since σ is a spheri-

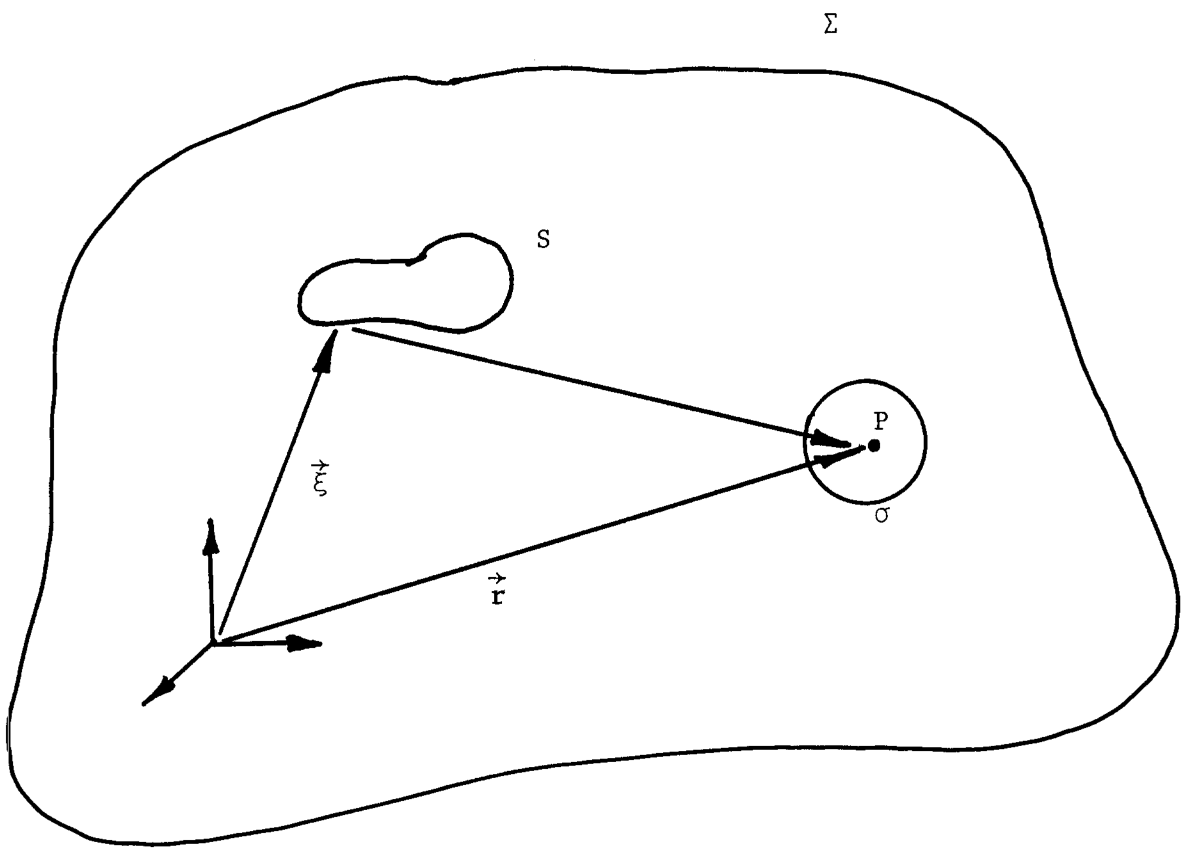

Figure B.1 Intergration Regions for Equation B.6

cal surface, then $R = \varepsilon$ and $\frac{\partial}{\partial n} = \frac{\partial}{\partial \varepsilon}$, and the equation may be rewritten as

$$I_3 = \lim_{\varepsilon \to 0} \iint_\sigma \left[\frac{\partial \phi}{\partial \varepsilon} \frac{1}{\varepsilon} - \phi \frac{\partial}{\partial \varepsilon} \left(\frac{1}{\varepsilon}\right)\right] \varepsilon^2 d\Omega \tag{B.7}$$

where $d\Omega$ = differential solid angle. By the mean value theorem of integration, it is possible to determine mean surface values of ϕ and $\frac{\partial \phi}{\partial n}$ such that Equation B.7 becomes

$$I_3 = \lim_{\varepsilon \to 0} \left.\frac{\partial \phi}{\partial \varepsilon}\right|_{mean} \oiint_\sigma \frac{\varepsilon^2}{\varepsilon} d\Omega + \lim_{\varepsilon \to 0} \phi \Big|_{mean} \oiint_\sigma \frac{\varepsilon^2}{\varepsilon^2} d\Omega$$

or

$$I_3 = 4\pi \, \phi(\vec{r}) . \tag{B.8}$$

From the preceding conclusions, Equation B.6 becomes

$$\phi(\vec{r}) = \frac{1}{4\pi}\left\{-\oiint_S \frac{\partial \phi}{\partial n} \frac{1}{R} dS + \oiint_S \phi \frac{\partial}{\partial n}\left(\frac{1}{R}\right) dS\right\} \tag{B.9}$$

which is the desired integral solution to Laplace's equation. A notable feature of Equation B.9 is that the potential at any given point in the fluid flow field is determined by the potential and its normal derivative on the bounding surface. In addition, the terms $\frac{1}{4\pi R}$ and $\frac{\partial}{\partial n}[\frac{1}{4\pi R}]$ may be recognized as potential sources and doublest, respectively.

Although the previous derivation was given for a three-dimensional flow field, equivalent relations for a two-dimensional field may be determined also. In this case, Gauss' divergence theorem relates surface and line integrals rather than volume and surface integrals. The derivation of Green's theorem proceeds in exactly the same way. The result is given by

$$\iint_S (\phi'\nabla^2\phi - \phi\nabla^2\phi')\,dS = \oint_C (\phi' \frac{\partial\phi}{\partial n} - \phi \frac{\partial\phi'}{\partial n})\,d\ell. \tag{B.10}$$

We allow ϕ to be the solution of $\nabla^2\phi = 0$ and choose $\phi = \ell n(R)$ where $R = |\vec{r}-\vec{\zeta}|$ as before. Substitution into Equation B.10 yields

$$0 = \oint_{\sigma+\Sigma+S} [\ell n\ R \frac{\partial\phi}{\partial n} - \phi \frac{\partial}{\partial n}(\ell n\ R)]\,d\ell. \tag{B.11}$$

If we take the limits as $\Sigma\to\infty$ and $\sigma\to 0$, the two-dimensional equivalent of Equation B.9 results and is given by

$$\phi(\vec{r}) = -\oint_C [\frac{\ell nR}{2\pi} \frac{\partial\phi}{\partial n} + \frac{\phi}{2\pi} \frac{\partial}{\partial n}(\ell n\ R)]\,d\ell. \tag{B.12}$$

For this case, the surfaces are represented by two-dimensional sources and doublets.

APPENDIX C

UNIQUENESS REQUIREMENTS FOR THE INTEGRAL SOLUTION

Consider an interior and exterior flow separated by a bounding surface, S, as shown in Figure C.1. Let $\phi_E(\vec{r},t)$ be the solution of $\nabla^2\phi_E$ for the exterior flow and $\phi_I(\vec{r},t)$ be the solution for the interior flow.

Recall that Green's theorem was given by Equation B.5 as

$$\iiint_V (\phi'\nabla^2\phi - \phi\nabla^2\phi')dV = \oint\!\!\oint_S (\phi' \frac{\partial\phi}{\partial n} - \phi \frac{\partial\phi'}{\partial n})dS. \tag{C.1}$$

For the exterior flow, we choose $\phi = \phi_E$ and $\phi_E = \frac{1}{R}$ where $R = |\vec{r}-\vec{\zeta}_E|$. Now $\nabla^2\phi_E = 0$ everywhere except at $\vec{\zeta} = \vec{r}$. Consequently, by surrounding the point P at $\vec{r}$ with a spherical boundary and taking the limit as the sphere is reduced to P, we find that (as shown in Appendix B)

$$\phi(\vec{r},t) = \frac{-1}{4\pi} \oint\!\!\oint_S [\frac{\partial\phi_E}{\partial n_E} \frac{1}{R} - \phi_E \frac{\partial}{\partial n} \left(\frac{1}{R}\right)]dS. \tag{C.2}$$

For the interior flow, $\phi = \phi_I$, and again, $\phi_I = \frac{1}{R}$. Since we are only concerned with the points P exterior to S, $R = |\vec{r}-\vec{\zeta}_I|$ cannot be zero and $\nabla^2\phi_I = 0$ for all $\vec{\zeta}_I$. Equation C.1 for the interior problem may be written as

$$0 = \frac{-1}{4\pi} \oint\!\!\oint_S [\frac{\partial\phi_I}{\partial n_I} \frac{1}{R} - \phi_I \frac{\partial}{\partial n_I} \left(\frac{1}{R}\right)]dS. \tag{C.3}$$

Adding the exterior and interior solutions, Equations C.2 and C.3, respectively, yields

$$\phi(\vec{r},t) = \frac{-1}{4\pi} \oint\!\!\oint_S \left(\frac{\partial\phi_E}{\partial n_E} + \frac{\partial\phi_I}{\partial n_I}\right)\frac{1}{R}]dS$$

$$+ \frac{1}{4\pi} \oint\!\!\oint_S [\phi_E \frac{\partial}{\partial n_E} \left(\frac{1}{R}\right) + \phi_I \frac{\partial}{\partial n_I} \left(\frac{1}{R}\right)]dS \tag{C.4}$$

Noting that $\frac{\partial}{\partial n_E} = - \frac{\partial}{\partial n_I}$, Equation C.4 may be rewritten as

$$\phi(\vec{r},t) = \frac{-1}{4\pi} \oint\!\!\oint_S \left[\left(\frac{\partial \phi_E}{\partial n_E} - \frac{\partial \phi_I}{\partial n_E} \right) \frac{1}{R} \right] dS$$

$$+ \frac{1}{4\pi} \oint\!\!\oint_S \left[(\phi_E - \phi_I) \frac{\partial}{\partial n_E} \left(\frac{1}{R} \right) \right] dS. \tag{C.5}$$

From Equation C.5, it is noted that the external potential field is again determined by surface distributions of potential sources and doublets. In this case, however, it is clear that the strength distributions of the singularities is dependent on the interior flow. Suppose that the interior flow is such that $\phi_I = \phi_E$ on S, thereby requiring a continuous tangential velocity across S, with the possibility of a discontinuous normal velocity left open. Equation C.5 reduces to

$$\phi(\vec{r},t) = \frac{-1}{4\pi} \oint\!\!\oint_S \left[\left(\frac{\partial \phi_E}{\partial n_E} - \frac{\partial \phi_I}{\partial n_E} \right) \frac{1}{R} \right] dS \tag{C.6}$$

illustrating that the potential field may be represented by a surface distribution of sources.

Suppose that $\frac{\partial \phi_E}{\partial n_E} = \frac{\partial \phi_I}{\partial n_E}$ so that the normal velocity across S is continuous while the tangential velocity may be discontinuous. Equation C.5 reduces to

$$\phi(\vec{r},t) = \frac{1}{4\pi} \iint_S \left[(\phi_E - \phi_I) \frac{\partial}{\partial n_E} \left(\frac{1}{R} \right) \right] dS \tag{C.7}$$

which provides an expression for $\phi(\vec{r},t)$ with a surface distribution of doublets.

We may generalize the preceding discussion by stating that a solution to Laplace's equation may be uniquely represented by surface distributions of

1) sources only

2) doublets only

3) sources and doublets on separated portions of the surface

4) linearly related distributions of sources and doublets.

As a final comment, it is noted that doublet distributions are required on lifting surfaces, since only they allow the possibility of discontinuous tangential velocities and finite circulations.

APPENDIX D

EQUIVALENT DOUBLET AND VORTEX SURFACE DISTRIBUTIONS

The objective for this appendix is to demonstrate the equivalence of surface distributions of potential doublets and vortices. This will be accomplished by first deriving the expression for the potential of a three-dimensional doublet. The velocity field induced by a vortex segment will then be derived, and from that the velocity potential induced by a ring vortex will be determined. It will then be clear that the potential field due to a distribution of uniform strength doublets over an open surface is equivalent to that induced by a line vortex around the boundary of the surface with strength equal to that of the doublets. Finally, the general conclusion will be drawn that any surface distribution of doublets may be represented by a distribution of vortices oriented normal to the gradient of doublet strength and having strengths equal to that gradient.

D.1 The Potential Doublet

A potential doublet may be formed by taking the limit as a potential source and sink are brought together where the axis of the doublet is along the line connecting source and sink centers as shown in Figure D.1. This is expressed by

$$\underset{\text{doublet}}{\phi(\vec{r})} = \lim_{\delta s \to 0} \left[\underset{\text{source}}{\phi(\vec{r})} + \underset{\text{sink}}{\phi(\vec{r} + \vec{\delta s})} \right]$$

$$= \lim_{\delta s \to 0} \left[\underset{\text{source}}{\phi(\vec{r})} - \underset{\text{source}}{\phi(\vec{r} + \vec{\delta s})} \right]$$

$$= \lim_{\delta s \to 0} \underset{\text{source}}{\nabla\phi(\vec{r})} \cdot \vec{\delta s}$$

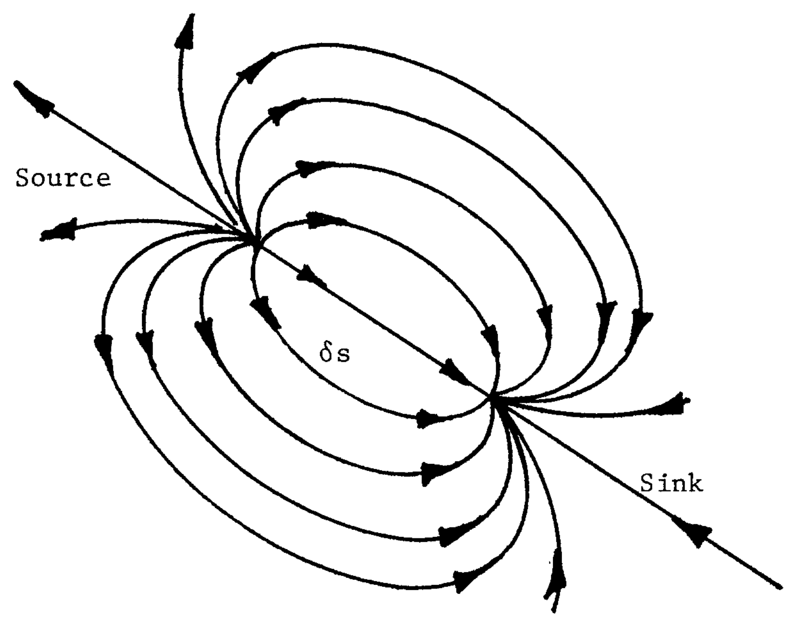

Figure D.1 Doublet as a Combined Source and Sink Flow

$$= \nabla\phi(\vec{r})_{\text{source}} \cdot \vec{e}_s$$

$$= \frac{\mu}{4\pi} \nabla \left(\frac{1}{R}\right) \cdot \vec{e}_s \qquad \text{(D.1)}$$

where

$$R = |\vec{r}-\vec{\zeta}|.$$

From Equation D.1, the potential field due to a surface distribution of doublets is given by

$$\phi(\vec{r}) = \iint_S \frac{\mu}{4\pi} \nabla\left(\frac{1}{R}\right) \cdot \vec{n}\, dS \qquad \text{(D.2)}$$

where $\vec{n}$ = the surface normal.

D.2 Velocity Field Induced by a Vortex Segment

For an ideal fluid, the incompressibility requirement may be stated as

$$\nabla \cdot \vec{U} = 0$$

Since for all vector fields, A, it is true that

$$\nabla \cdot (\nabla \times \vec{A}) = 0$$

we may choose

$$\vec{U} = \nabla \times \vec{A}. \qquad \text{(D.3)}$$

Given U_1, the vorticity field is given by

$$\vec{\Omega} = \nabla \times \nabla \times \vec{A}$$

or

$$\vec{\Omega} = \nabla(\nabla\cdot\vec{A}) - \nabla^2\vec{A} \tag{D.4}$$

Since $\vec{A}$, to this point, is indeterminate to the extent of the gradient of a vector, we may further stipulate that

$$\nabla\cdot\vec{A} = 0 \tag{D.5}$$

With Equation D.5, Equation D.4 may be rewritten as

$$\nabla^2\vec{A} = -\vec{\Omega}$$

This is Poisson's equation for $\vec{A}$. By solving for $\vec{A}$, it will then be possible to determine the velocity field utilizing Equation D.3.

Consider the solution of the vector relationship, Equation D.6, which has the following component equations:

$$\begin{aligned} \nabla^2 A_x &= -\Omega_x \\ \nabla^2 A_y &= -\Omega_y \\ \nabla^2 A_z &= -\Omega_z \end{aligned} \tag{D.7a,b,c}$$

It is sufficient to determine the solution of C.7a over all space, keeping in mind that $\vec{U}$ and $\vec{A}$ must vanish at infinity.

Recall that Green's theorem was given by Equation B.5 as

$$\iiint_V (\phi'\nabla^2\phi - \phi\nabla^2\phi')dV = \iint_S (\phi' \frac{\partial\phi}{\partial n} - \frac{\partial\phi'}{\partial n})dS \tag{D.8}$$

For ϕ and ϕ', choose

$$\phi = A_x \tag{D.9}$$

$$\phi' = 1/R \tag{D.10}$$

where

$$R = |\vec{r} - \vec{r}_1|$$

Therefore,

$$\begin{aligned}
\nabla\phi &= \nabla A_x \\
\nabla^2\phi &= \nabla^2 A_x \\
\nabla^2\phi &= -\,\Omega_x \\
\nabla\phi' &= \vec{R}/R^3 \\
\nabla\phi' &= 0 \quad \text{for } \vec{r} \neq \vec{r}_1 \\
&= \infty \quad \text{for } \vec{r} = \vec{r}_1
\end{aligned} \tag{D.11}$$

Substitution of Equations D.9 - D.11 into Equation D.8 yields

$$\begin{aligned}
\iiint_V \frac{\Omega x}{R}\, dV = &- \lim_{\Sigma} \iint_\Sigma \left(A_x \nabla\left(\frac{1}{R}\right) + \frac{\nabla A_x}{R}\right)\cdot\vec{n}\, dS \\
&- \lim_{\sigma\to\infty} \iint_\sigma \left(A_x \nabla\left(\frac{1}{R}\right) + \frac{\nabla A_x}{R}\right. \cdot\vec{n}\, dS
\end{aligned} \tag{D.12}$$

where Σ = outer boundary

σ = spherical shell about singular point at $\vec{r}_1 = \vec{r}$.

The surfaces Σ and σ, as well as the vectors $\vec{r}$, $\vec{r}_1$ and $\vec{R}$ are illustrated in Figure D.2.

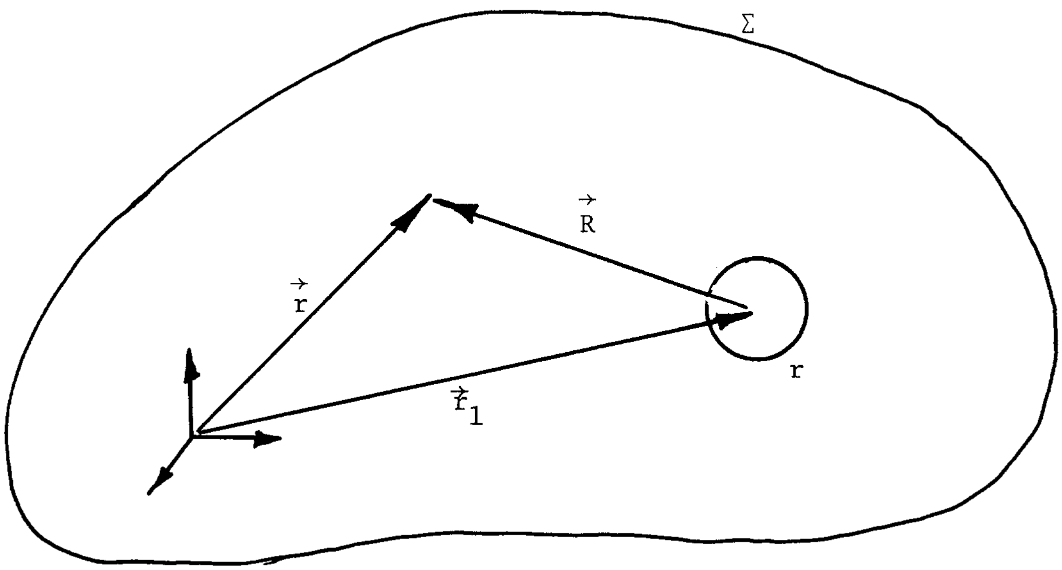

Figure D.2 Integration Regions for Equation D.12

If we consider the first integral of the right hand side of Equation D.12 and allow Σ to be a spherical surface which spreads to infinity in the limit, it follows that

$$0 = \lim_{R\to\infty} \iint_\Sigma \left(\frac{-A_x}{R^2}\right) + \frac{1}{R}\frac{\sigma A_x}{\sigma R}\right) R^2 \; d\Omega \tag{D.13}$$

where $d\Omega$ = differential solid angle and it is assumed that

$$\lim_{R\to\infty} \frac{R}{\sigma A_x/\sigma R} = 0$$

For the second integral over σ,

$$I_2 = \lim_{R\to 0} \iint_\sigma \left(\frac{-A_x}{R^2} + \frac{1}{R}\;\frac{\sigma A_x}{\sigma R}\right) R^2 \; d\Omega$$

$$I_2 = \lim_{R\to 0} \Big(-A_x\Big|_{mean} \iint_\sigma d\Omega + \frac{\sigma A_x}{\sigma R}\Big|_{mean} \iint_\sigma d\Omega \tag{D.14}$$

$$I_2 = -\,4\pi\,A_x(\vec{r}_1)$$

Substitution of Equations D.13 and D.14 into Equation D.12 yields

$$A_x(\vec{r}) = \frac{1}{4\pi} \iiint_V \frac{\Omega_x(\vec{r}_1)}{R} \; dV \tag{D.15}$$

When the equivalent solutions for Equation D.7b and c are determined, we may write

$$\vec{A}(\vec{r}) = \frac{1}{4} \iiint_V \frac{\vec{\Omega}(\vec{r}_1)}{R} \; dV \tag{D.16}$$

Now from Equations D.3 and D.16, we may determine the velocity field resulting in the vorticity distribution, $\vec{\Omega}(\vec{r})$;

$$\vec{U} = \nabla_r \times \vec{A} = \frac{1}{4} (\nabla_r \times \iiint_V \frac{\vec{\Omega}(\vec{r}_1)}{R} \, dV \tag{D.17}$$

We now wish to determine the velocity field induced by an infinitesimal vortex filament with strength Γ as shown in Figure D.3. From Equation D.16, the incremental contribution to $\vec{A}$ from the filament may be written as

$$\begin{aligned} \delta \vec{A}(\vec{r}) &= \frac{1}{4\pi} \frac{\vec{\Omega}(\vec{r}_1)}{R} \, dV \\ &= \frac{1}{4\pi} \frac{\vec{\Omega}(\vec{r}_1)}{R} \vec{n} \, dS \cdot d\vec{\ell} \end{aligned} \tag{D.18}$$

We may write

$$d\vec{\ell} = \frac{\vec{\Omega}}{\Omega} \, d\ell$$

and

$$\vec{\Omega} \cdot \vec{n} \, dS = \Gamma$$

so that Equation D.18 may be rewritten as

$$\delta\vec{A}(\vec{r}) = \frac{\Gamma}{4\pi} \frac{d\vec{\ell}}{R}$$

Consequently, the incremental velocity from the vortex filament is

$$\begin{aligned} \delta\vec{U}(\vec{r}) &= \frac{\Gamma}{\pi} \quad {}_r \times \frac{d\vec{\ell}}{R} \\ &= \frac{\Gamma}{4\pi} d\vec{\ell} \times \nabla_r \left(\frac{1}{R}\right) \end{aligned} \tag{D.20}$$

where $\vec{d\ell}$ and $\vec{r}_1$ are fixed and ∇_r indicates that the curl is to be

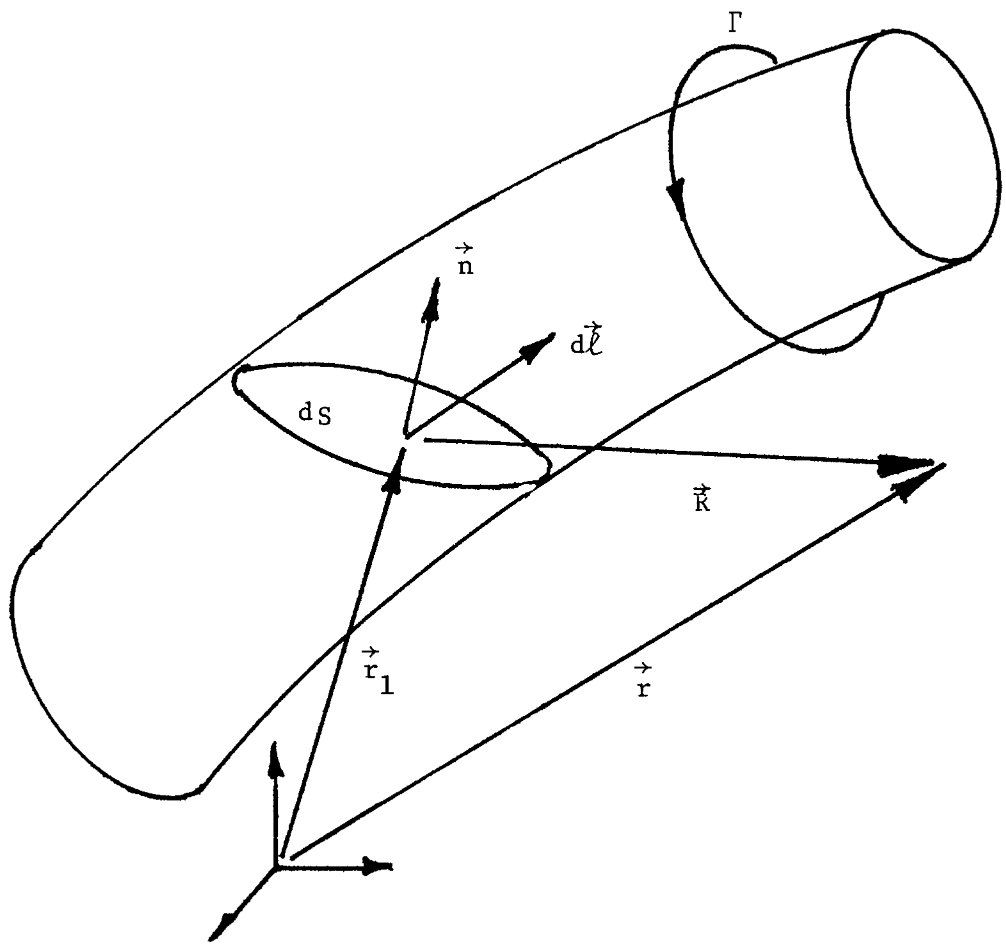

Figure D.3 Velocity Induced by a Vortex Line taken with respect to the coordinates of the point $\vec{r}$.

Finally, the velocity induced by a vortex segment is

$$\vec{U}(\vec{r}) = \frac{\Gamma}{4\pi} \int_c d\vec{\ell} \times \nabla \left(\frac{1}{R}\right)$$

which is the well known Biot-Savart law.

D.3 Velocity Field of a Vortex Ring

We would now like to determine the velocity field induced by a vortex ring. Equation D.21 may be written in component form for a closed vortex ring as

$$U_x(\vec{r}) = \frac{\Gamma}{4\pi} \int_c \left[\frac{\sigma}{\sigma z} \left(\frac{1}{R}\right) d\ell_y - \frac{\sigma}{\sigma y} \left(\frac{1}{R}\right) d\ell_z\right] \quad \text{(D.22a)}$$

$$V_y(\vec{r}) = \frac{\Gamma}{4\pi} \int_c \left[\frac{\sigma}{\sigma x} \left(\frac{1}{R}\right) d\ell_z - \frac{\sigma}{\sigma z} \left(\frac{1}{R}\right) d\ell_x\right] \quad \text{(D.22b)}$$

$$U_z(\vec{r}) = \frac{\Gamma}{4\pi} \int_c \left[\frac{\sigma}{\sigma y} \left(\frac{1}{R}\right) d\ell_x - \frac{\sigma}{\sigma x} \left(\frac{1}{R}\right) d\ell_y\right] \quad \text{(D.22c)}$$

By Stokes' theorem, Equation D.22a may be rewritten as

$$U_x(\vec{r}) = \int_c \vec{\zeta} \cdot d\vec{\ell} = \iint_S (\nabla \times \vec{\zeta}) \cdot \vec{n} dS \quad \text{(D.23)}$$

where

$$\vec{\zeta} = \frac{\Gamma}{4\pi} \left[\frac{\sigma}{\sigma z} \left(\frac{1}{R}\right) \vec{e}_y - \frac{\sigma}{\sigma y} \left(\frac{1}{R}\right) \vec{e}_z \right]$$

By expanding Equation D.23, we find that

$$U_x(\vec{r}) = \frac{\Gamma}{4\pi} \iint_S \left[\left(- \frac{\sigma^2}{\sigma y^2} - \frac{\sigma^2}{\sigma z^2}\right) \frac{1}{R} e_x + \frac{\sigma^2}{\sigma x \sigma y} \left(\frac{1}{R}\right) \vec{e}_y + \frac{\sigma^2}{\sigma x \sigma z} \left(\frac{1}{R}\right) \vec{e}_z\right] \cdot \vec{n} \, dS \quad \text{(D.24)}$$

$$= \frac{\Gamma}{4\pi} \iint_S \nabla \left(\frac{\sigma}{\sigma x} \frac{1}{R} \right) \cdot \vec{n} \, dS$$

Similarly, for the other two component equations;

$$U_y(\vec{r}) = \frac{\Gamma}{4\pi} \iint_S \nabla(\frac{\sigma}{\sigma y} \frac{1}{R}) \cdot \vec{n} dS$$

$$U_z(\vec{r}) = \frac{\Gamma}{4\pi} \iint_S \nabla(\frac{\sigma}{\sigma z} \frac{1}{R}) \cdot \vec{n} dS$$

We conclude that

$$\vec{U}(\vec{r}) = \frac{\Gamma}{4\pi} \iint_S \nabla \; [\nabla \; (\frac{1}{R}) \cdot \vec{n}] \; dS \tag{D.25}$$

and

$$\phi(\vec{r}) = \frac{\Gamma}{4\pi} \iint_S \nabla \; (\frac{1}{R}) \cdot \vec{n} \; dS \tag{D.26}$$

D.4 Equivalency of Doublet and Vortex Distributions

To summarize, in Section D.1, the potential due to an isolated doublet was derived. Following that, the potential due to a surface distribution of doublets was given by Equation D.2. For the special cases of distribution of uniform strength doublets, the potential becomes

$$\phi(\vec{r}) = \frac{\mu}{4\pi} \iint_S \nabla \; (\frac{1}{R}) \cdot \vec{n} \; dS \tag{D.27}$$

where $n = n(\zeta)$, the surface normal and

$$R = | \; \vec{r} - \vec{\xi} \; |$$

In sections D.2 and D.3, the velocity potential due to a vortex ring was determined by deriving the velocity field due to an arbitrary distribution of vorticity and specializing it for the case of an isolated vortex filament. The resulting potential field of a vortex ring given by Equation D.2 and is repeated here;

$$\phi(\vec{r}) = \frac{\Gamma}{4\pi} \iint_S \nabla \left(\frac{1}{R}\right) \cdot \vec{n}\, dS \tag{D.28}$$

where S is any open surface bounded by the vortex ring.

Comparison of Equations D.27 and D.28 reveals that a vortex ring of strength Γ is equivalent to a distribution of doublets with strengths $\mu = \Gamma$ over any arbitrarily shaped surface bounded by the vortex ring. If two constant strength doublet surfaces share a common boundary, as shown in Figure D.4, it follows that the potential for that segment of the boundary is equivalent to a vortex segment with a strength equal to the difference of the doublet strengths. This idea may be carried further by envisioning any surface as being made up of infinitesimal areas of constant strength doublets. In the limit, as the areas are reduced to points, the equivalent vortex representation would be a vortex sheet with the filaments directed normal to the gradient of doublet strength and filament circulations equal to the gradient.

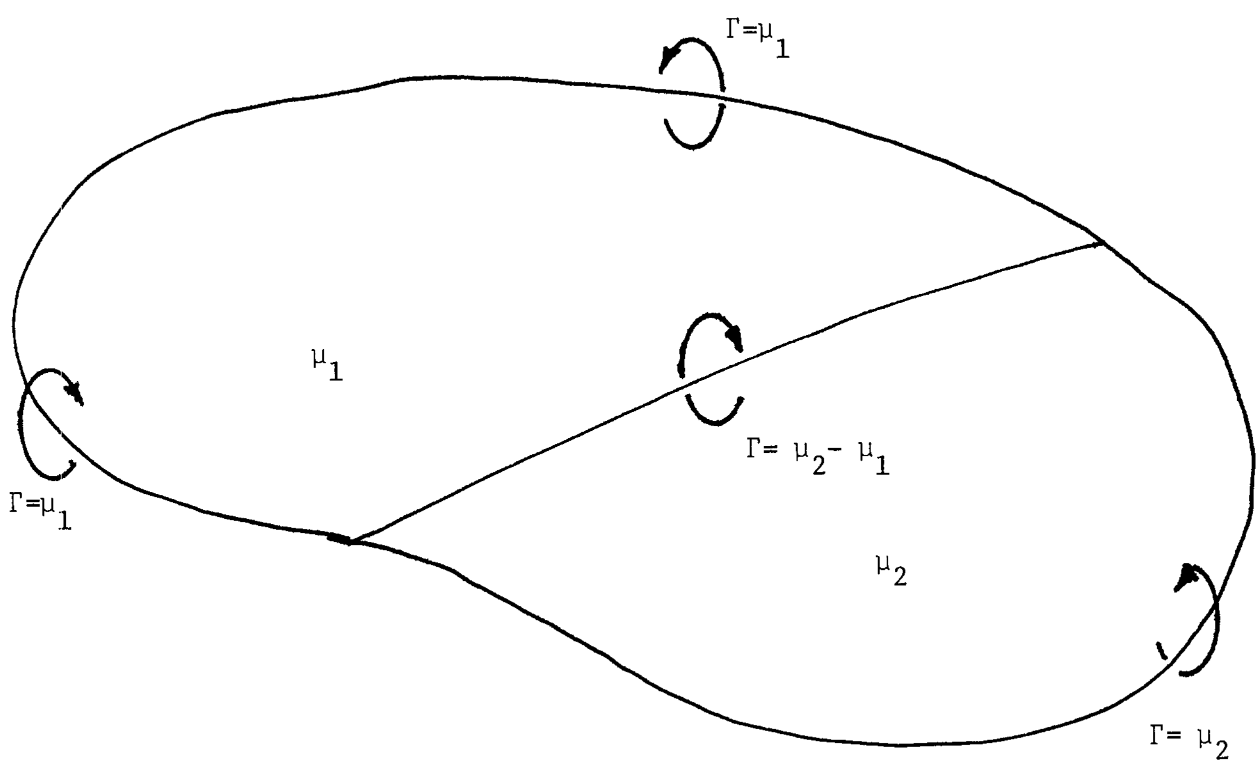

Figure D.4 Vortex Representation of Uniform Strength Doublet Panels

APPENDIX E

EXPERIMENTAL PRESSURE DATA

In this appendix typical plots of pressure data are given. These plots consist of pressure coefficient curves at selected blade positions in the second revolution of the rotor. Data for the three tip-to-windspeed ratios of 2.5, 5.1, and 7.6 are given in Figures E.1, E.2, and E.3 respectively.

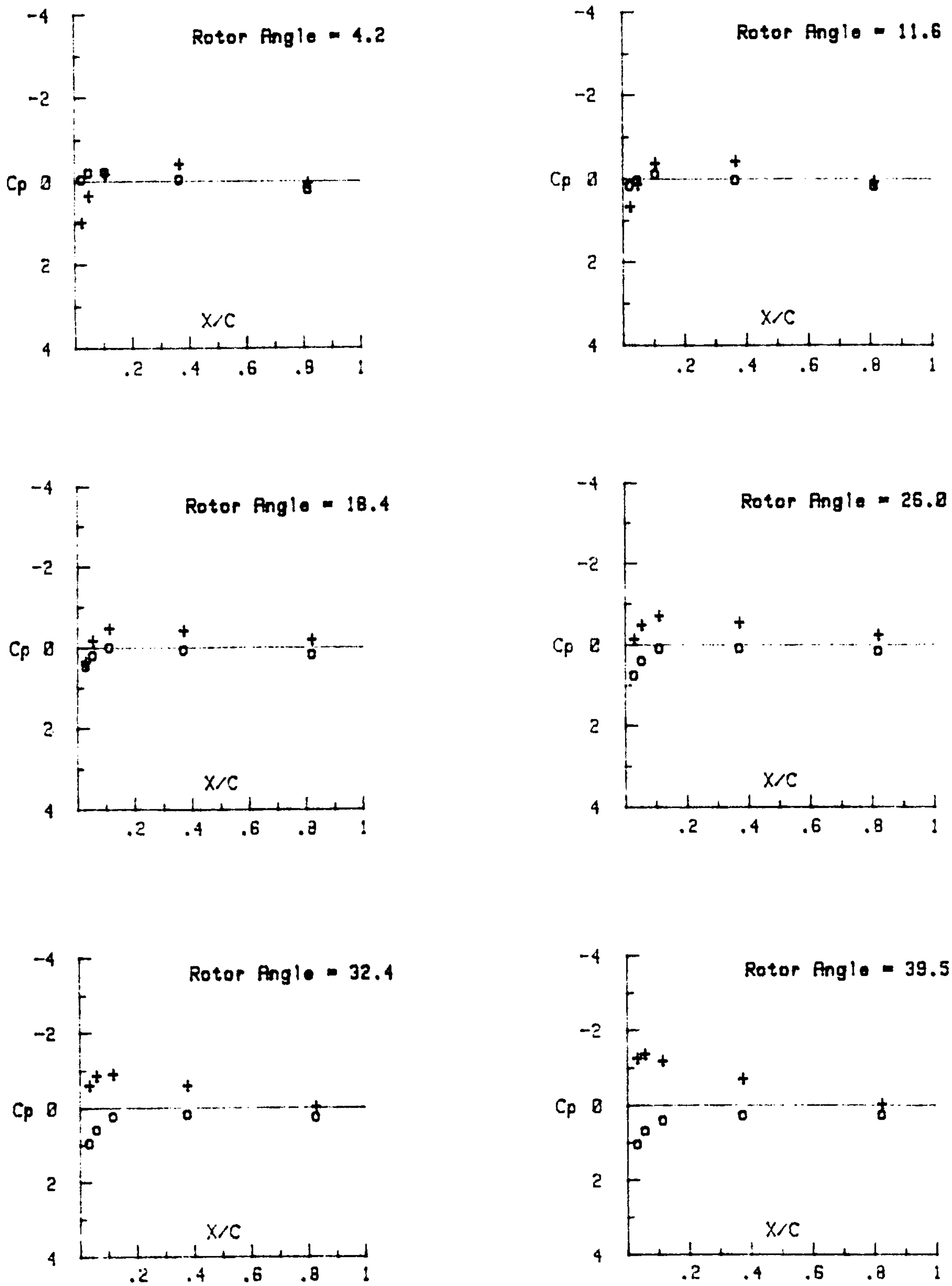

Figure E.1: Effect Of Rotor Angle On C_p Profiles
TSR = 2.5, C/R = 0.25, NB = 1, Outer Surface - ∘, Inner Surface - +

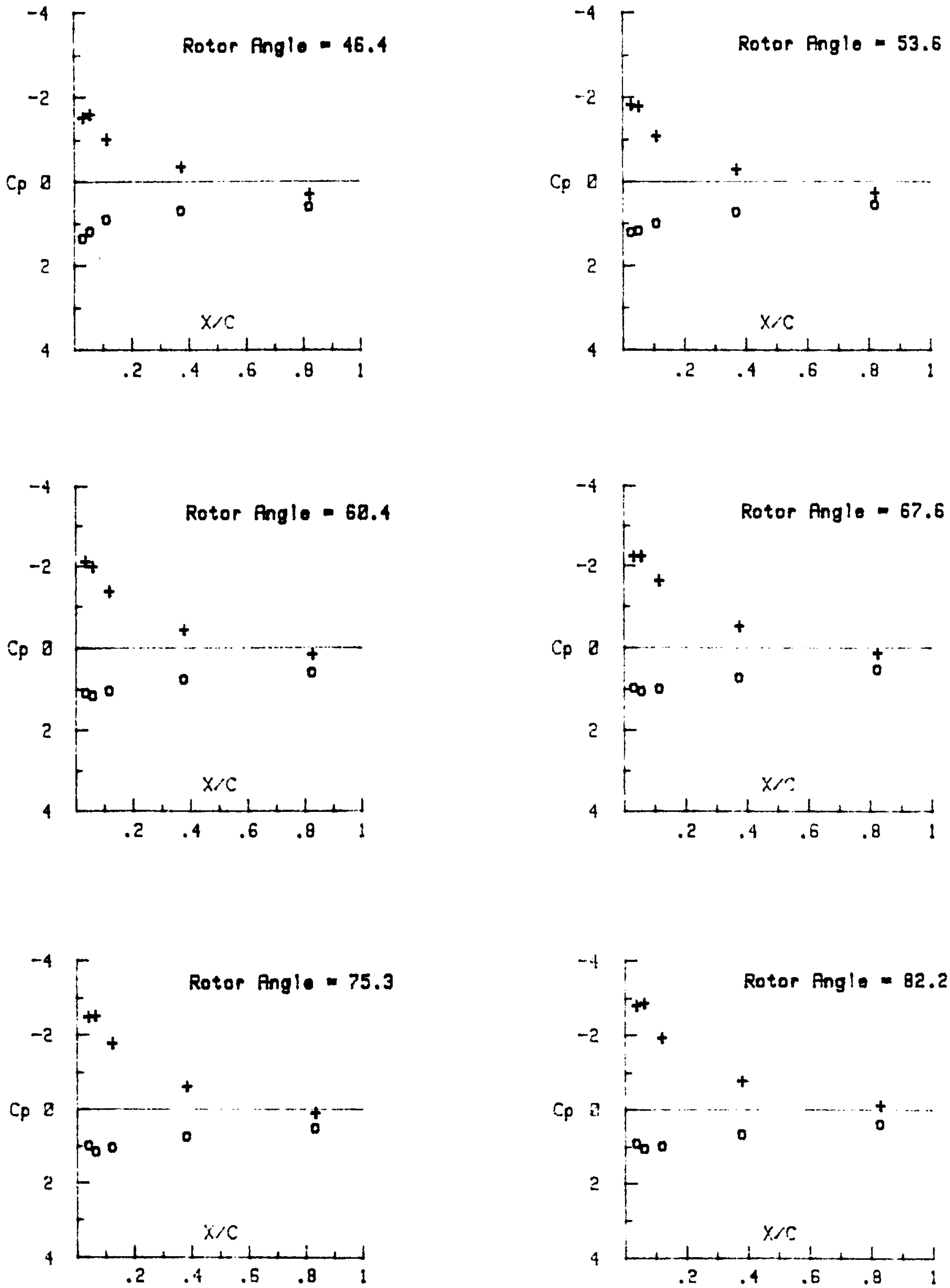

Figure E.1: Continued

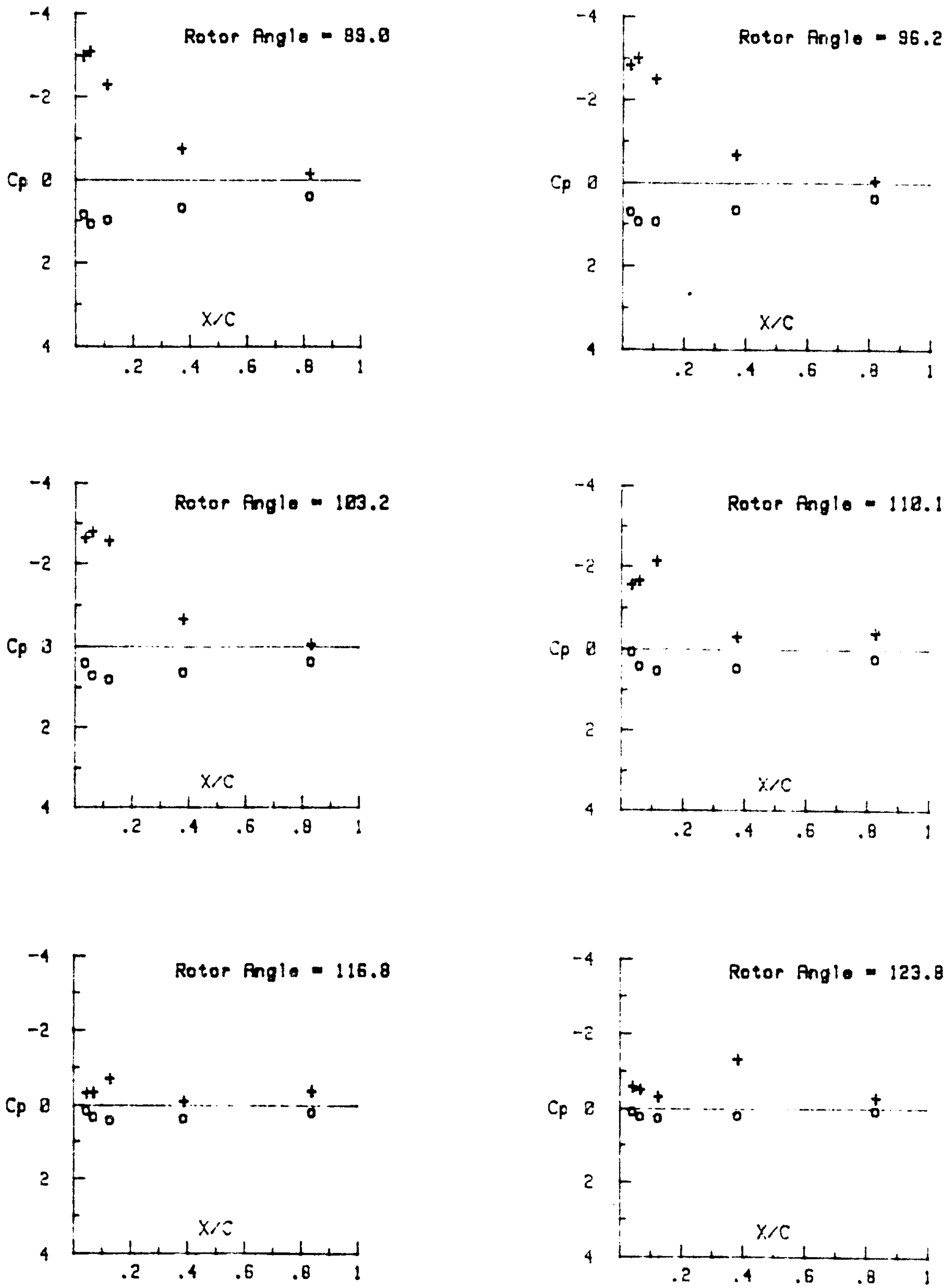

Figure E.1: Continued

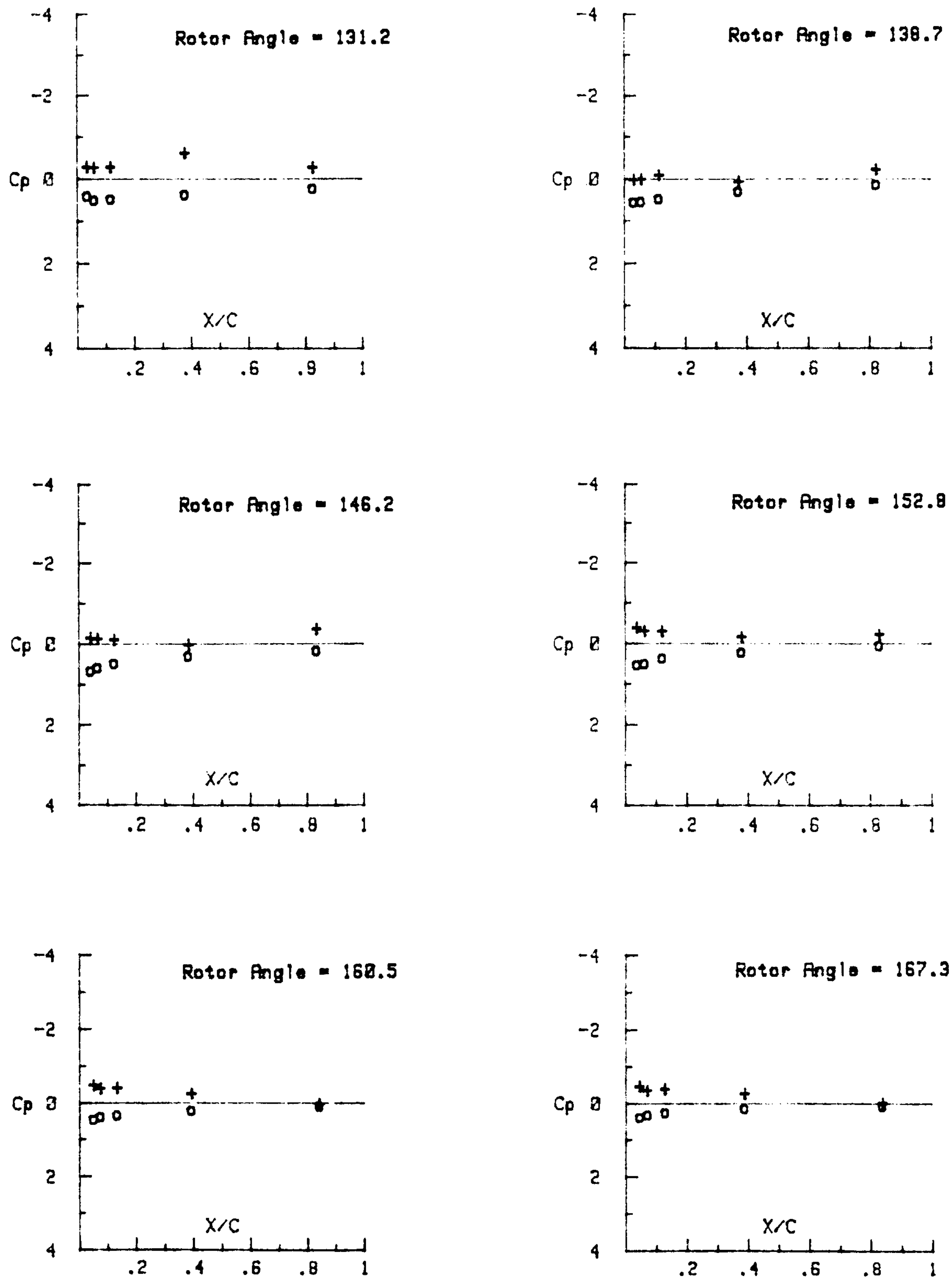

Figure E.1: Continued

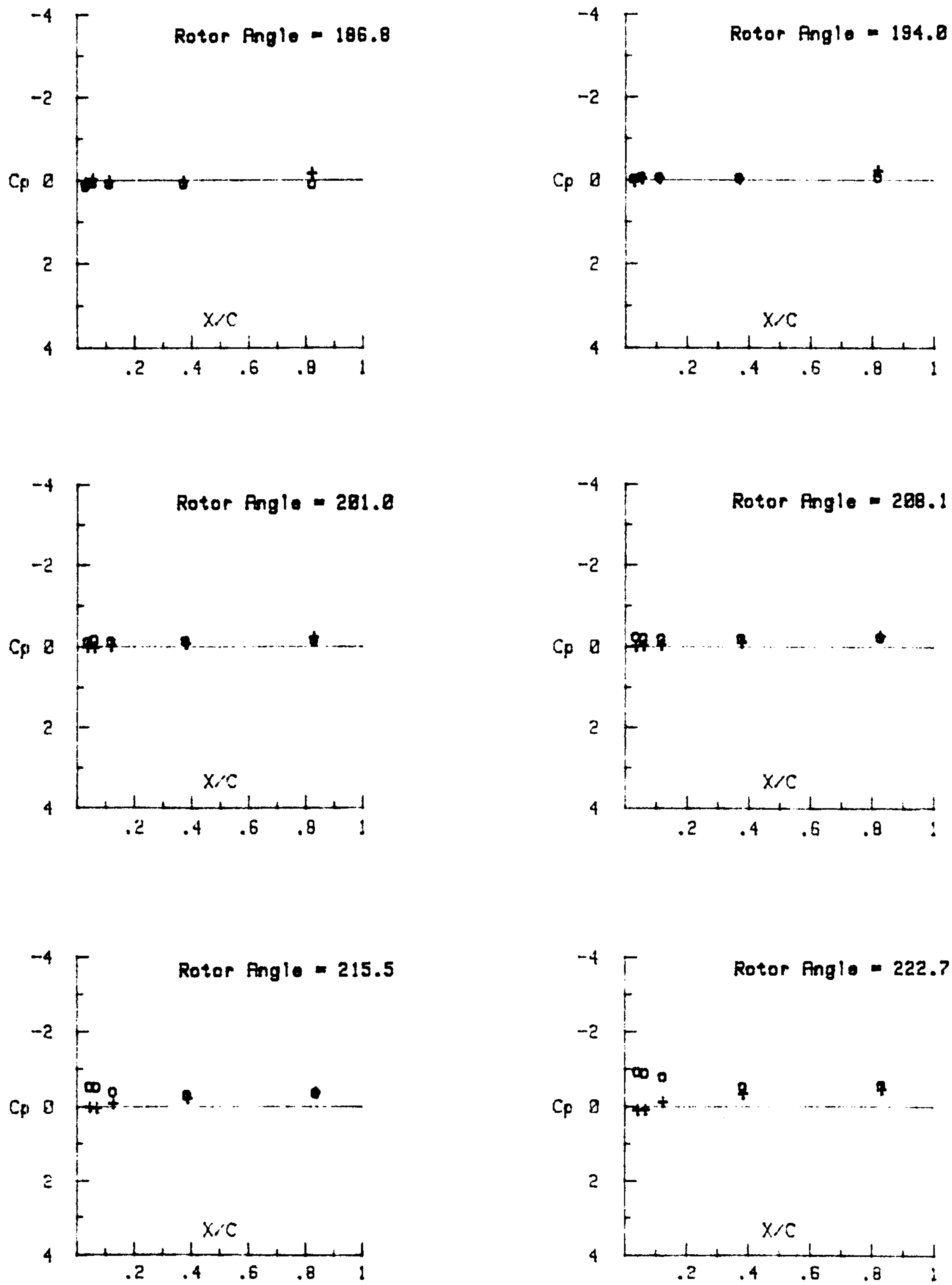

Figure E.1: Continued

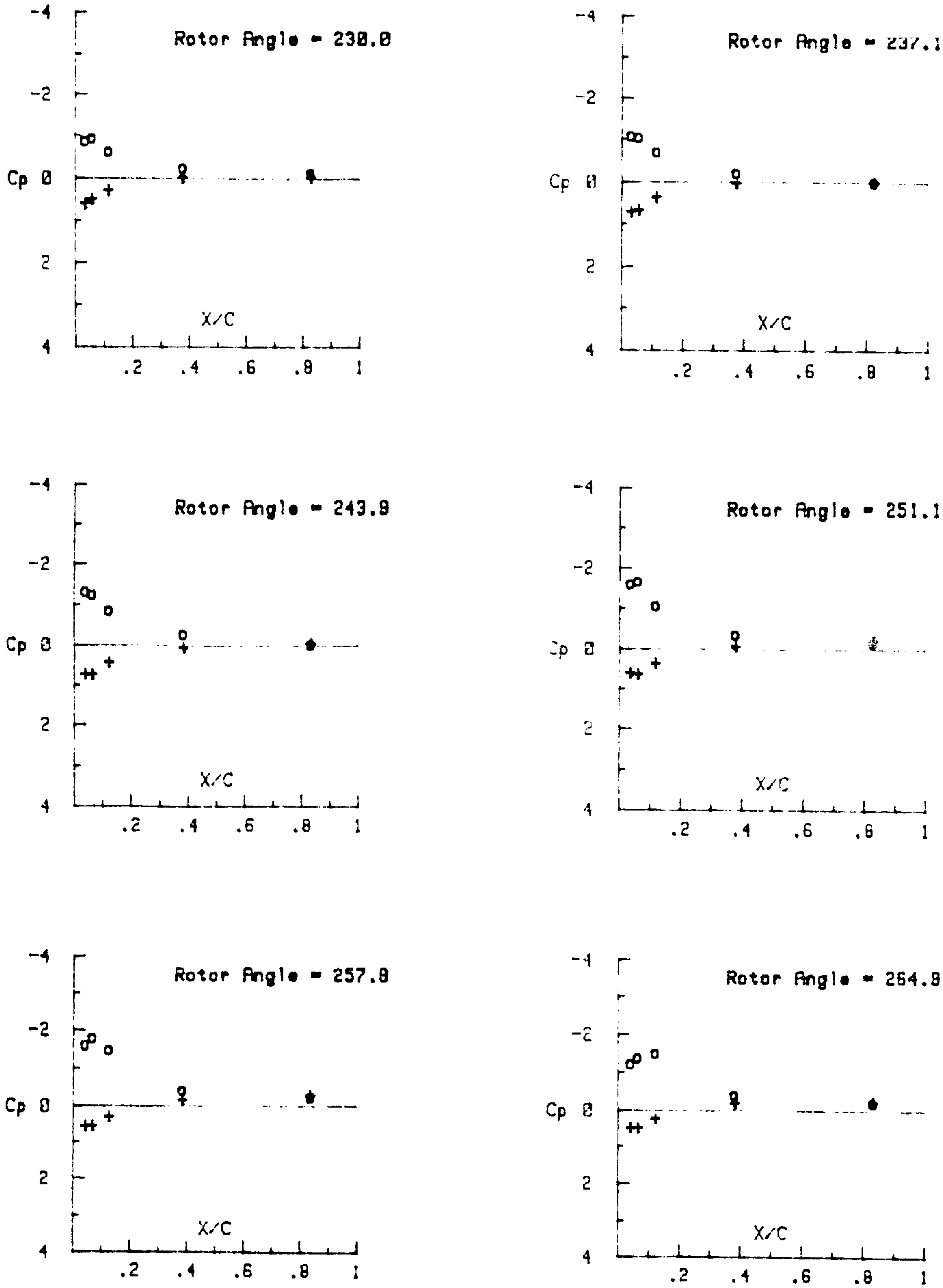

Figure E.1: Continued

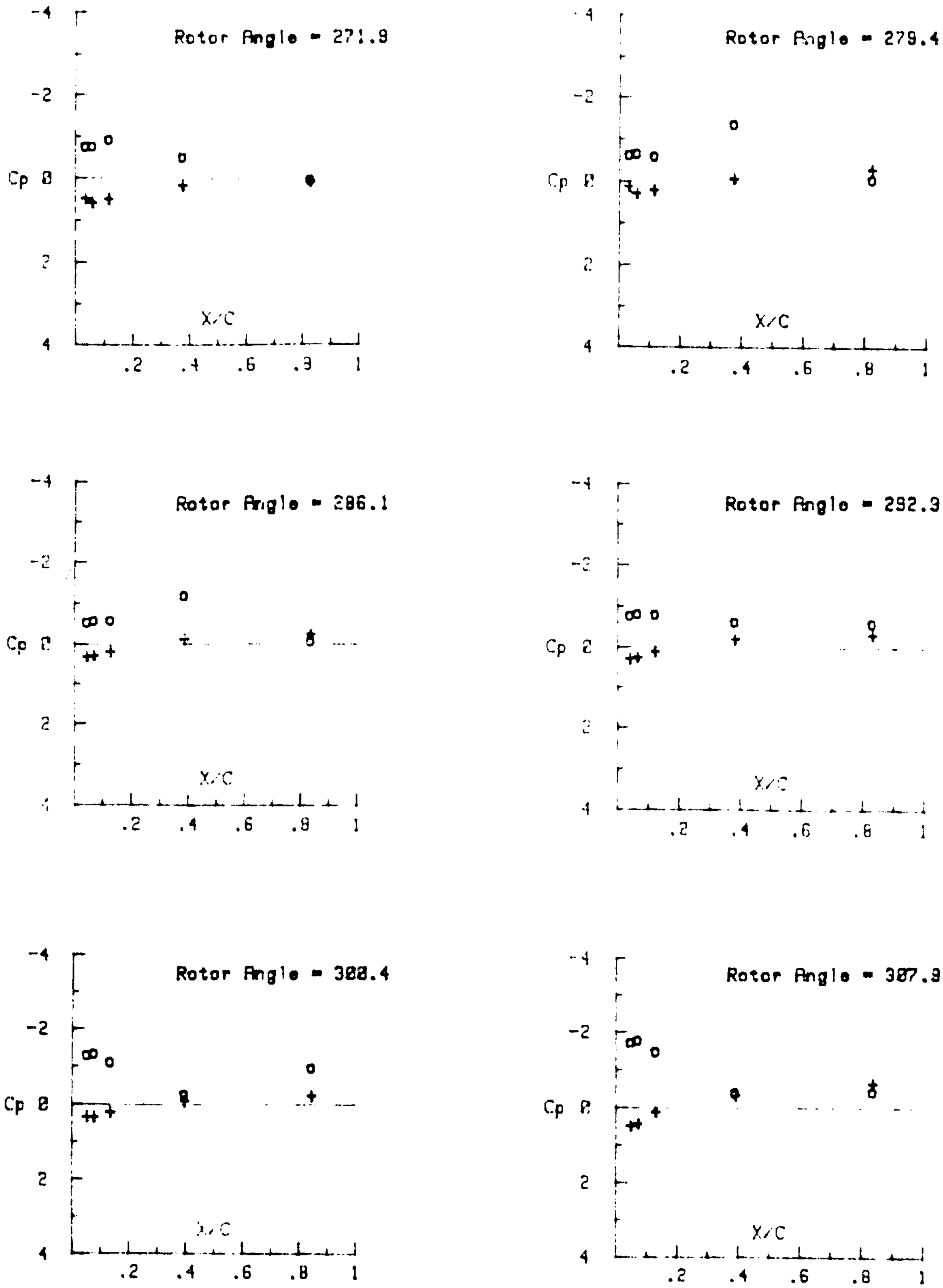

Figure E.1: Continued

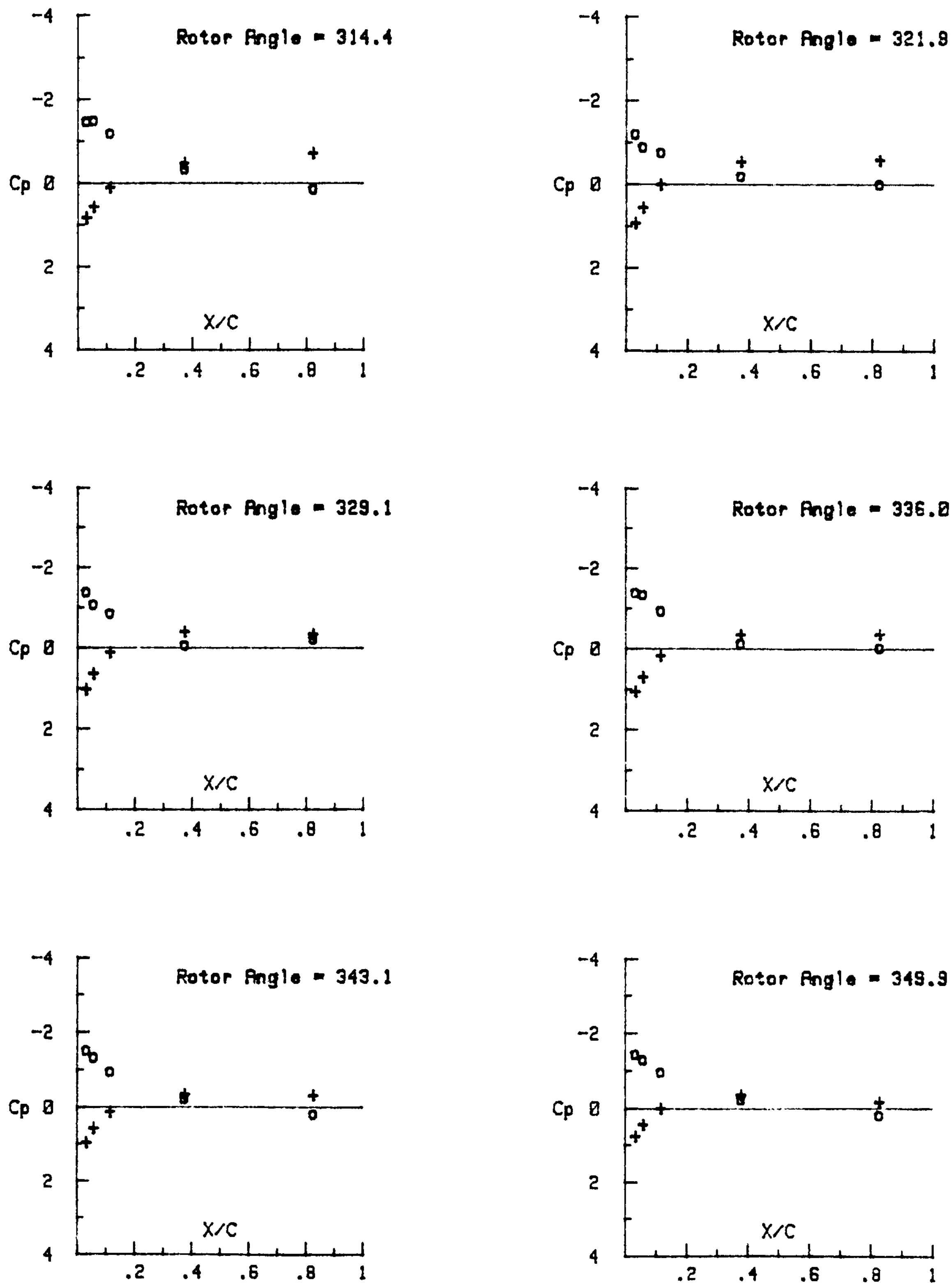

Figure E.1: Continued

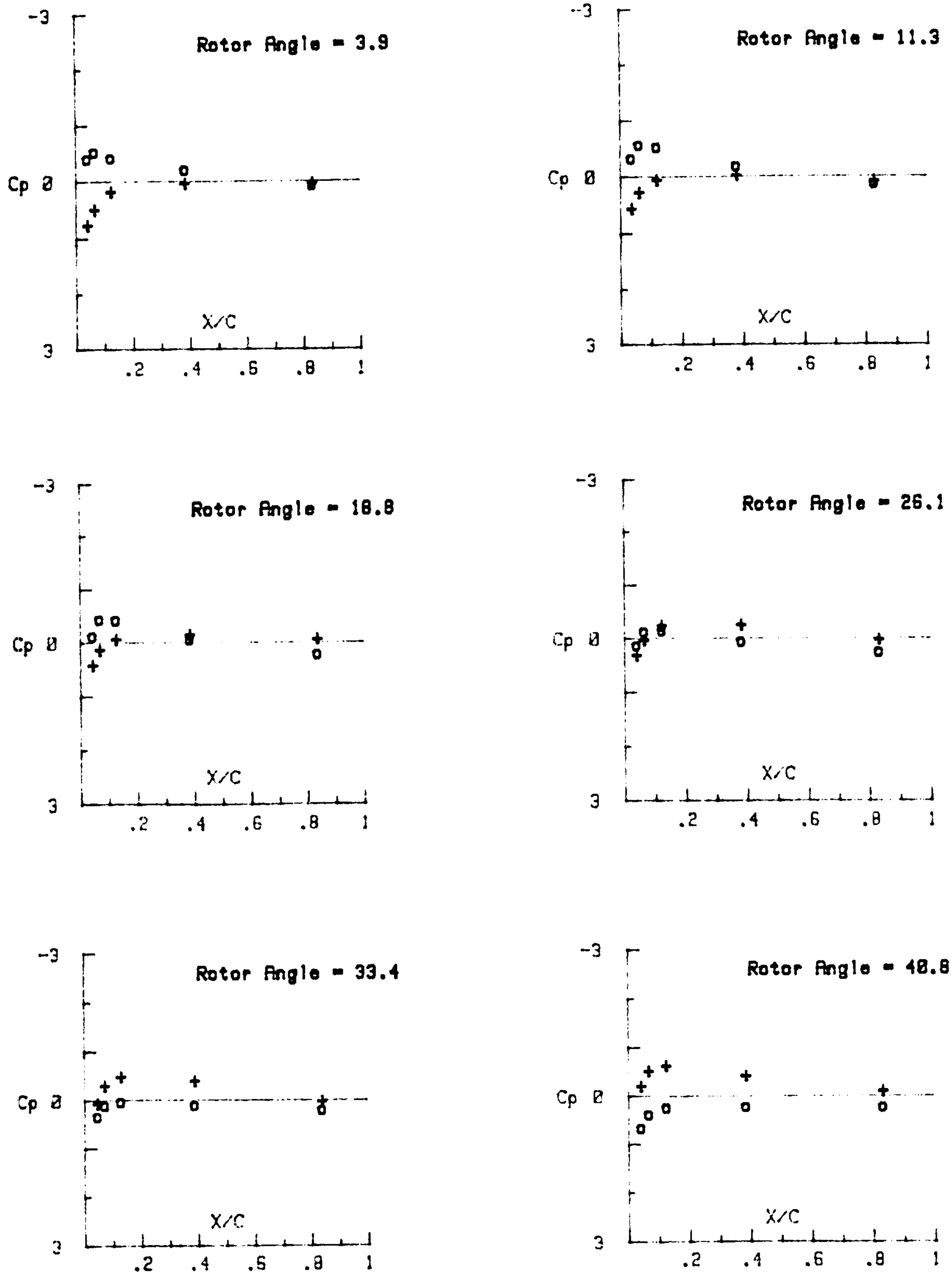

Fig. E.2: Effect of Rotor Angle on C_p Profiles (TSR = 5.1, C/R = 0.25, NB = 1, Outer Surface 0, Inner Surface +)

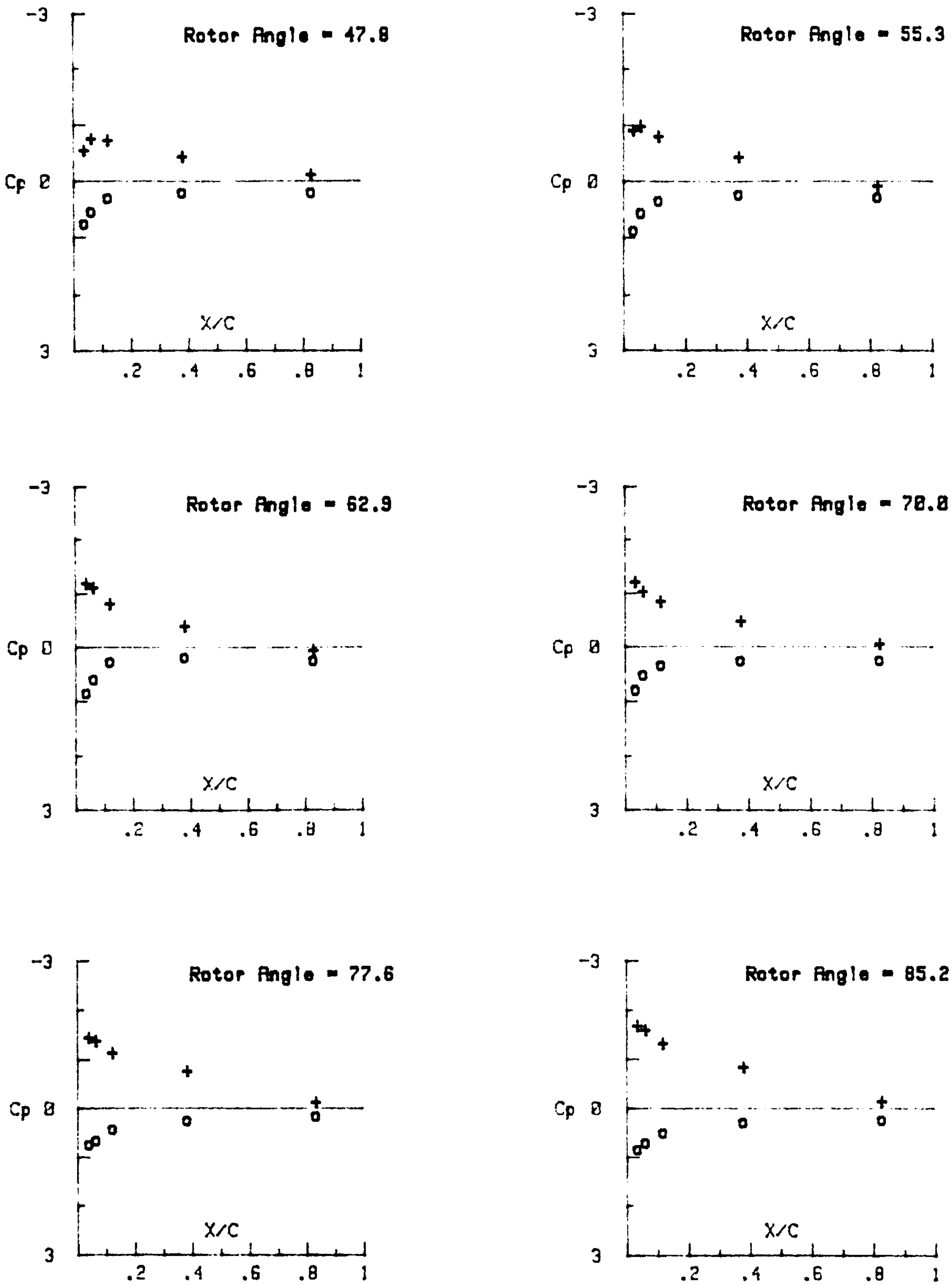

Figure E.2: Continued

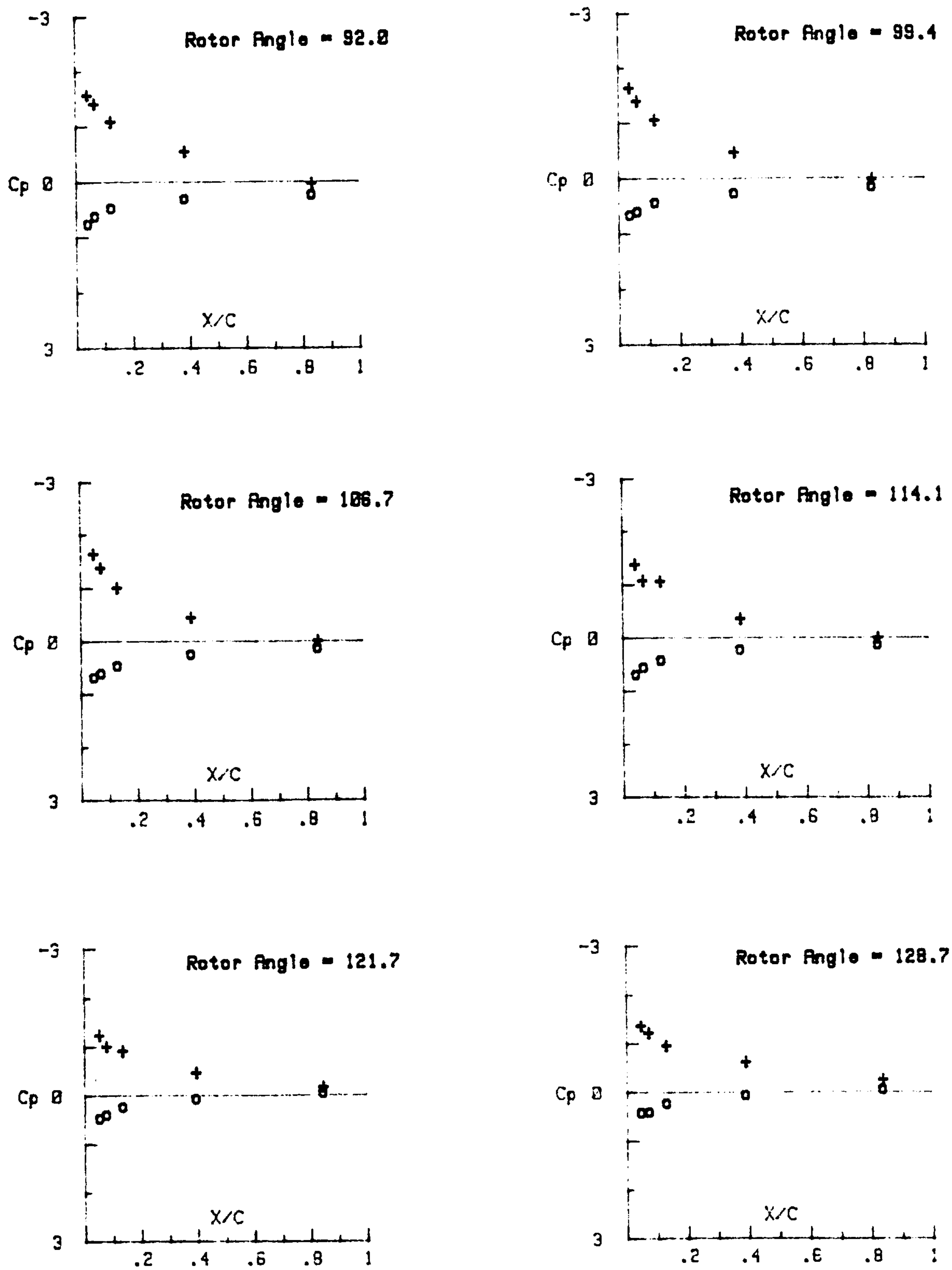

Figure E.2: Continued

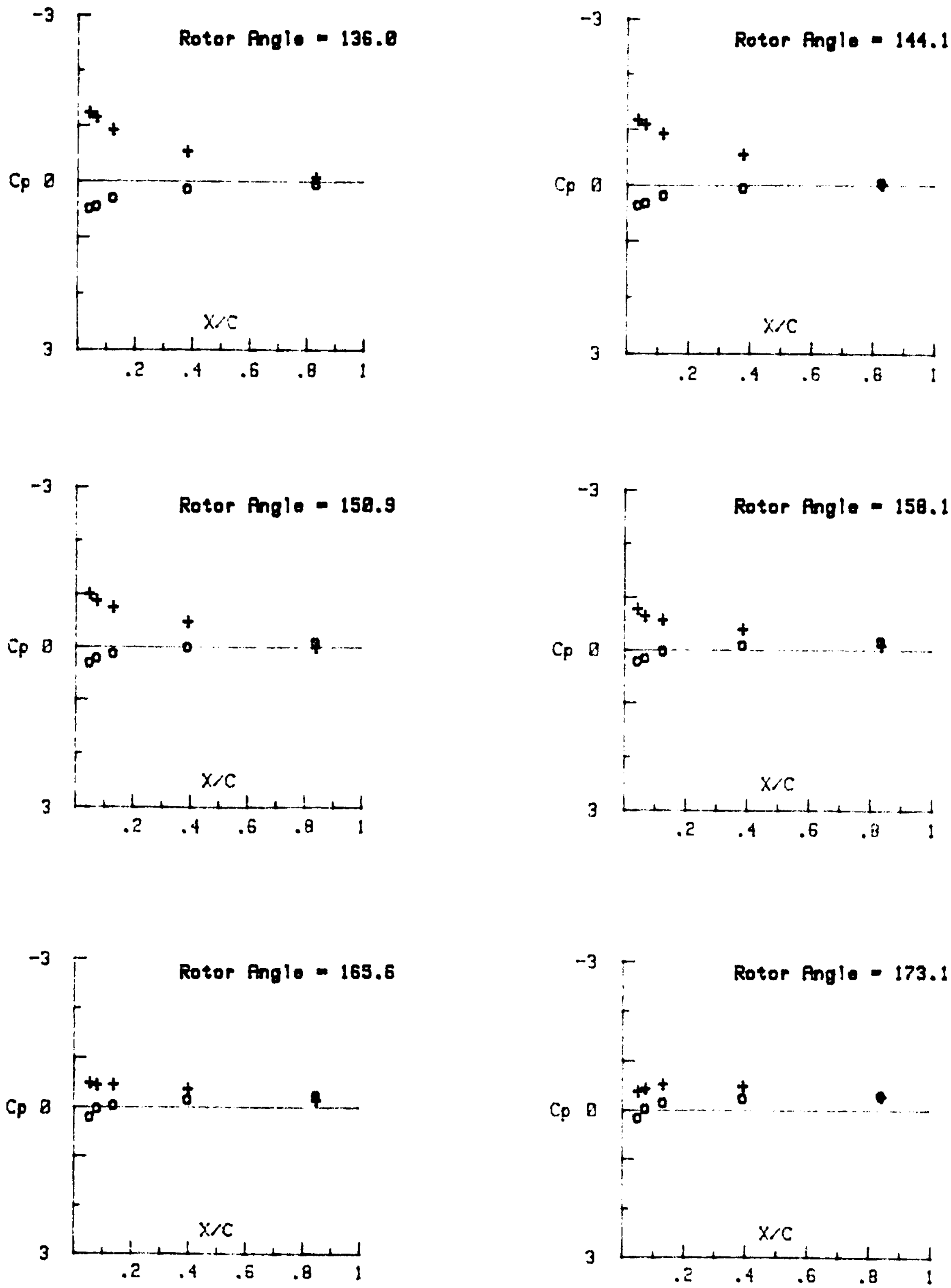

Figure E.2 : Continued

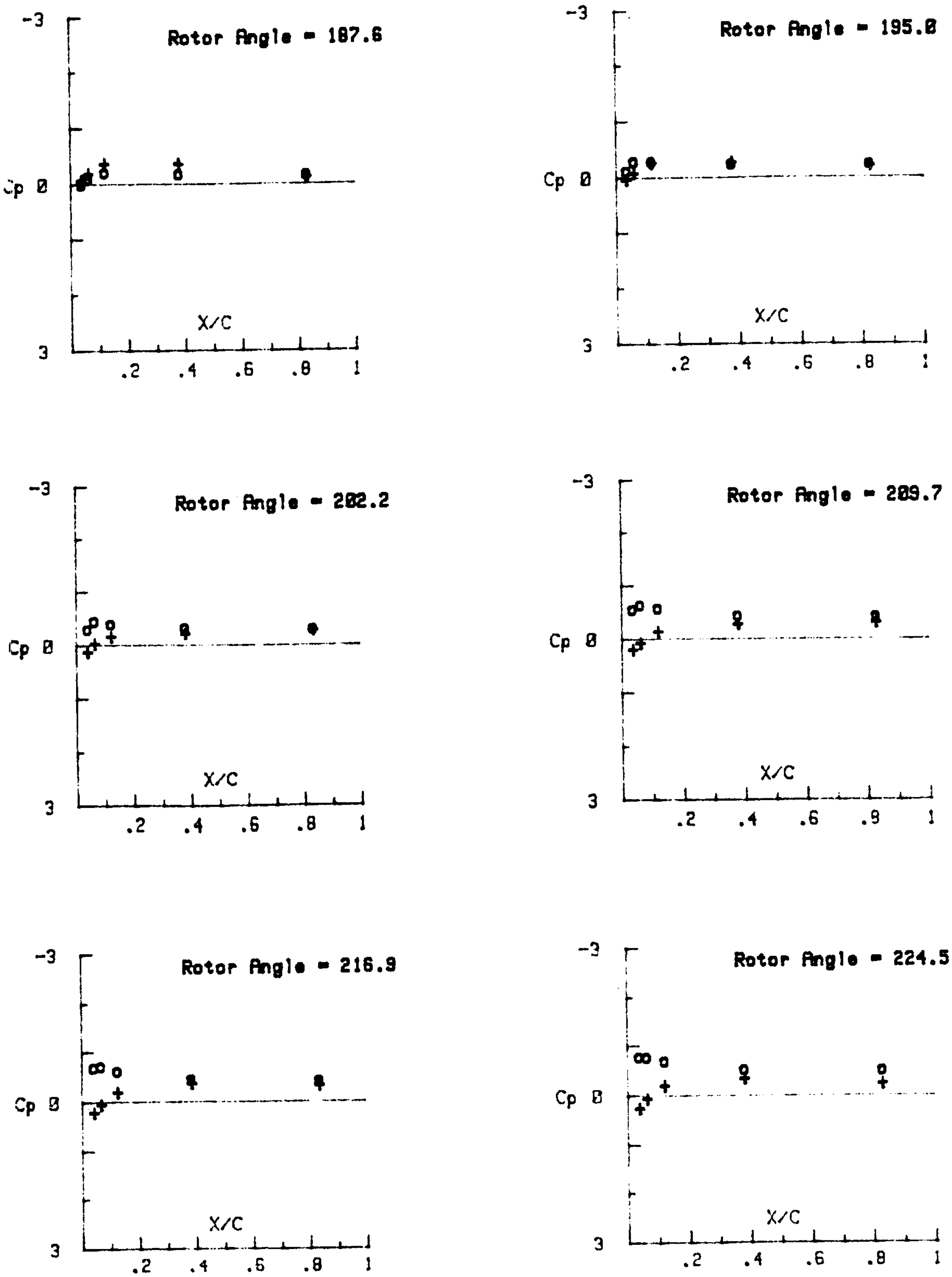

Figure E.2: Continued

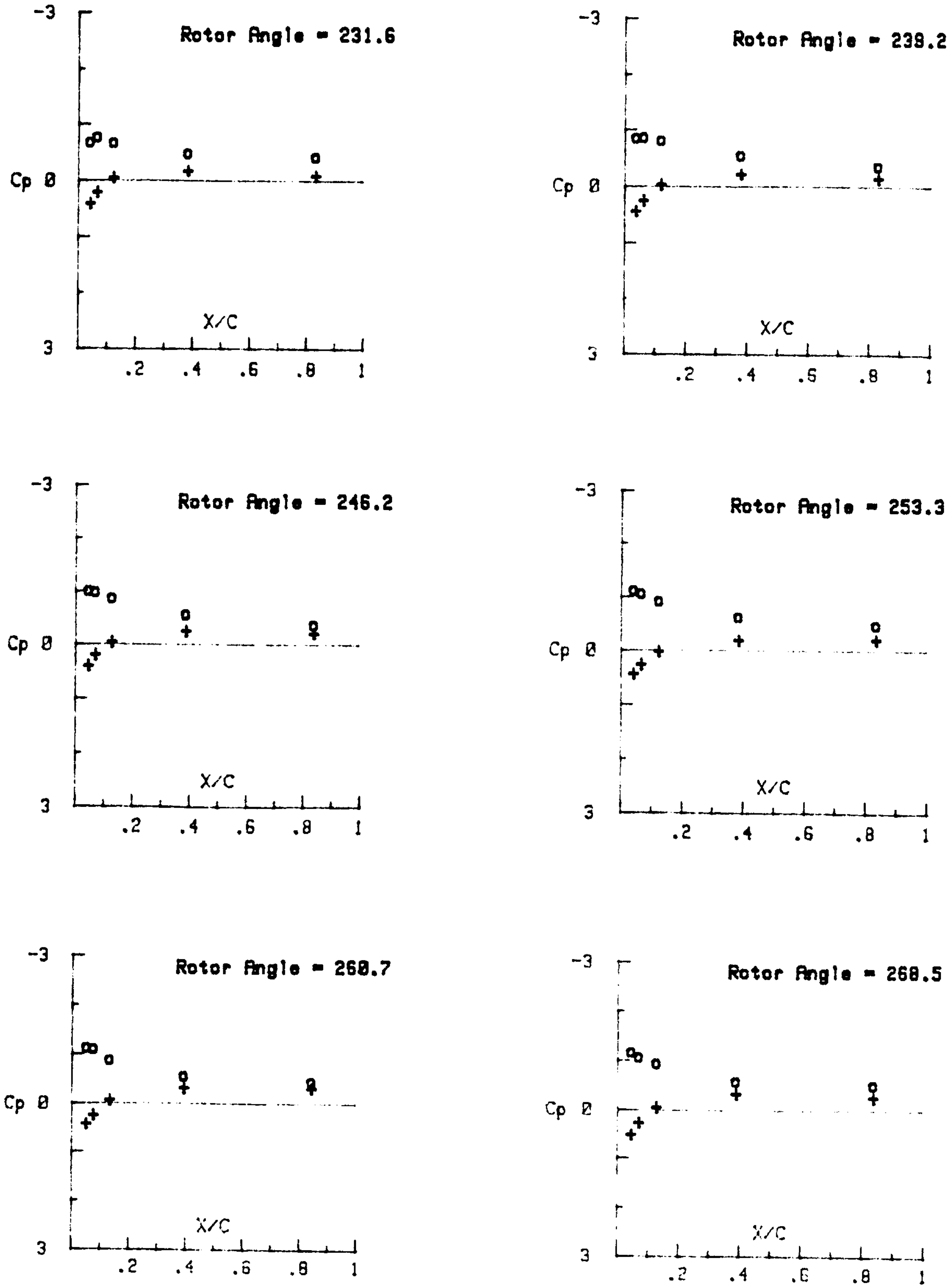

Figure E.2: Continued

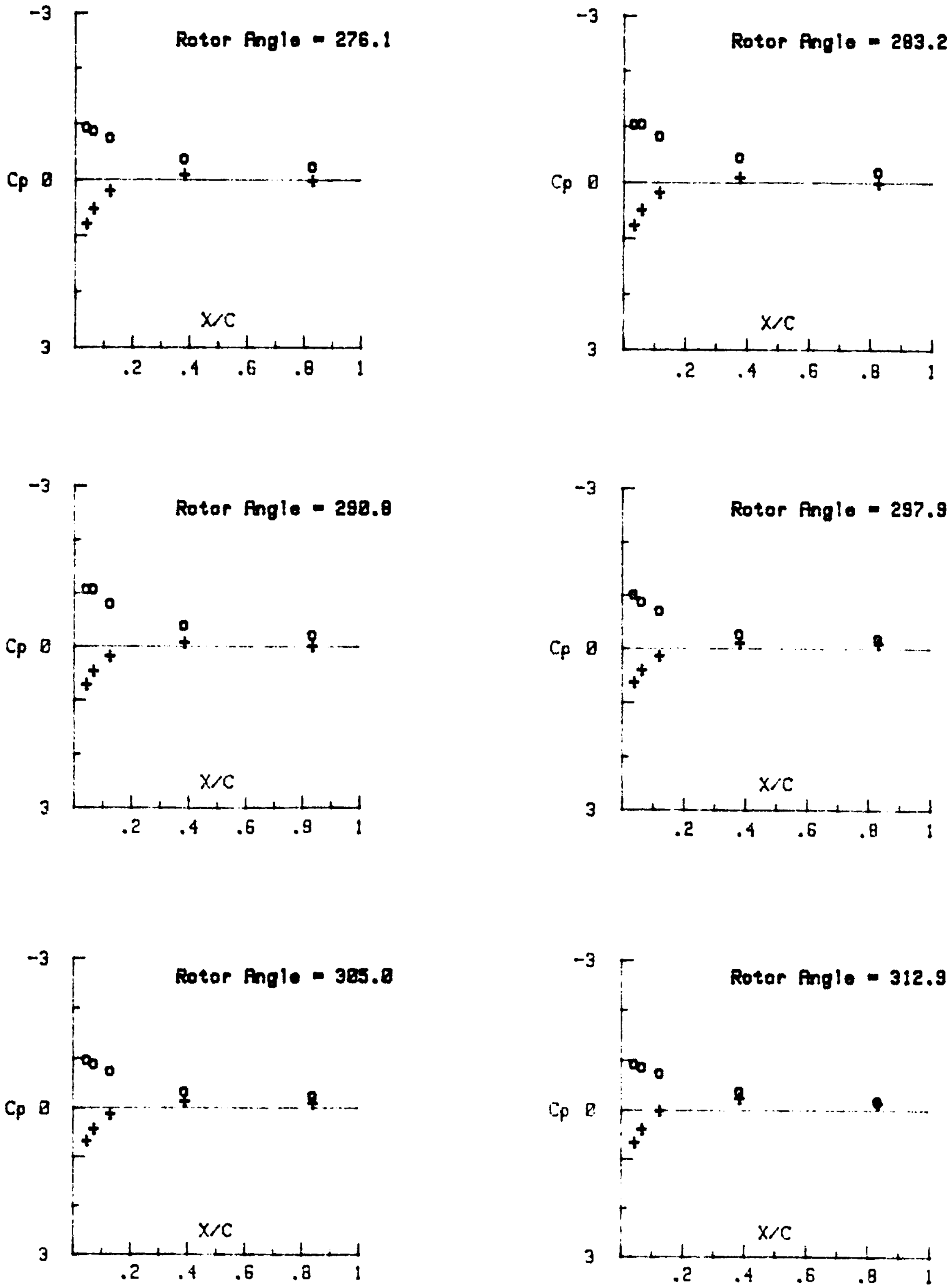

Figure E.2: Continued

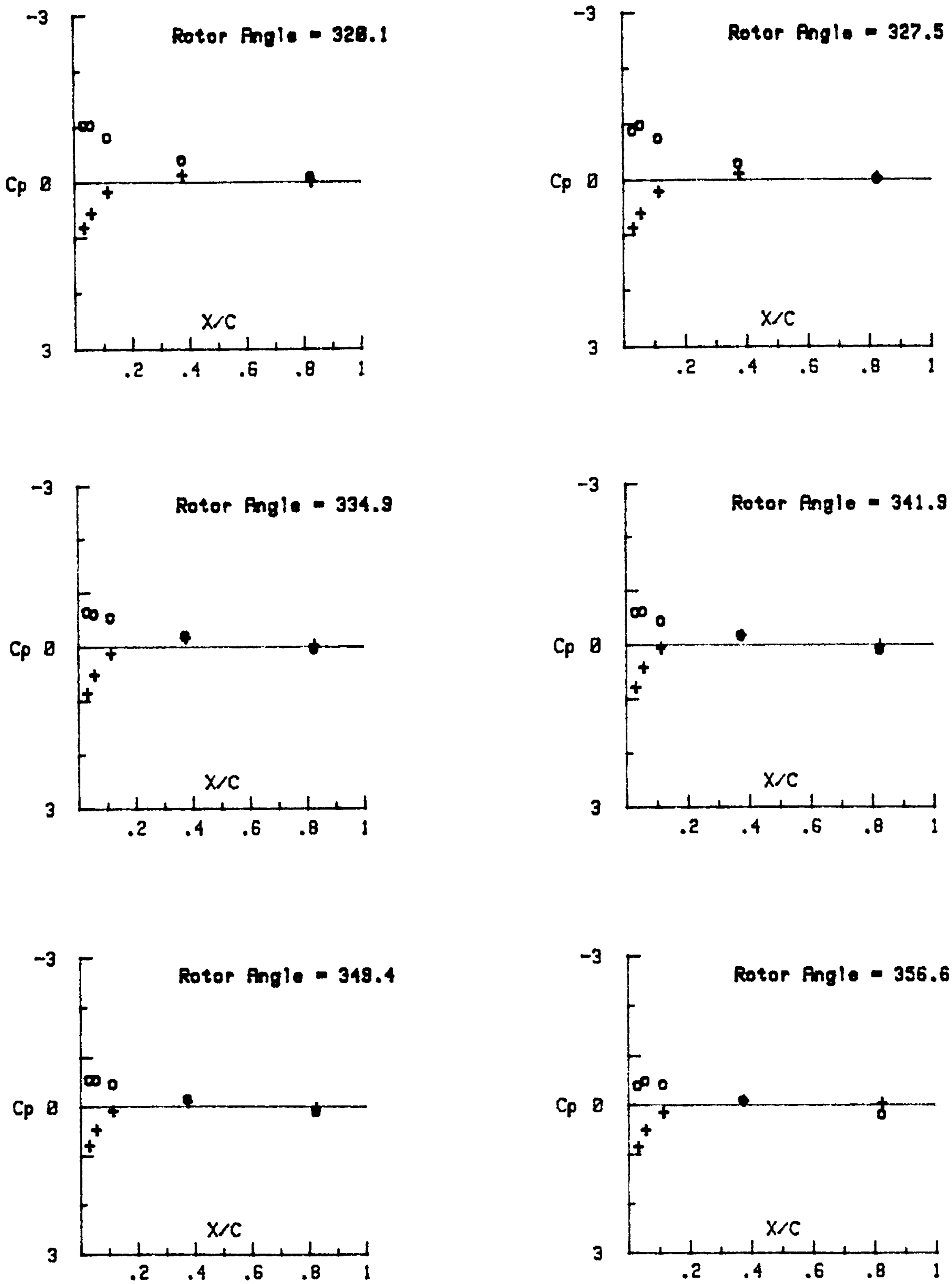

Figure E.2: Continued

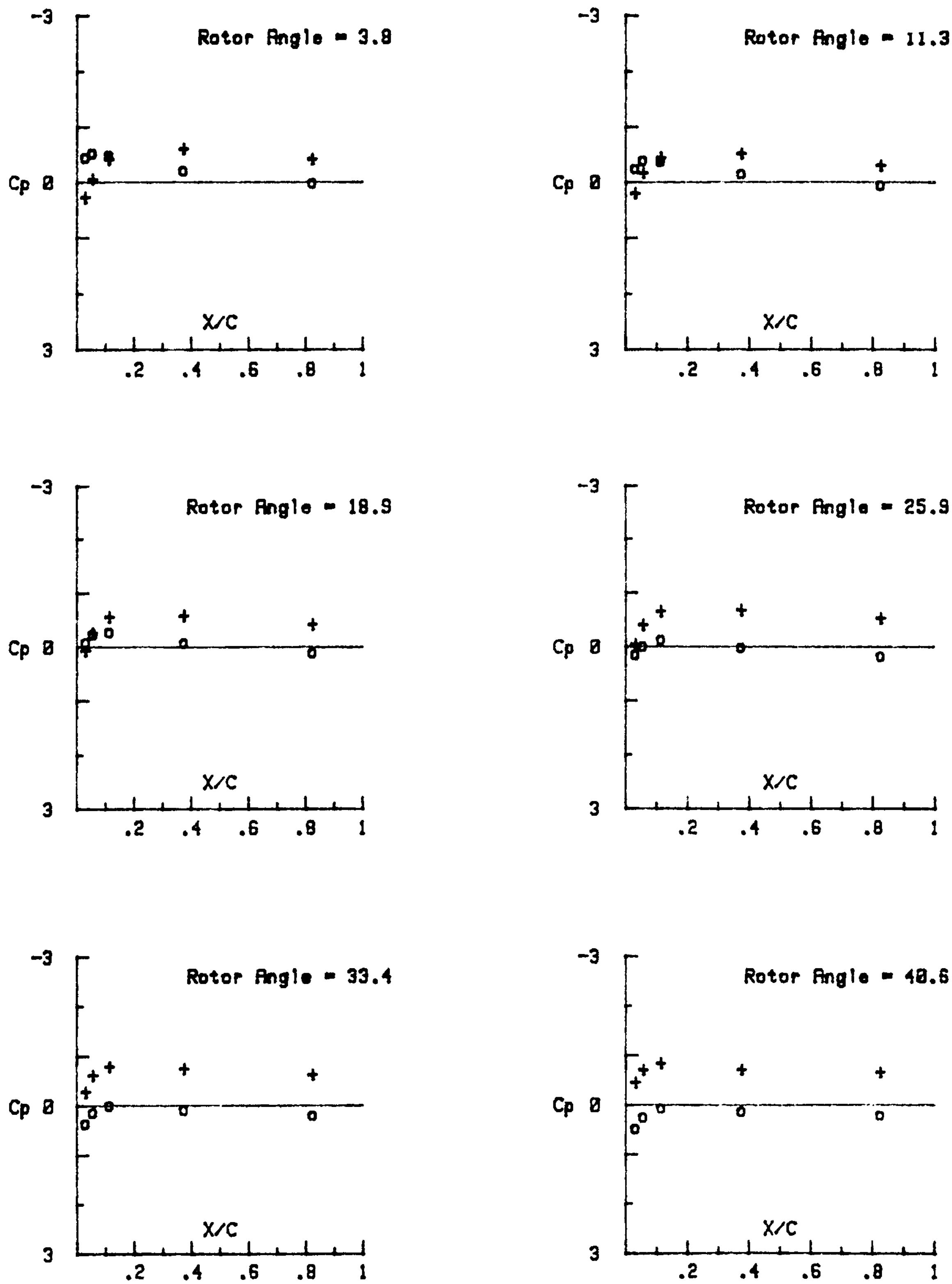

Fig. E.3: Effect of Rotor Angle on C_p Profiles
(TSR = 7.6, C/R = 0.25, NB = 1, Outer Surface 0,
Inner Surface +)

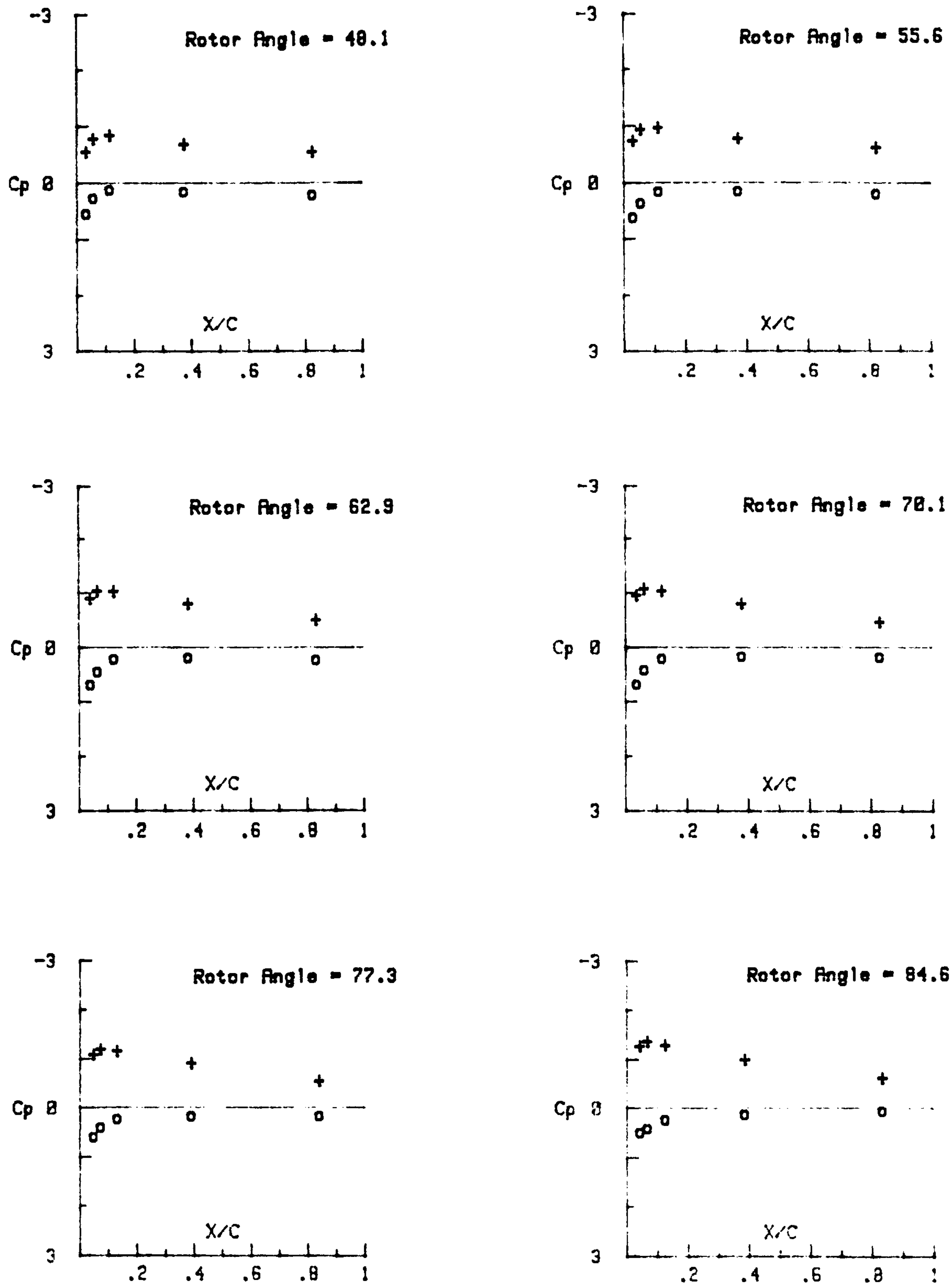

Figure E.3: Continued

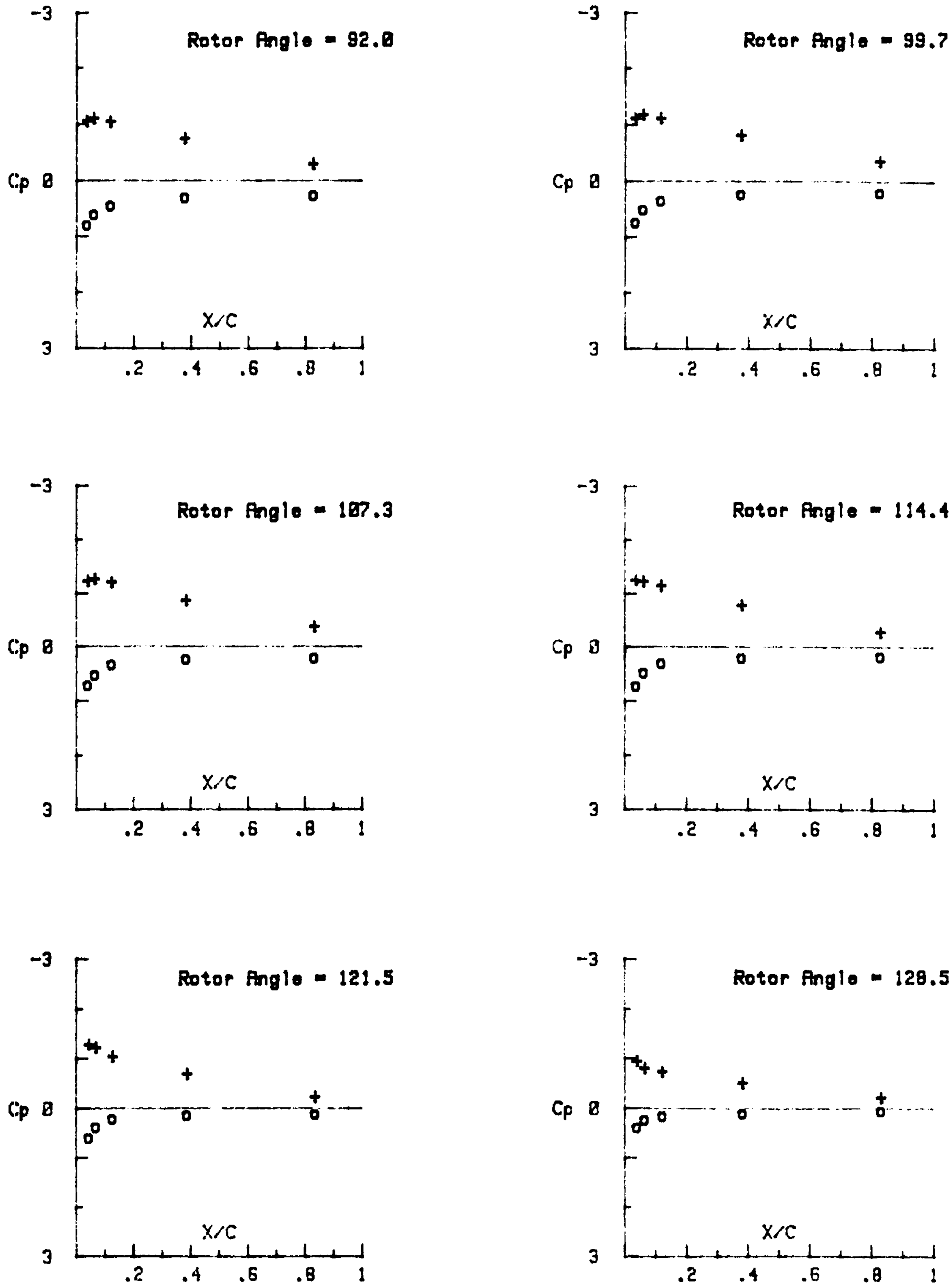

Figure E.3: Continued

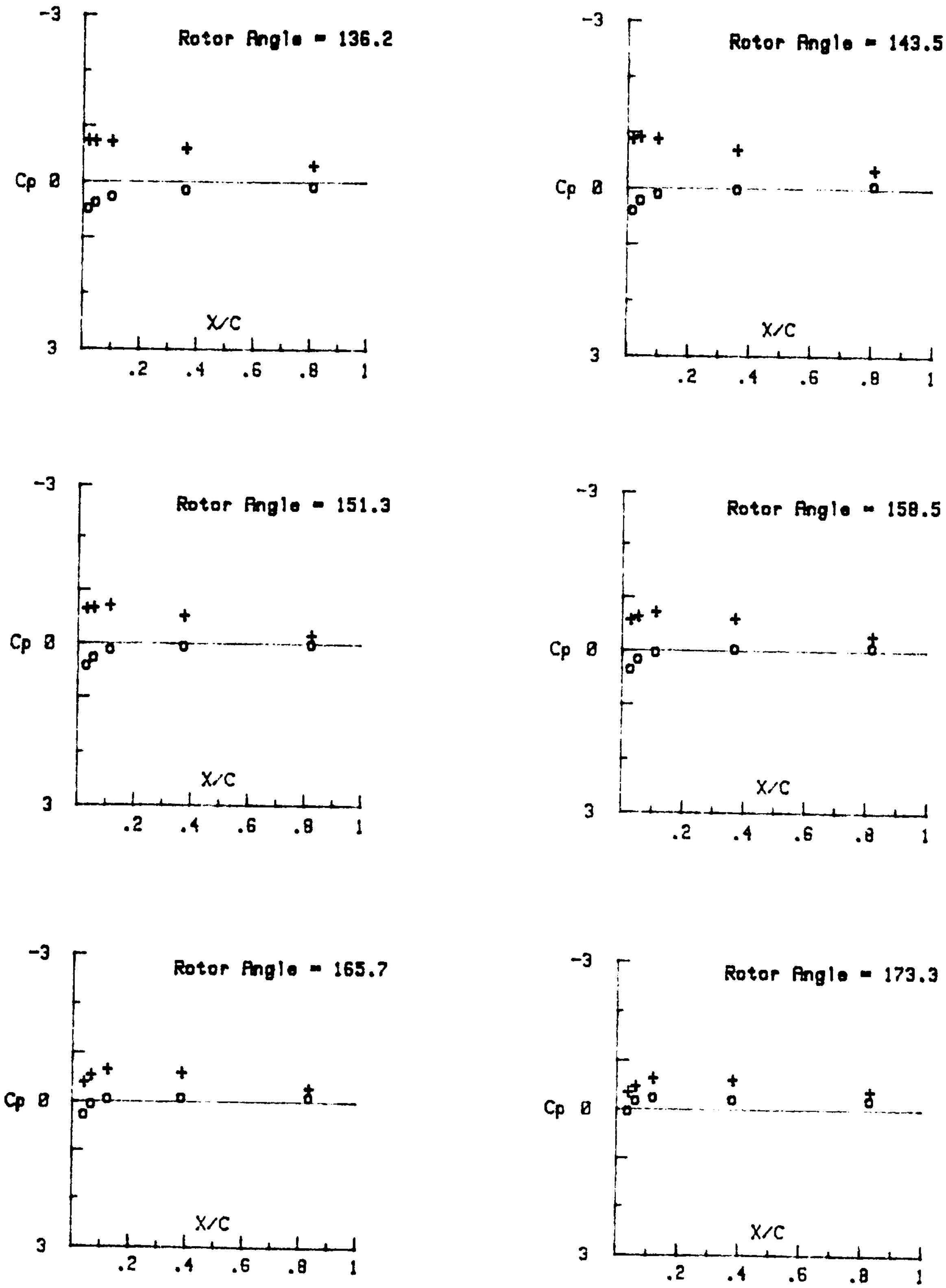

Figure E.3: Continued

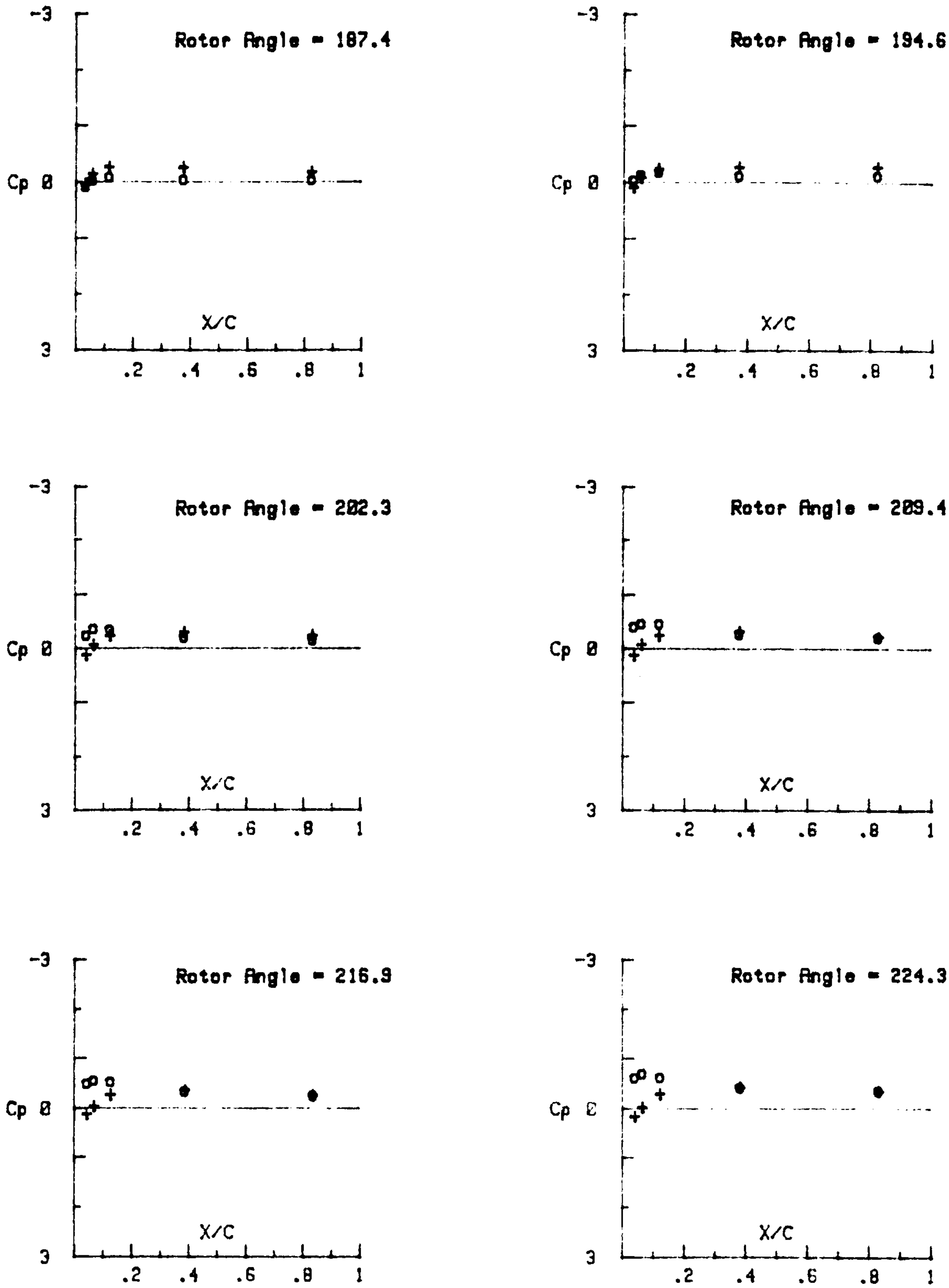

Figure E.3 : Continued

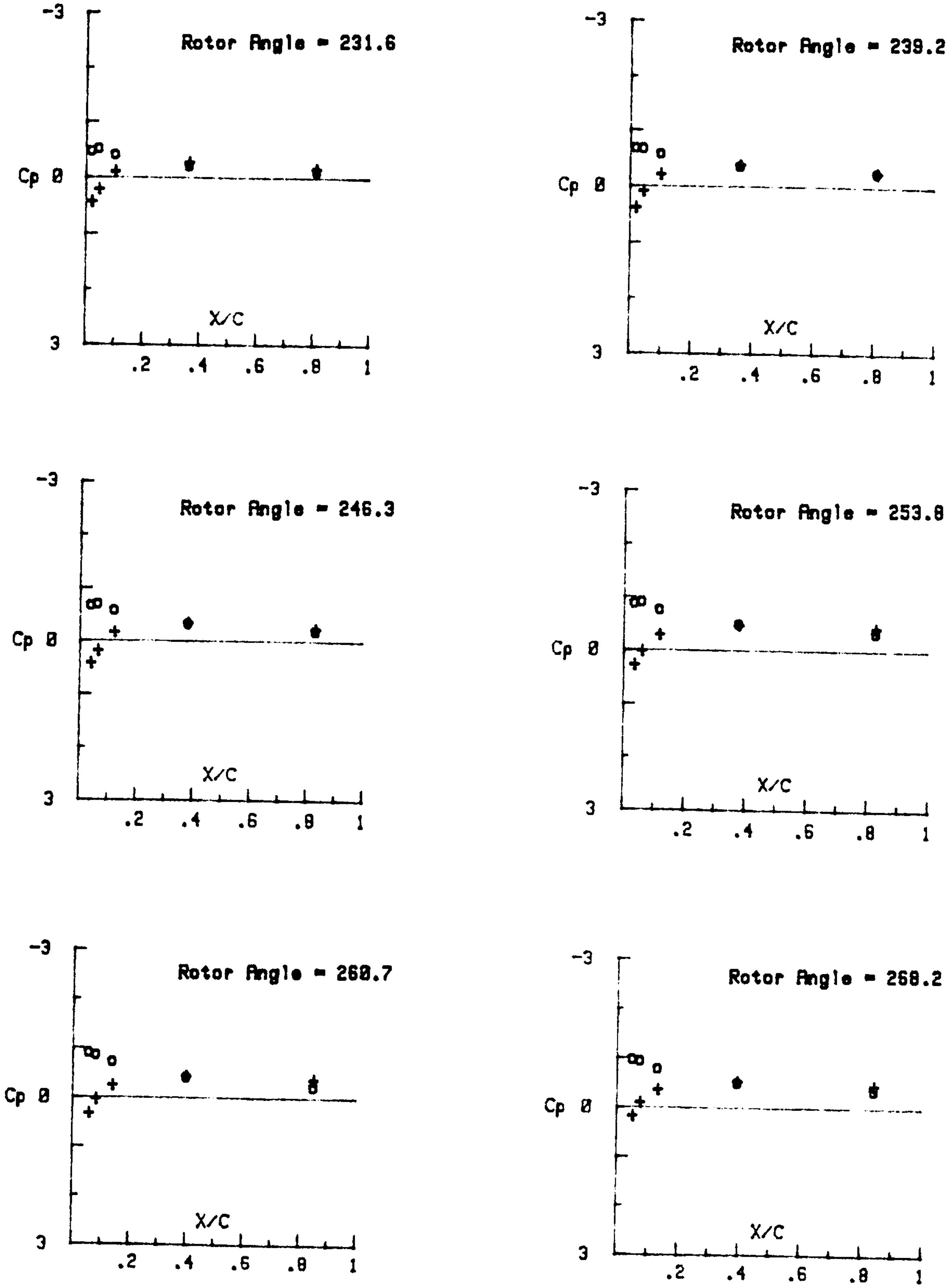

Figure E.3: Continued

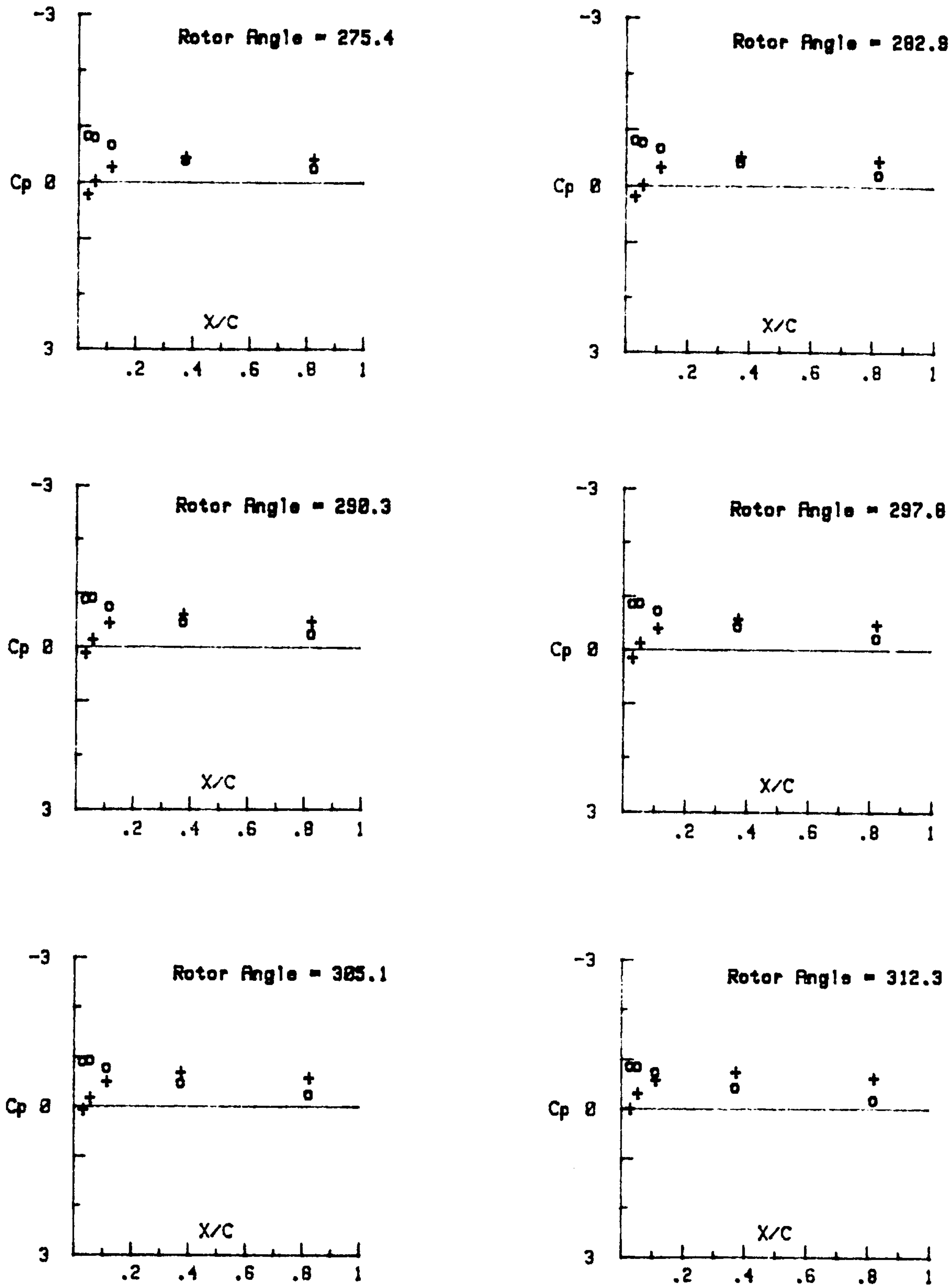

Figure E.3: Continued

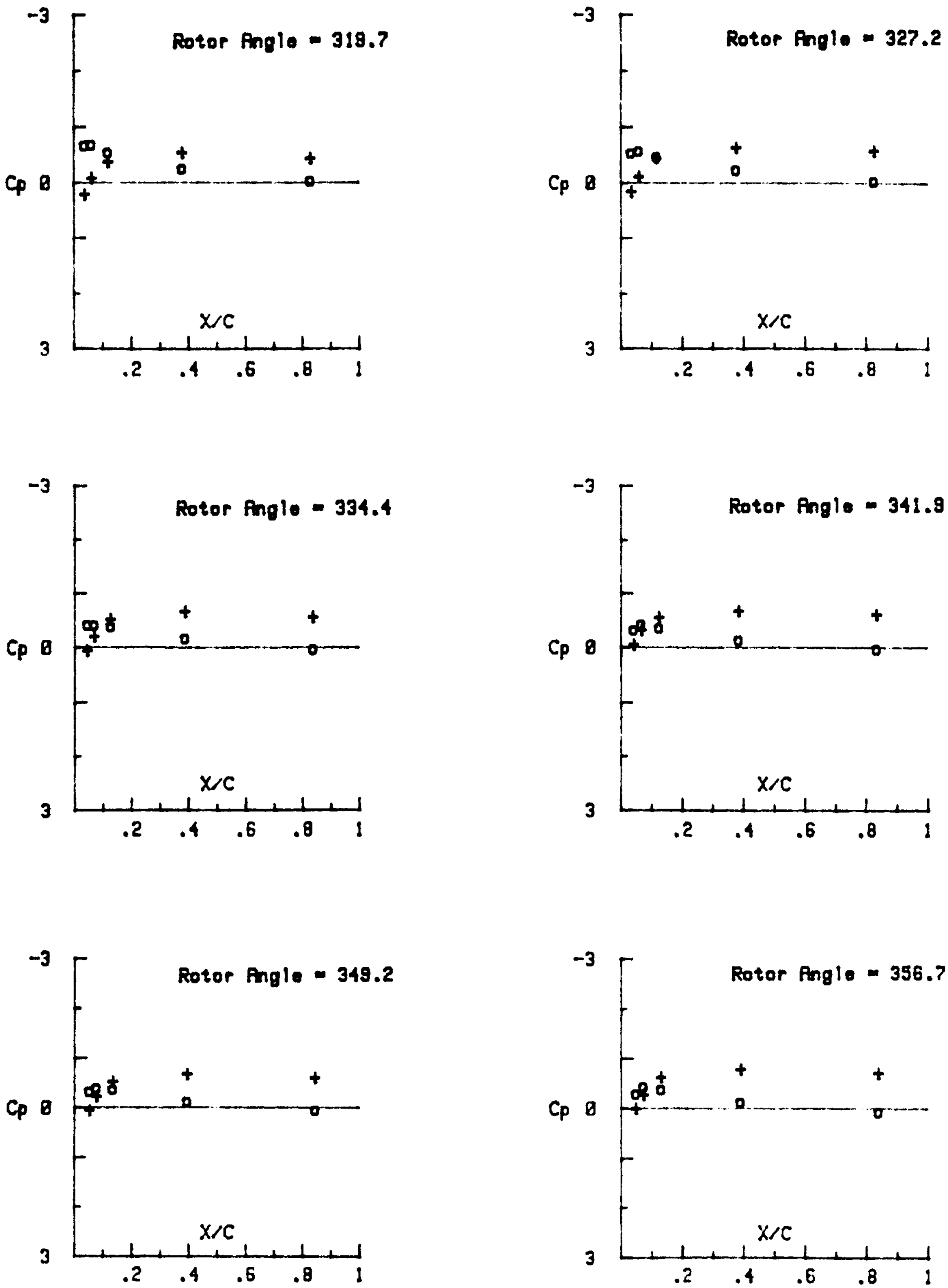

Figure E.3: Continued

DISTRIBUTION:

Aero Engineering Department (2)
Wichita State University
Wichita, KS 67208
Attn: M. Snyder
W. Wentz

Alcoa Laboratories (4)
Alcoa Technical Center
Aluminum Company of America
Alcoa Center, PA 15069
Attn: D. K. Ai
J. T. Huang
J. R. Jombock
J. L. Prohaska

American Wind Energy Association
1609 Connecticut Avenue NW
Washington, DC 20009

E. E. Anderson
South Dakota School of Mines and Technology
Department of Mechanical Engineering
Rapid City, SD 57701

Holt Ashley
Stanford University
Department of Aeronautics and
Astronautics Mechanical Engineering
Stanford, CA 94305

Kevin Austin
Consolidated Edison Company of
New York, Inc.
4 Irving Place
New York, NY 10003

Dr. P. J. Baum
Institute of Geophysics
and Planetary Physics
University of California
Riverside, CA 92521

F. K. Bechtel
Washington State University
Department of Electrical Engineering
College of Engineering
Pullman, WA 99163

M. E. Beecher
Arizona State University
University Library
Tempe, AZ 85281

K. Bergey
University of Oklahoma
Aero Engineering Department
Norman, OK 73069

R. K. Berky
Alco Energy, Inc.
8002 Lee Blvd.
Leawood, KS 66208

Steve Blake
Wind Energy Systems
Route 1, Box 93-A
Oskaloosa, KS 66066

N. Butler
Bonneville Power Administration
P.O. Box 3621
Portland, OR 97225

R. Camerero
Faculty of Applied Science
University of Sherbrooke
Sherbrooke, Quebec
CANADA J1K 2R1

Professor V. A. L. Chasteau
School of Engineering
University of Auckland
Private Bag
Auckland, NEW ZEALAND

Dr. R. N. Clark
USDA, Agricultural Research Service
Southwest Great Plains Research Center
Bushland, TX 79012

Dr. D. E. Cromack
Mechanical and Aerospace Engineering Department
University of Massachusetts
Amherst, MA 01003

Gale B. Curtis
Curtis Associates
3089 Oro Blanco Drive
Colorado Springs, CO 80917

DOE/ALO (2)
Albuquerque, NM 87115
Attn: G. P. Tennyson

DOE Headquarters/Wind Energy Technology Division (20)
1000 Independence Avenue
Washington, DC 20585
Attn: L. V. Divone
P. Goldman

C. W. Dodd
School of Engineering
Southern Illinois University
Carbondale, IL 62901

D. D. Doerr
Kaiser Aluminum and Chemical Sales, Inc.
6177 Sunol Blvd.
P.O. Box 877
Pleasonton, CA 94566

Dominion Aluminum Fabricating, Ltd. (2)
3570 Hawkestone Road
Mississauga, Ontario
CANADA L5C 2V8
Attn: L. Schienbein
C. Wood

J. B. Dragt
Nederlands Energy Research Foundation (E.C.N.)
Physics Department
Westerduinweg 3 Patten (nh)
THE NETHERLANDS

Alfred J. Eggers, Jr.
Chairman of the Board
RANN, Inc.
260 Sheridan Ave., Ste. 414
Palo Alto, CA 94306

D. W. Dunham
Commonwealth Electric Co.
Box 368
Vineyard Haven, MA 02568

F. R. Eldridge, Jr.
The Mitre Corporation
1820 Dolley Madison Blvd.
McLean, VA 22102

Electric Power Research Institute
3412 Hillview Avenue
Palo Alto, CA 94304
Attn: E. Demeo
F. Goodman
S. Kohan

R. G. Ferreira
The Resources Agency
Department of Water Resources
Energy Division
1416 9th Street
P.O. Box 388
Sacramento, CA 95802

D. R. Finley
New England Geosystems
P.O. Box 128
East Derry, NH 03041

FloWind Corporation
21414 68th Avenue South
Kent, WA 98031
Attn: S. Tremoulet
I. E. Vas

J. D. Fock, Jr.
Department of Aerospace Engineering Sciences
University of Colorado
Boulder, CO 80309

G. A. Fontana (2)
Burns & Roe, Inc.
800 Kinderkamack Road
Oradell, NJ 07649

Dr. L. C. Frederick
Public Service Company of New Hampshire
1000 Elm Street
Manchester, NH 03105

H. Gerardin
Mechanical Engineering Department
Faculty of Sciences and Engineering
Universite Laval-Quebec
CANADA G1K 7P4

E. Gilmore
Amarillo College
Amarillo, TX 79100

R. T. Griffiths
University College of Swansea
Department of Mechanical Engineering
Singleton Park
Swansea SA2 8PP
UNITED KINGDOM

Professor G. Gregorek
Ohio State University
Aeronautical and Astronautical Department
2070 Neil Avenue
Columbus, OH 43210

A. A. Hagman
Kaiser Aluminum and Chemical Sales, Inc.
14200 Cottage Grove Avenue
Dolton, IL 60419

Professor N. D. Ham
Massachusetts Institute of Technology
77 Massachusetts Avenue
Cambridge, MA 02139

Capt. J. L. Hanson
United States Air Force
Energy Technology Liaison Office
NGD
DOE/ALO
Albuquerque, NM 87115

C. F. Harris
Wind Engineering Corporation
Airport Industrial Area
Box 5936
Lubbock, TX 79415

W. L. Harris
Aero/Astro Department
Massachusetts Institute of Technology
Cambridge, MA 02139

Terry Healy (2)
Rockwell International
Rocky Flats Plant
P.O. Box 464
Golden, CO 80401

Helion, Inc.
Box 445
Brownsville, CA 95919

T. Hillesland
Pacific Gas & Electric
3400 Crow Canyon Road
San Ramon, CA 94583

JBF Scientifcic Corporation
2 Jewel Drive
Wilmington, MA 01887
Attn: E. E. Johanson

Dr. G. L. Johnson
Electrical Engineering Department
Kansas State University
Manhattan, KS 66506

Kaman Aerospace Corporation
Old Windsor Road
Bloomfield, CT 06002
Attn: W. Batesol

R. E. Kelland
The College of Trades and Technology
P.O. Box 1693
Prince Philip Drive
St. John's, Newfoundland
CANADA A1C 5P7

R. H. Klein
KW Control Systems, Inc.
RD#4, Box 914C
South Plank Road
Middletown, NY 10940

O. Krauss
Michigan State University
Division of Engineering Research
East Lansing, MI 48825

M. Lechner
Public Service Company of New Mexico
P.O. Box 2267
Albuquerque, NM 87103

Kalman Nagy Lehoczky
Cort Adelers GT. 30
Oslo 2
NORWAY

G. E. Lennox
Mill Products Division
Reynolds Metals Company
6601 West Broad Street
Richmond, VA 23261

J. Lerner
State Energy Commission
Research and Development Division
1111 Howe Avenue
Sacramento, CA 95825

L. Liljidahl
Building 005, Room 304
Barc-West
Beltsville, MD 20705

P. B. S. Lissaman
Aeroenvironment, Inc.
660 South Arroyo Parkway
Pasadena, CA 91105

Olle Ljungstrom
FFA, The Aeronautical Research Institute
Box 11021
S-16111 Bromma
SWEDEN

Beatrice de Saint Louvent
Establissement d'Etudes et de Recherches
Meteorologigues
77, Rue de Serves
92106 Boulogne-Billancourt Cedex
FRANCE

Ernel L. Luther
PRC Energy Analysis Co.
7600 Old Springhouse Road
McLean, VA 22101

E. L. Markowski
Motorola, Inc.
G.E.D.
Mail Drop 1429
8201 E. McDowell Road
P.O. Box 1417
Scottsdale, AZ 85252

Frank Matanzo
Dardalen Associates
15110 Frederick Road
Woodbine, MD 21797

H. S. Matsuda
Composite Materials Laboratory
Pioneering R&D Laboratories
Toray Industries, Inc.
Sonoyama, Otsu, Shiga
JAPAN 520

J. R. McConnell
Tumac Industries, Inc.
650 Ford Street
Colorado Springs, CO 80915

R. N. Meroney
Colorado State University
Department of Civil Engineering
Fort Collins, CO 80521

G. N. Monsson
Department of Economic Planning
and Development
Barrett Building
Cheyenne, WY 82002

Napier College of Commerce and Technology
Tutor Librarian, Technology Faculty
Colinton Road
Edinburgh, EH10 5DT
ENGLAND

NASA Lewis Research Center (4)
21000 Brookpark Road
Cleveland, OH 44135
Attn: D. Baldwin
J. Savino

A. A. Nedd
The Power Company, Inc.
P.O. Box 221
Genesee Depot, WI 53217

V. Nelson
West Texas State University
Department of Physics
P.O. Box 248
Canyon, TX 79016

Leander Nichols
Natural Power, Inc.
New Boston, NH 03070

Roger O'Hara
Energy Times
909 NE 43rd
Suite 308
Seattle, WA 98105

Oklahoma State University
Stillwater, OK 76074
Attn: D. K. McLaughlin
ME Department

Oregon State University (2)
Corvallis, OR 97331
Attn: R. W. Thresher
ME Department
R. E. Wilson
ME Department

Alcir de Faro Orlando
Pontificia Universidade Catolica-PUC/Rj
Mechanical Engineering Department
R. Marques de S. Vicente 225
Rio de Janeiro, BRAZIL

Ion Paraschivoiu
IREQ
1800 montee Ste-Julie
Varennes, Quebec
CANADA JOL 2PO

G. D. Park
Gates Learjet
Mid-Continent Airport
P.O. Box 7707
Wichita, KS 67277

R. A. Parmalee
Northwestern University
Department of Civil Engineering
Evanston, IL 60201

Troels Friis Pedersen
Riso National Laboratory
Postbox 49
DK-4000 Roskilde
DENMARK

Helge Petersen
Riso National Laboratory
DK-4000 Roskilde
DENMARK

Wilson Prichett, III
National Rural Electric Cooperative Association
1800 Massachusetts Avenue NW
Washington, DC 20036

K. R. Rasmussen
Utah Power and Light Co.
51 East Main Street
P.O. Box 277
American Fork, UT 84003

T. W. Reddoch
Department of Electrical Engineering
The University of Tennessee
Knoxville, TN 37916

R. G. Richards
Atlantic Wind Test Site
P.O. Box 189
Tignish P.E.I.
CANADA COB 2BO

A. Robb
Memorial University of Newfoundland
Faculty of Engineering and Applied Sciences
St. John's Newfoundland
CANADA A1C 5S7

J. R. Rodriquez
Solarwind Energy Corporation
1163 Pomona Road
Unit A
Corona, CA 91720

Dr. -Ing. Hans Ruscheweyh
Institut fur Leichbau
Technische Hochschule Aachen
Wullnerstrasse 7
GERMANY

R. K. St. Aubin
Aerolite, Inc.
550 Russells Mills Road
South Dartmouth, MA 02748

R. L. Scheffler
Southern California Edison
R&D Department
Room 497
P.O. Box 800
Rosemead, CA 91770

Gwen Schreiner
Librarian
National Atomic Museum
Albuquerque, NM 87185

Arnan Seginer
Professor of Aerodynamics
Technion-Israel Institute of Technology
Department of Aeronautical Engineering
Haifa, ISRAEL

Dr. Horst Selzer
Dipl.-Phys.
Wehrtechnik und Energieforschung
ERNO-Raumfahrttechnik GmbH
Hunefeldstr. 1-5
Postfach 10 59 09
2800 Bremen 1
GERMANY

H. Sevier
Rocket and Space Division
Bristol Aerospace Ltd.
P.O. Box 874
Winnipeg, Manitoba
CANADA R3C 2S4

P. N. Shankar
Aerodynamics Division
National Aeronautical Laboratory
Bangalore 560017
INDIA

David Sharpe
Kingston Polytecnic
Canbury Park Road
Kingston, Surrey
UNITED KINGDOM

Kent Smith
Instituto Technologico Costa Rico
Apartado 159 Cartago
COSTA RICA

L. H. Soderholm
Iowa State University
Agricultural Engineering, Room 213
Ames, IA 50010

G. Stacey
The University of Reading
Department of Engineering
Whiteknights, Reading, RG6 2AY
ENGLAND

Bent Sorenson
Roskilde University Center
Energy Group, Bldg. 17.2
IMFUFA
P.O. Box 260
DK-400 Roskilde
DENMARK

D. T. Stjernholm
Morey/Stjernholm and Associates
1050 Magnolia Street
Colorado Springs, CO 80907

G. W. Stricker
130 Merchant St. #1104
Honolulu, HI 96813

C. J. Swet
Route 4
Box 358
Mt. Airy, MD 21771

John Taylor
National Research Council
ASEB
2101 Constitution Avenue
Washington, DC 20418

R. J. Templin (3)
Low Speed Aerodynamics Section
NRC-National Aeronautical Establishment
Ottawa 7, Ontario
CANADA K1A OR6

Texas Tech University (3)
P.O. Box 4389
Lubbock, TX 79409
Attn: J. W. Oler
ME Department
J. Strickland
ME Department

J. M. Turner
Terrestrial Energy Technology Program Office
Energy Conversion Branch
Aerospace Power Division
Aero Propulsion Laboratory
Department of the Air Force
Air Force Wright Aeronautical Laboratories (AFSC)
Wright-Patterson Air Force Base, OH 45433

United Engineers and Constructors, Inc.
Advanced Engineering Department
30 South 17th Street
Philadelphia, PA 19101
Attn: A. J. Karalis

University of New Mexico
New Mexico Engineering Research Institute
Campus P.O. Box 25
Albuquerque, NM 87131
Attn: G. G. Leigh

Jan Vacek
Eolienne experimentale
C.P. 279, Cap-aux-Meules
Iles de la Madeleine, Quebec
CANADA

P. N. Vosburgh
Forecast Industries, Inc.
3500A Indian School Road NE
Albuquerque, NM 87106

Otto de Vries
National Aerospace Laboratory
Anthony Fokkerweg 2
Amsterdam 1017
THE NETHERLANDS

R. Walters
West Virginia University
Department of Aero Engineering
1062 Kountz Avenue
Morgantown, WV 26505

G. R. Watson
The Energy Center
Pennine House
4 Osborne Terrace
Newcastle upon Tyne NE2 1NE
UNITED KINGDOM

Tom Watson
Canadian Standards Association
178 Rexdale Blvd.
Rexdale, Ontario
CANADA M9W 1R3

R. G. Watts
Tulane University
Department of Mechanical Engineering
New Orleans, LA 70018

Gary Wayne
Department of Mechanical and Aerospace Engineering
Upson Hall
Cornell University
Ithaca, NY 14853

Larry Wendell
Battelle-Pacific Northwest Laboratory
P.O. Box 999
Richland, WA 99352

T. Wentink, Jr.
University of Alaska
Geophysical Institute
Fairbanks, AK 99701

D. Westlind
Central Lincoln People's Utility District
2129 North Coast Highway
Newport, OR 97365-1795

West Texas State University
Government Depository Library
Number 613
Canyon, TX 79015

Wind Energy Report
Box 14
102 S. Village Avenue
Rockville Centre, NY 11571
Attn: Farrell Smith Seiler

Wind Power Digest
P. O. Box 700
Bascom, OH 44809
Attn: Michael Evans

Wind Program Manager
Wisconsin Division of State Energy
8th Floor
101 South Webster Street
Madison, WI 53702

R. E. Wong
Central Solar Energy Research Corporation
1200 Sixth Street
328 Executive Plaza
Detroit, MI 48226

Jerry Yudelson
Solar Initiative
162 Christen Drive
Pacheco, CA 94553

1520 T. B. Lane
1523 R. C. Reuter, Jr.
1523 D. B. Clauss
1523 D. W. Lobitz
1523 P. S. Veers
1524 W. N. Sullivan
1600 D. B. Shuster
1630 R. C. Maydew
1633 R. E. Sheldahl
1636 J. K. Cole
1636 D. E. Berg
2525 R. P. Clark
3141 L. J. Erickson (5)
3151 W. L. Garner (3)
3154-3 C. H. Dalin (25)
For DOE/TIC (Unlimited Release)
3160 J. E. Mitchell (15)
3161 P. S. Wilson
7111 J. W. Reed
8214 M. A. Pound
9000 G. A. Fowler
6200 E. H. Beckner
6220 D. G. Schueler
6225 R. H. Braasch (50)
6225 R. E. Akins
6225 J. D. Cyrus
6225 R. D. Grover
6225 E. G. Kadlec
6225 P. C. Klimas
6225 M. T. Mattison
6225 R. O. Nellums
6225 M. H. Worstell